

University of New Hampshire

University of New Hampshire Scholars' Repository

Doctoral Dissertations

Student Scholarship

Spring 2022

Water droplet machining and droplet impact mechanics

Benjamin Mitchell

University of New Hampshire, Durham

Follow this and additional works at: <https://scholars.unh.edu/dissertation>

Recommended Citation

Mitchell, Benjamin, "Water droplet machining and droplet impact mechanics" (2022). *Doctoral Dissertations*. 2685.

<https://scholars.unh.edu/dissertation/2685>

This Dissertation is brought to you for free and open access by the Student Scholarship at University of New Hampshire Scholars' Repository. It has been accepted for inclusion in Doctoral Dissertations by an authorized administrator of University of New Hampshire Scholars' Repository. For more information, please contact Scholarly.Communication@unh.edu.

Water Droplet Machining and Droplet Impact Mechanics

By

Benjamin R Mitchell

BS, Mechanical Engineering, University of New Hampshire, 2015

DISSERTATION

Submitted to the University of New Hampshire
in Partial Fulfillment of
the Requirements for the Degree of

Doctor of Philosophy
in
Mechanical Engineering

May, 2022

This dissertation was examined and approved in partial fulfillment of the requirements for the degree of Doctor of Philosophy in Mechanical Engineering by

Dissertation Director, Brad L Kinsey,
Professor of Mechanical Engineering,
University of New Hampshire

Co-Director, Yannis P Korkolis,
Associate Professor of Integrated Systems Engineering,
The Ohio State University

Joseph C Klewicki,
Head of School, Elec, Mech & Infrastructure Engineering,
University of Melbourne

Jinjin Ha,
Assistant Professor of Mechanical Engineering,
University of New Hampshire

Greg P Chini,
Professor of Mechanical Engineering,
University of New Hampshire

On April 13, 2022

Approval signatures are on file with the University of New Hampshire Graduate School.

ACKNOWLEDGMENTS

Funding from the U.S. National Science Foundation through award No. CMMI-1462993 is gratefully acknowledged. Support from the University of New Hampshire Graduate School, John Olson Advancement Manufacturing Center (JOAMC), as well as faculty and staff from the College of Engineering and Physical Sciences (CEPS) is greatly appreciated.

TABLE OF CONTENTS

ACKNOWLEDGMENTS	iii
LIST OF TABLES	vii
LIST OF FIGURES	viii-ix
ABSTRACT	x

CHAPTERS

INTRODUCTION	1
1. DROPLET IMPACT FORCE	5
1.1 Description of experiments.....	11
1.2 Results.....	15
1.2.1 Stages of impact.....	16
1.2.2 Force profiles	17
1.2.3 Peak force	19
1.2.4 Normalized Profiles.....	20
1.2.5 Impulse and change in momentum	24
1.2.6 Free-surface configuration at peak force.....	25
1.2.7 Long-time behavior of inertial profiles	26
1.3 Force model.....	29
1.4 Long-time force decay measured from free-surface height evolution.....	32
1.5 Summary.....	39
2. IMPACT FORCE OF RAYLEIGH JETS	41
2.1 Classification of jet regimes	44
2.2 Droplet formation from Rayleigh jets	46
2.2.1 Plateau's reasoning	46
2.2.2 Rayleigh's local analysis	47
2.2.3 Spatial analysis.....	49
2.2.4 Stimulated droplet formation.....	51
2.2.5 Effects of nozzle geometry	51

2.2.6 Other analyses.....	52
2.3 Force induced by continuous jets	53
2.3.1 Steady state jets.....	53
2.3.2 Wavy jets	54
2.4 Force induced by droplets.....	57
2.5 Experimental setup and procedures.....	62
2.6 Results and discussion.....	65
2.6.1 Steady state jet.....	67
2.6.2 Wavy jet.....	67
2.6.3 Droplet train.....	70
2.6.4 Impulse and momentum conservation.....	75
2.6.5 Steady-state jet versus droplet train.....	76
2.7 Summary.....	77
3. ANALYSIS OF HERTZIAN CONTACT USING PHOTOELASTICITY	79
3.1 Experimental methodologies	82
3.1.1 Material properties	84
3.1.2 Experimental setup	85
3.2 Integrated photoelasticity	87
3.2.1 Integral Wertheim law.....	88
3.2.2 Stokes parameters and the optically equivalent model.....	89
3.3 Hertzian contact theory.....	95
3.3.1 Derivation.....	95
3.3.2 Secondary principal stress.....	101
3.3.3 Boundary effects.....	103
3.4 Numerical simulation.....	104
3.5 Results and discussion.....	106
3.5.1 Phase retardation fields.....	106
3.5.2 Maximum equivalent stress and principal stress components.....	114
3.5.3 Maximum surface displacement and contact radius.....	122
3.6 Summary.....	124
4. WATER DROPLET MACHINING PROCESS AND EROSION CHARACTERISTICS	126
4.1 State of the art.....	128

4.2. Experimental setup and methodologies.....	131
4.3. Start up and steady-state operating conditions	137
4.4 Influence of stand-off distance.....	141
4.5 Influence of jet diameter	148
4.6 Comparison with conventional pure waterjet cutting	152
5. CUTTING CARBON FIBER WITH AWJ VS. WDM.....	154
5.1 Experimental methods	156
5.2 Results and discussion.....	158
5.2.1 Abrasive waterjet cutting of CFRP.....	158
5.2.2 Water droplet machining of CFRP	159
5.2.3 Surface roughness of WDM cut edges on CFRP	162
5.2.4 Dimensional accuracy of AWJ and WDM cuts	163
5.3 Summary.....	166
6. CONCLUSIONS AND FUTURE WORK	168
LIST OF REFERENCES.....	172

LIST OF TABLES

1. Material properties of the liquids employed in droplet impact force study.....	13
2. Test conditions of single droplet impact study.....	18
3. Material properties and experimental parameters used in photoelasticity	85
4. Dimensional results of hole cutting	166

LIST OF FIGURES

1.1 Droplet impact force experimental apparatus.....	12
1.2 Stages of droplet impact	16
1.3 Force-time profiles.....	19
1.4 Non-dimensional force profiles	21
1.5 Deformed droplet configuration at peak force	26
1.6 Long-time behavior of the inertial droplet force profile.....	27
1.7 Droplet free-surface height evolution.....	35
1.8 Central height evolution	38
2.1 Schematic of the normal impingement of Rayleigh jets	42
2.2 Rayleigh dispersion relation.....	49
2.3 Theoretical force of droplet train vs. steady jet.....	61
2.4 Schematic of Rayleigh jet experimental setup	64
2.5 High-speed images of Rayleigh jet impact.....	66
2.6 Force induced by Rayleigh jets.....	66
2.7 Wavy jet free-surface profile	69
2.8 Force induced by droplet train	72
2.9 Experimental force of droplet train vs. steady jet	77
3.1 Schematic of Hertzian contact problem	83
3.2 Image of photoelasticity experimental setup	86
3.3 Numerical simulation results of Hertzian contact	105
3.4 Photoelastic phase field for 1 gram mass.....	107
3.5 Photoelastic phase field for 5 gram mass.....	108
3.6 Photoelastic phase field for 10 gram mass	109
3.7 Photoelastic phase field for 16 gram mass	110
3.8 Maximum phase for various load cases	113
3.9 Von Mises stress at mid-plane.....	115
3.10 Secondary principal stress profile.....	116
3.11 Relation between von Mises stress and phase	119
3.12 Principal stresses for various load cases	121
3.13 Surface displacement of sphere	122
3.14 Contact radius of sphere.....	124
4.1 Schematic of idealized water droplet machining process	130
4.2 Water droplet machining experimental setup	133
4.3 Trench features in workpiece.....	136
4.4 Pressure and temperature response at cool-down	140
4.5 Image of tests conducted at various stand-off distances	143
4.6 Trench profiles of various stand-off distances and feed rates	144
4.7 Maximum trench depth for various feed rates	145
4.8 Material removal rate for stand-off distance tests	146
4.9 Image of tests conducted with different orifice diameters.....	149
4.10 Trench profiles for different orifice diameters	150
4.11 Material removal rate for different orifice diameters.....	151
4.12 Comparison of pure waterjet and water droplet machined workpiece.....	153

5.1 Image of abrasive waterjet cut carbon fiber workpiece	159
5.2 Image of water droplet machined carbon fiber workpiece	160
5.3 Microscope image of carbon fiber cut edge	163
5.4 Dimensional accuracy measurement results.....	164
6.1 Steel pocket created with water droplet machining.....	170
6.2 Range of materials cut with water droplet machining	171
6.3 Various components made with water droplet machining	172

Abstract

Water Droplet Machining (WDM) is a new manufacturing process, which uses a series of high-velocity, pure-water droplets to impact and erode metal workpieces, for the purpose of through-cutting, milling and surface profiling. The process is conducted within a vacuum environment to suppress aerodynamic drag and atomization of the waterjet and droplet stream. This preserves droplet momentum and allows for a more efficient transfer of energy between the water and workpiece, than in standard atmospheric pressure. As a new manufacturing technique, parameter-specific details and characteristics of this process are absent from the scientific literature. Furthermore, the erosion mechanisms involved in droplet-solid interactions are not well-understood. Therefore, this research aims to elucidate the capabilities of WDM, and uncover the mechanics involved in droplet impact. This is done by investigating the force imparted by liquid droplets across a wide range of impact parameters, where a novel force model is developed for inertial-dominated impacts. A force comparison is made between continuous jet and droplet train impacts, where the findings show that a droplet train has a higher erosive potential than its continuous jet counterpart, owing to the higher forces exerted by individual droplets. In addition, the stress state inside of a material subject to a Hertzian contact, which is connected to this research as it emulates the axisymmetric nature of a droplet-like loading, is explored using integrated photoelasticity. Finally, the process parameters and erosion characteristics of WDM are investigated using a custom-fabricated machine, where a range of waterjet-types (and droplet trains) are produced. The industrial efficacy of this process is evaluated by manufacturing a diverse array of engineering materials.

INTRODUCTION

Abrasive waterjet (AWJ) cutting is a common machining process used in the manufacturing industry. Favorable for its ability to cut temperature-sensitive materials and for its fast feed rates, AWJ is utilized in industries such as aerospace, automotive, medical, and electronics [1], and can cut nearly any material, including diamond [2]. The process involves a multi-phase slurry of high-speed water mixed with abrasive particles and entrained air, which collides with a workpiece inducing local deformation and failure. Ploughing of abrasive particles dominates the erosion process [3], making abrasives essential for satisfactory operation. Composed of crushed garnet gemstone, the abrasives are typically disposed of after a single use due to the loss of their sharp edges and difficulty of retrieving. Mining, transportation, and storing of abrasives contribute to the high operating cost of AWJ, which is unfavorable for the manufacturing industry and the environment. Furthermore, workpiece and workplace cleanliness are important aspects in specialized applications, such as medical implants and aerospace components, where abrasive particle-embedment is unacceptable. This motivates the search for abrasive-less, environmentally friendly, and cost-effective machining alternatives to AWJ.

A recent development in waterjet technology has been proposed [4], which eliminates the use of abrasives, and instead utilizes high-speed, pure-water droplet impacts to erode and cut-through materials. In this technique, referred to herein as Water Droplet Machining (WDM), high pressure water is accelerated through an orifice forming a waterjet which, with downstream evolution, segments into a train of droplets via capillary instabilities, i.e., Rayleigh-type breakup [5]. The resulting droplet train then impinges and

locally erodes the workpiece for the purpose of cutting, milling, or surface profiling. The process is conducted within a vacuum environment to suppress aerodynamic drag and atomization of the waterjet and droplet train. Unlike continuous waterjets, e.g., AWJ, the discrete nature of a droplet train prevents the buildup of a liquid layer on the workpiece surface, which produces efficient momentum transfer.

The erosion associated with the impact of a droplet onto a solid surface has been considered by several authors [6-9] and has been the subject of investigations in steam and wind turbine damage [10-11], as well as aircraft damage when flying through rain [12]. Most studies characterize the erosion based on empirical models, while others credit the shockwave, water hammer pressure for material removal [13-14]. A model which describes the erosion induced by a high-speed droplet train is absent. However, such a model would be useful for predictive analyses in WDM and would help identify the physical mechanisms involved in the droplet-impact-erosion phenomena.

The only past published work considering WDM is the patent [4], which provides information on how to create a high-speed droplet train. However, details are lacking regarding WDM process parameters, process capabilities, and its feasibility as an industrial machining operation. Furthermore, evidence of the process's effectiveness is absent and has led to speculation among many for its ability to process high-strength materials, such as steel. This Ph.D. research aims to fill in these knowledge gaps so that industry may consider and take advantage of this novel material processing technique and to help uncover the physical mechanisms of the droplet-impact-erosion phenomenon. This research is categorized into two main components: droplet-solid interaction and the

WDM manufacturing process. The WDM process research includes the capabilities of WDM, the parameters necessary for effective material removal, and its operation as a manufacturing device, while the droplet impact research focuses on the mechanics involved with the collapse of droplets onto solid materials. This is done, in part, by investigating the forces, stresses and strains imparted by droplets and droplet trains.

This dissertation is outlined as follows. Chapter 1 investigates the force of single, isolated droplet impacts across a range of impact parameters, i.e., velocities and liquids (with varying densities, viscosities and surface tensions). An inertial-dominated regime is found, where force profiles adhere to a normalized, self-similar master curve [15]. The significance of this study is the development of a novel force model, which accurately predicts the entire time-dependent loading of droplet impacts over a wide range of Reynolds and Weber numbers [15]. Chapter 2 describes the droplet formation mechanisms from a continuous jet and studies the impact force exerted by droplet trains and continuous jets. The force model explained in Chapter 1 was further developed, in a time-series fashion, to accommodate droplet-train impacts [16]. The importance of this study identifies that the peak force exerted by a droplet train is approximately four times greater than the force exerted by a continuous jet of equal momentum. This finding suggests that droplet trains exhibit a higher erosive potential than their continuous jet counterparts. Chapter 3 investigates the stress state of materials subject to a Hertzian contact, which emulates the axisymmetric loading condition found in a droplet impact, through integrated photoelasticity, which is typically only employed for 2D situations. The significance here is that the stress tensor and components at the point where maximum equivalent stress occurs are fully determined through photoelastic experimentation. This

provides crucial insight into yield forecasting and provides the framework to identify the stresses a material will experience when subject to droplet loading. Chapter 4 formally introduces the WDM technology and its principals of operation. A custom-built machine is used to explore the process parameters, where the type of jet configuration is controlled by varying the orifice diameter, velocity, and standoff distance from the nozzle to the workpiece for a desired erosion outcome. The erosion characteristics of WDM are studied on aluminum and steel and are compared to the erosion rates produced by traditional pure, and abrasive waterjet cutting. These studies are significant because they demonstrate how WDM is an advancement in pure waterjet cutting technology. This has broader impacts in the manufacturing community, as a range of aerospace, automotive, medical, and electronic components can be manufactured with this clean, environmentally friendly process, which uses water alone. Chapter 5 investigates the capabilities of WDM in through-cutting, milling, and surface profiling modes, and identifies a diverse range of materials that can be cut with WDM.

1. DROPLET IMPACT FORCE

(Text for this chapter is taken from [15], i.e., Mitchell, B. R., Klewicki, J. C., Korkolis, Y. P., & Kinsey, B. L. (2019). The transient force profile of low-speed droplet impact: measurements and model. *Journal of Fluid Mechanics*, 867, 300-322. My contributions to this work were all experimental and theoretical investigations.)

The impact of liquid droplets on a flat, solid surface is a subject of scientific interest due to the highly dynamic and complex nature of the impacting droplet structure. Research on such impacts support a range of disciplines within fluid mechanics as the physical parameters of Reynolds, Weber, capillary, Mach, and Marangoni numbers can vary rapidly and spatially throughout the impinging drop [17-21]. This diversity of physical phenomena renders the droplet impact problem a useful testing platform for a multitude of fields. Phenomena such as von Kármán vortices [22], shock waves [23], cavitation [24], waves [25], jets [26], contact line motion [27], bloodstain patterns [28] and, of course, spreading and splashing [29], can be studied through droplet impacts. For typical millimeter-sized rain droplets most of these phenomena happen on the order of milliseconds making observations difficult for the human eye. Advancements in novel measurement technologies and high-speed cameras has, however, allowed these areas to be studied in detail, and are now widely growing areas of interest [29]. The impact of a drop of water is a seemingly simple everyday occurrence but despite its growing attention, an accurate mathematical equation describing the entire force evolution does not yet exist. Technical applications must therefore rely on empirical data, simulations, or assumptions to approximate the entire time-dependent loading.

Relative to applications, droplet impacts can erode steam and wind turbine blades [30-31], scour aircraft [32], and serve as a materials processing technique via high-speed, droplet train impingement [4, 33]. In nature, droplet impacts can erode soil [34], compact snow [35], disrupt hummingbird and mosquito flight [36-37], and even damage the surfaces of leaves [38]. In each case, the force–time history associated with the droplet impact is of considerable importance, since it characterizes the time scale over which an object will experience the impact force and the resulting impulse (i.e., change in momentum). Similarly, in designing material processing applications, the force–time history is essential to characterize material erosion, since it provides an evolution of the time-dependent loading. This allows, for example, the calculation of stresses and strains experienced by the solid. Due to their rapid deformation and potentially destructive nature, high-speed droplet impacts are inherently difficult to image and pose significant measurement challenges. Therefore, in this study, we establish an appropriate scaling law that captures the dominant physics of low-speed droplet impacts, and, through this, provide a foundation for which the force–time profiles of high-speed impacts can be estimated. This is done by measuring droplet impact force–time profiles over a significant range of Reynolds and Weber numbers, then, using the data, along with existing theories, develop a model which accurately describes high Reynolds and Weber number impacts. Several experimental studies, e.g., [21, 39-43], have investigated various aspects of the normal impingement of a water droplet onto a flat, rigid surface. Such measurements reveal that the impact force is characterized by a rapid rise to a maximum, followed by a much more gradual decay to zero force. As might be intuitively surmised, existing studies indicate that the peak force increases with increased droplet diameter, d , liquid density,

ρ , and/or impact velocity, v . One study found the force to scale as the square of impact velocity [44]. Another study found the time duration (total time in which a droplet imparts a normal force) decreases with impact velocity and increases with increased droplet diameter [41]. A similar study showed the droplet impact force–time profile is Reynolds number invariant, above $Re = 230$, as only the inertial parameters (i.e., ρ , v , and d) affect the profile [42]. Here, the Reynolds and Weber numbers are respectively given by,

$$Re = \rho v d / \mu , \quad (1.1)$$

$$We = \rho d v^2 / \sigma , \quad (1.2)$$

where μ and σ are the liquid's viscosity and surface tension, respectively. Conversely, as the Reynolds number decreases, below $Re = 230$, viscosity plays a more dominant role. Specifically, the normalized peak force increases, while the normalized time duration decreases. In this impact regime, viscosity impedes droplet spreading, and as shown later in this chapter, promotes a faster deceleration of the drop, altering the inertial force profile.

In the extensive study of [21], the force profiles in a Reynolds number range of approximately $10^{-1} < Re < 10^4$, were measured, resulting in the discovery of visco-elastic, viscous and inertial regimes. In the visco-elastic regime ($Re < 0.7$), the force–time profile is nearly symmetric about the maximum force, corresponding to an elastic sphere impact. After this stage, a negative force is imparted, relating to a rebound effect. In the viscous regime, which occurs in the range of approximately $0.7 < Re < 200$, reference [21] found the early pre-peak force to scale as $1/\sqrt{Re}$. They provide a formal justification for this scaling law using the boundary layer thickness (found in [45]), with a perturbation expansion from the inviscid solution based on [19]. The approximate solution predicts a

$1/\sqrt{Re}$ scaling, good to order (Re^{-1}) and is supported by their experiments. In the inertial regime, [21] found self-similarity of all measured force profiles above $Re = 200$. Here, the peak force is found to equal approximately $0.85\rho v^2 d^2$. In addition, [21] experimentally verify the early time, \sqrt{t} force dependence, theoretically determined by [19]. The present experimental results, which were historically compiled over the same time frame, reinforce this finding. During the initial pre-peak rise in force, [19] has shown that the velocity and pressure fields adhere to a self-similar form and in addition, predict the normal impact force to grow in time like \sqrt{t} , namely:

$$F(t) = \sqrt{\frac{27}{2}} \rho d^{3/2} v^{5/2} \sqrt{t}, \quad (1.3)$$

This equation accurately predicts the impact force of inertial (i.e., high Re , high We), droplet impacts for early stages of impact, before peak force, as shown by [21]. In their study, they found the peak force to occur at a normalized time of about $\hat{t} = 0.18$, where $\hat{t} = tv/d$. Just before peak force, however, Eq. (1.3) diverges from the measurements and, thus, is only applicable for early time, i.e., $\hat{t} < 0.1$.

Other theoretical and numerical works on droplet impacts have been performed by [46-47], who collectively show that the center pressure of an impacting droplet obeys a $1/\sqrt{t}$ dependence, for early stages of deformation (up to approximately $\hat{t} = 0.5$). A subsequent rapid pressure decay commences thereafter. The $1/\sqrt{t}$ pressure dependence at the impact point agrees with the study of [19], while the long-time pressure decay observed in the simulations awaits further theoretical evaluation. Reference [48] also investigated the impact pressure. Here, the authors used the volume-of-fluid method to simulate the

normal impingement of inertia-dominated droplets onto a rigid surface. For times of the order of $\hat{t} = 1$, the results show the central pressure at the impact surface decays monotonically in time and is well approximated with an exponential of the form: e^{-t} . Although the droplet impact force is not explicitly calculated in reference [48], this form of pressure can be multiplied by the drop's contact area to obtain a force approximation. Such a calculation was done by using the contact area of a spherical cap [43]. The resulting force equation underestimates the measured force profiles. The equation does, however, follow the profile trends (i.e., sharp rise to maximum force followed by a gradual decay to zero). To provide a more suitable match, [43] has used an empirical equation based on an exponential-like decay. Although theoretical support is needed for the exponential decay, the use of it to describe the post-peak decay observed in experiments is quite appealing.

The force evolution at early times, first derived by [19] in Eq. (1.3), has been verified by [21], and is also supported by the present experiments. Since the early-time force evolution has credible establishment both theoretically and experimentally, a complementary aim of this work is to provide justification for the use of an exponential of the form: e^{-t} , to describe the post-peak decay. From this, a model equation is developed that accurately represents the entire force evolution of inertial droplet impacts, suitable for easy use in applications. This model includes the early time \sqrt{t} force dependence derived in [19], and the observed exponential post-peak decay. In addition, it is shown that the force decay can be predicted solely by the free-surface height evolution. In this alternative method, direct force measurements are not required. Instead, the free-surface

height evolution is used to calculate the impact force decay, and the ensuing results are shown to be in good agreement with direct force measurements.

The present experiments cover a range of Reynolds and Weber numbers of four and two decades, respectively. This is done by varying the liquid density, ρ , droplet diameter, d , impact velocity, v , fluid viscosity, μ , and surface tension, σ . Another important aspect of describing the physics involves controlling the shape of the droplet upon impact. A non-spherical droplet exerts a force–time profile that is different from a spherical droplet. This is due to variations in free-surface curvature, which result in variations in the duration of momentum transfer to the surface. For example, the present measurements show that, relative to a spherical droplet, oblate droplets correlate with shorter momentum transfer times, while prolate droplets correlate with longer momentum transfer times. This observation is reinforced by the recently reported findings of [43]. Such variations add undesirable complexity to the force–time profiles. Because of this, the present study restricts attention to droplets that are spherical to within a well-defined tolerance. This aim is accomplished by performing the experiments under sufficiently low ambient air pressure conditions, and thus avoiding the deviation from a spherical shape that occurs when significant drag is imparted by the surrounding gas [49]. For example, in standard atmospheric pressure (101 kPa), a 3.5 mm diameter water droplet falling at its terminal velocity, of approximately 8 m/s, has an aspect ratio, e (defined later), of approximately 0.8 [50-51].

In what follows, this chapter first describes the experimental procedures and the range of parameters explored. This is followed by a presentation of the experimental results from which the parameter thresholds are determined, and where self-similar, force–time

scaling exists. With this, a model equation is constructed for the entire force profile. The chapter concludes with a brief discussion of the primary experimental observations and the physics contained in the present model.

1.1 Description of experiments

The present experiments employ a custom-made apparatus that releases consistently sized droplets in a sub-atmospheric environment, see Figure 1.1. This apparatus features a 380 mm × 380 mm × 500 mm vacuum chamber, consisting of an aluminum frame enclosed by polycarbonate windows. An Edwards E2M30 vacuum pump is used to reduce the air pressure in the vacuum chamber, while an MKS 902 piezo transducer measures the ambient pressure inside the chamber with a resolution of 0.013 kPa (0.1 torr). For all tests, the absolute air pressure in the chamber is 12 + / – 0.4 kPa. The leak rate of the vacuum chamber at 12 kPa is approximately 0.006 kPa/s. During each trial, which takes a matter of seconds, the vacuum pump is turned off so that vibrations are reduced.

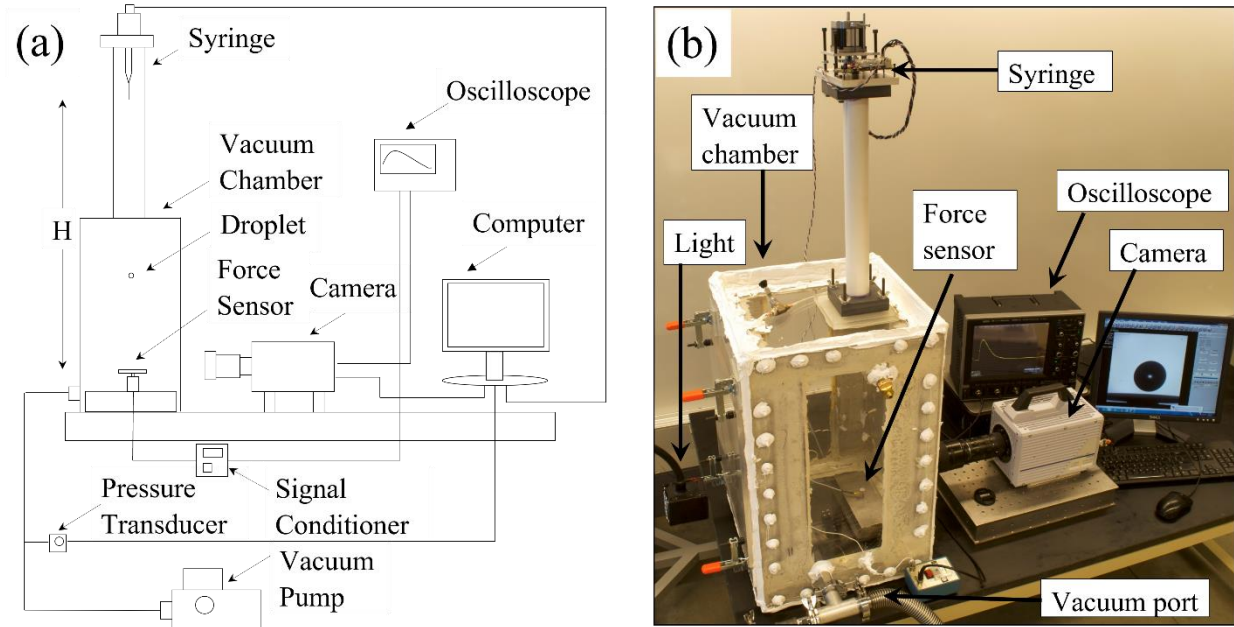


Figure 1.1: Droplet impact force experimental apparatus, (a) schematic, and (b) image.

A syringe with a double-gland, gas-tight piston expels droplets from a needle attached to its base, with the droplet subsequently falling onto the force sensor directly below. A stepper-motor controls the position of the piston, allowing precise dosimetry. Various lengths of polyvinyl chloride pipes, outfitted with o-rings and sealed to the vacuum chamber and syringe, allow for significant variations in the drop height, H (see Figure 1.1). Minor adjustments to H are accomplished by using variable thickness steel plates underneath the force sensor. The values of H in the present study resulted in impact velocities between 1.2 and 6.4 m/s, as detailed in the next section. Stainless steel needles attached to the syringe, generate droplet diameters between 1.7 and 5.1 mm. Three different liquids (ethanol, distilled water, and glycerin) are used to vary the viscosity, density, and surface tension of the impacting droplet, while in a temperature-controlled room of 20 °C. The ethanol used is 200 proof ethyl alcohol manufactured by PHARMCO-AAPER, and the glycerin is 99 % natural glycerin manufactured by PIT Process

Chemicals Inc. Furthermore, glycerin and distilled water are mixed at various proportions, to create liquids with properties between those of the pure substances. The material properties of the liquids used in the present experiments are listed in Table 1 [52-54].

Table 1: Material properties of the liquids employed.

Liquid	Density ρ (kg/m ³)	Viscosity μ (cP)	Surface tension σ (dyne/cm)
Glycerin	1258	1490	63
95 % Glycerin	1248	523	63
90 % Glycerin	1235	219	64
80 % Glycerin	1208	60	65
50 % Glycerin	1126	6	68
Water	998	1.0	73
Ethanol	789	1.1	23

A PCB model 209C11 piezo-electric force sensor with a calibrated sensitivity of 524.3 mV/N is located at the base of the vacuum chamber and is the target of the falling droplets. The impact surface is a polished 6061 aluminum cap with a surface roughness of $R_a = 0.09 \mu\text{m}$ (measured with a Mitutoyo SJ-400). A PCB 482 signal conditioner provides the excitation voltage to the sensor and a Lecroy Wavesurfer 64MXs-B oscilloscope sampling at 5 MHz is used to acquire the force–time measurements.

Droplet diameter prior to impact, impact velocity and post-impact deformation are determined from the analysis of high-speed camera images, obtained with a Photron Fastcam SA4 high-speed camera operating at 13,500 fps with an exposure time of 62 μs . All droplet impacts are recorded at this frame rate with the exception of images shown in Figure 1.2, which are recorded at 10,000 fps. A Northstar 250 W light is used to back illuminate the droplets, while a 105 mm Nikkor lens with a 49 mm extension tube is used to magnify the droplet images. The high-speed images reveal that, for the given range of

liquids and droplet sizes, the 12 kPa ambient air pressure sufficiently inhibits the air-drag-induced droplet distortion, while remaining well above the vapor pressure of the liquids used.

A position-tracking software was developed to determine the impact velocity and droplet diameter. The software utilizes a cross-correlation algorithm that determines the physical displacement of a droplet between two consecutive images. Dividing the physical displacement by the time between consecutive images provides an estimate for the droplet velocity. In all experiments the calculated velocity is within 5 % of the theoretical velocity (assuming no air drag), $v = \sqrt{2gH}$, where g is the acceleration due to gravity.

A distortion criterion is developed to ascertain if any given droplet deviates unacceptably from a spherical shape during its free fall. Distortion is quantified by the aspect ratio, e , i.e., the ratio between the length projected onto the axis of symmetry, d_1 , to the maximum diameter perpendicular to the axis of symmetry d_2 , $e = d_1/d_2$. In this study, only droplet impacts for which $0.95 < e < 1$ are considered. All droplets exhibited a slightly oblate ellipsoidal shape, $e < 1$, upon impact. This is consistent with the droplets being subject to the initial stages of air drag [55], albeit small, owing to the reduced pressure environment. The quantities d_1 and d_2 are determined from the ellipsoidal droplet images by an ellipse-fitting software. These quantities are also used to determine the equivalent droplet diameter, $d = (d_1 d_2^2)^{1/3}$, which is the diameter of a spherical droplet whose volume equals the volume of the ellipsoidal droplet. In order to validate the ellipse-fitting software, the equivalent droplet diameters, d , are compared to droplet diameters calculated from the measured droplet mass $d_m = (6m/\pi\rho)^{1/3}$, where ρ is the density and m is the droplet

mass. For test conditions 2, 9 and 11, the mass of 10 consecutive droplets are measured with a Mettler-Toledo MX5 scale having 1 μg precision. The droplets from these test conditions have large, small, and medium diameters, respectively. The average mass of each trial set is determined, and used as m to determine d_m . This is then compared to the equivalent droplet diameter d , in which case the equivalent droplet diameters are within 3 % of their d_m counterparts.

For all of the present experiments, low-amplitude, high-frequency oscillations are found to be superimposed onto the measured force profile. These oscillations stem from the vibration of the measurement system caused by the droplet impact. The oscillations are spectrally removed from the dataset using a method similar to that employed by [41]. The oscillation amplitude decreases with increased time and is, therefore, greatest at the beginning. For each test condition (listed in Table 2), five trials are performed, to verify repeatability. After droplet impact, the chamber is returned to atmospheric pressure, the door opened, and the impact plate wiped clean, in preparation for the next trial.

1.2 Results

In this section the stages of droplet deformation are introduced first, followed by force profile measurement results. Then, it is shown that the peak force occurs when the droplet side walls are perpendicular to the impact plate – a consequence of maximum momentum redirection. The normalized profiles are subsequently presented and compared with previous findings. This section also shows two distinct impact regimes (i) a self-similar inertial, and (ii) a viscous regime. Next, the impulse and change in momentum due to droplet impact is discussed, as well as how viscosity affects the free-surface configuration

at peak force. Finally, the long-time behavior of inertial profiles are investigated and are shown to be well approximated by an exponential decay law.

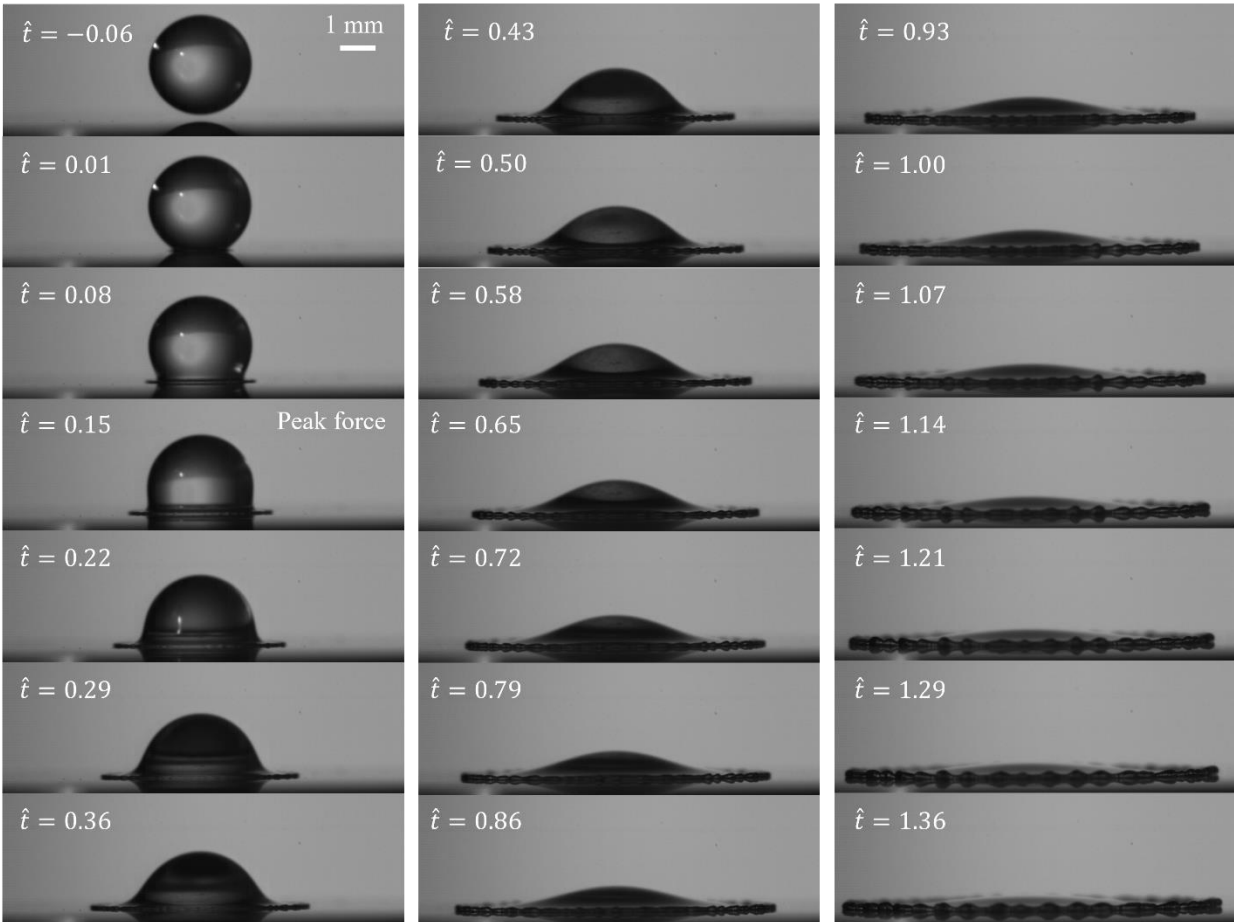


Figure 1.2: Stages of droplet impact. High-speed images of a 2.9 mm diameter water droplet impacting at 2.1 m/s, ($Re = 5960$, $We = 170$). The time between images is $100 \mu s$ (normalized time of $\hat{t} = tv/d = 0.07$). The progression of images start from the top left side, proceed downwards, then to the right.

1.2.1 Stages of impact

Figure 1.2 shows the stages of droplet deformation for a 2.9 mm diameter water droplet impacting at 2.1 m/s. The time between successive images is $100 \mu s$ (normalized time of $\hat{t} = 0.07$). The images are taken at 10,000 fps with an exposure time of $25 \mu s$. During the early stages of deformation, the droplet resembles a truncated sphere with a thin liquid jet circumscribing the initial point of contact. The thin liquid jet, or lamella, advances

parallel to the surface and radially away from the impact center. As the droplet deforms, liquid from the bulk travels to the spreading lamella and momentum is redirected from the normal to surface-parallel direction. This redirection of momentum induces the applied force at the surface. Specifically, the normal force acting on the plate is equal to the rate at which the total momentum within the collapsing droplet, normal to the plate, changes with time. The later stages of deformation exhibit a rippling effect in the lamella due to capillary instabilities about the advancing contact line [56]. The liquid ceases further radial advancement, as surface tension forces retract the lamella and contact line back toward the initial point of contact (not shown). The liquid then oscillates several times, although no clear normal force variations are observed during this stage.

1.2.2 Force profiles

Ensembles of the force profiles were generated as previously described, covering the 14 separate test conditions listed in Table 2. These experiments span Reynolds and Weber number ranges of $10 \leq Re \leq 29,800$ and $37 \leq We \leq 6360$, respectively. The force profiles for test condition 11 are shown in Figure 1.3. These results exemplify the typical force profile of a spherical droplet impinging normal to a flat rigid surface. As expected, the force increases rapidly, rising to a maximum of about 55 mN at approximately 160 μ s after initial impact, and then gradually returns to zero. The time duration is approximately 2 ms. Note that Figure 1.3(a) plots 5 trials, and thus provides an indication of experiment-to-experiment repeatability. The reduced ambient pressure helps facilitate impact location repeatability. In contrast, as the impact velocity increases, droplets travelling within standard atmospheric pressure rarely hit the same spot owing to the unsteady wakes that form behind them [57]. Additionally, Figure 1.3(a) compares the experiments with the

analytically derived, pre-peak rise in normal force given by [19]. As shown, the initial rise in force compares well with Eq. (1.3), but quickly diverges after 50 μ s. Note that droplet splashing is suppressed in the reduced pressure environment – a result found previously [58]. It has been shown that a splashing droplet impact exerts approximately the same force as a non-splashing droplet impact [59].

Table 2: Test conditions of single droplet impact.

	Test condition	Liquid	Velocity v (m/s)	Diameter d (mm)	Re	We
Viscous regime	1	Glycerin	2.9	4.0	10	690
	2	Glycerin	3.9	4.9	16	1500
	3	95 % Glycerin	2.8	4.0	27	610
	4	Glycerin	6.4	5.1	28	4200
	5	90 % Glycerin	2.8	4.0	64	610
	6	80 % Glycerin	3.9	3.6	280	1020
Self-similar, inertial regime	7	Ethanol	1.2	1.7	1460	86
	8	50 % Glycerin	2.8	3.7	1960	480
	9	Water	1.2	1.9	2270	37
	10	Ethanol	2.7	2.1	4070	530
	11	Water	2.7	2.9	7920	300
	12	Ethanol	6.3	3.3	15000	4540
	13	Ethanol	6.4	4.5	20700	6360
	14	Water	6.3	4.7	29800	2570

Together, the force measurements and high-speed images illustrate the interplay between the deformed droplet shape and its corresponding force. During the initial deformation, but before peak force, the droplet closely resembles a truncated sphere, surrounded by its radial lamella. During this stage there is a rapid increase in normal force due to the sudden redirection of flow that drives the expanding lamella. The liquid in the spreading lamella does not contribute to a significant normal force, but instead, induces a drag force due to the viscous boundary layer at the solid/liquid interface [45]. During the initial pre-peak rise, the upper portion of the droplet does not yet experience the effects of the impact surface and continues to travel towards the surface with its initial impact

velocity, v . Within the small region about the impact plane, however, the liquid rapidly decelerates and adheres to upward expanding self-similar pressure and velocity fields [19]. At this time, the impact-induced flow drives a tank-treading-like motion of the contact line, where the maximum pressure exists. This is a rather counterintuitive result as the maximum pressure does not occur at the central stagnation point, but rather near the expanding contact line [19]. By the time of peak force, the droplet closely resembles a dome with sides walls that are perpendicular with respect to the impact plane, see Figure 1.2. Peak force occurs at a normalized time of approximately $\hat{t} = 0.15$. In terms of the entire duration of normal force ($\hat{t} \cong 2.0$), the peak force is rapidly attained, within the first 10 % of normalized time duration.

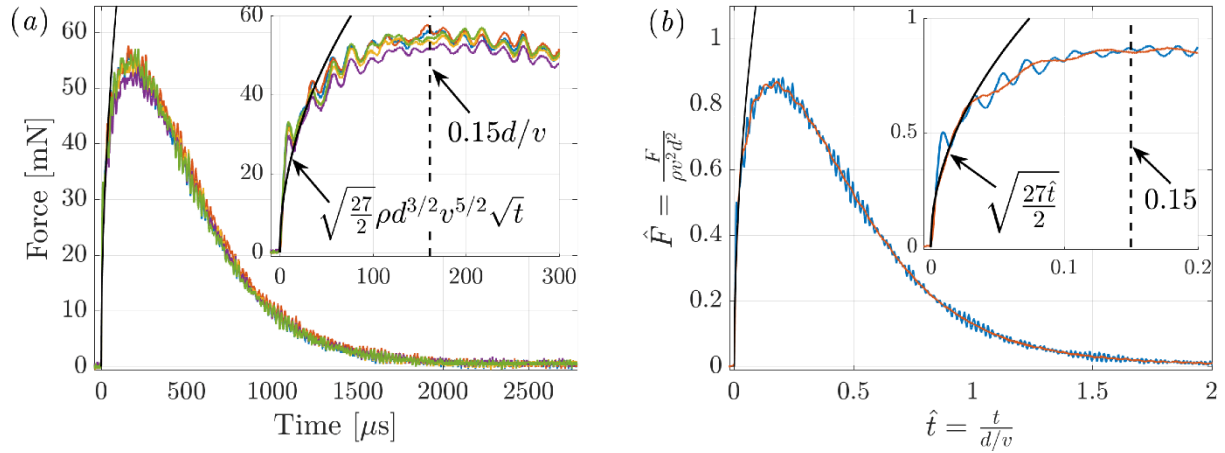


Figure 1.3: Force-time profiles; (a) measured force profiles for the five trials of test condition 11 and (b) their ensemble-averaged (blue) and filtered non-dimensional force profile (orange). Insets show the initial rise and peak force compared with the analytical force (black) from [19]. The peak force occurs at approximately $\hat{t} = 0.15d/v$, shown with a black dashed line.

1.2.3 Peak force

There are currently no theories that explain why the deformed droplet exhibits vertical side walls at the time of peak force. It can be intuitively surmised, however, that at this

time the largest amount of wall-normal momentum is projected onto the impact plane leading to the largest normal force. Consider the deformed droplet configuration before peak force, if the lamella is neglected, the droplet side walls near the base are curved inward and the area projected onto the surface is less than the area of a circle with diameter, d , see Figure 2.1. At peak force, the side walls are perpendicular to the plate and the area projected onto the surface has an area equal to that of a circle with diameter, d . At this time, the momentum within the bulk droplet is purely in the direction normal to the plate. The largest amount of momentum, normal to the plate, occurs at this instant, and from this, it can be reasoned that the largest normal force occurs at this time. After peak force, the projected area is larger, but despite this, the momentum in the bulk has components in the radial direction, as indicated by the radially expanding free surface. Consequently, less momentum is directed in the plate-normal direction, and the impact force drops correspondingly. During this time ($\hat{t} > 0.15$), the upper free surface melds into the spreading lamella, see Figure 2.1. This decay stage is much longer than the pre-peak rise. In terms of the total time duration, the majority of the induced force occurs during the decay.

1.2.4 Normalized Profiles

In terms of the entire experimental range, the measured peak forces cover three orders of magnitude. The peak force of test condition 4 exceeded 1300 mN, while the peak force of test condition 7 was under 3 mN. The profiles of all test conditions exhibit the same qualitative features as displayed in Figure 3.1, but exhibit different peak forces, time durations, etc. See the supplemental material section in [15] for the force profiles of all test conditions. Figure 3.1(b) shows the non-dimensional force profile for the test of Figure

3.1(a) and its respective filtered profile. As is apparent, the filtered profile faithfully adheres to the trend of the unfiltered profile. The normalized profile for each test condition, listed in Table 2, is determined by dividing the force of each respective trial by $\rho v^2 d^2$, and the time by d/v , and then averaging the 5 non-dimensionalized trials of the test condition. This choice of non-dimensionalization employs an inertial set of normalizing parameters (i.e., ρ , v and d). In Figure 3.1(b), the peak force occurs at a non-dimensional time of approximately 0.15 and attains a non-dimensional peak force magnitude of approximately 0.87. Similarly, [21] found the normalized time of peak force and peak force to be 0.18 and 0.85, respectively. Figure 3.1(b) shows the analytical solution derived by [19], compared with the measurements. As shown, the normalized form of Eq. (1.3) compares well with the filtered data up to a normalized time of approximately ($\hat{t} = 0.05$), and then diverges. This demonstrates that the initial impact force scales like \sqrt{t} , as anticipated. Note that Figure 3.1 is representative of inertia-dominated impacts (high Re), and an alternative scaling law must be adopted for viscous drops (low Re).

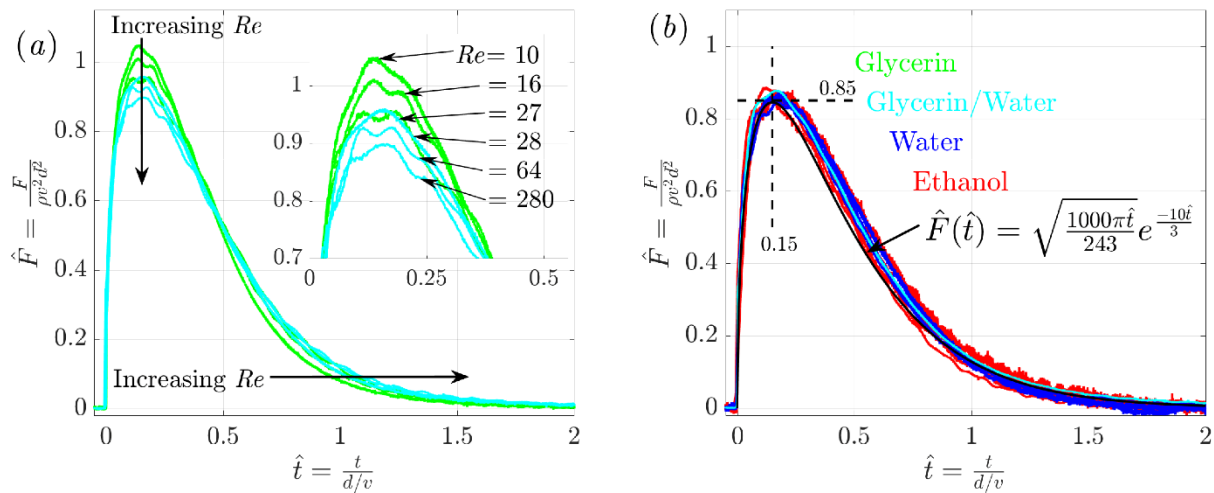


Figure 1.4: Non-dimensional force profiles; (a) test conditions in the viscous regime, $10 \leq Re < 280$, and (b) test conditions in the self-similar inertial regime, $280 < Re \leq 29,800$. The black profile is Eq. (1.8).

The normalized profiles for all test conditions are displayed in Figure 1.4. Figure 1.4(a) shows the force profiles for impacts in the viscous regime, while Figure 1.4(b) shows the force profiles for impacts in the self-similar inertial regime. The viscous regime profiles are noticeably different from inertia-dominated profiles. Namely, they exhibit a greater peak non-dimensional force, and have a shorter non-dimensional time duration. These tests are representative of low Re , (test conditions 1–6), and have their own viscous regime (see Table 2). With increasing Re , in the viscous regime, the force profiles decrease in peak non-dimensional force and increase in non-dimensional time duration, as indicated by the arrows in Figure 1.4(a). The inset of Figure 1.4(a) readily shows how the peak force decreases with increasing Re .

These Reynolds number dependent characteristics of viscous force profiles are in agreement with the results found in [21]. In their study, however, a wider range of Reynolds numbers is explored within the viscous range (down to $Re = 0.7$). Based on the peak time, they propose a quantitative model for the scaling of peak force. The peak time was found to increase with increasing Re , and using this, the peak force is determined through the product of inertial peak force and the ratio of inertial peak time to viscous peak time (see equations 3.18 & 3.20 in [21]). Using this model, the normalized peak force for Reynolds numbers of 10, 16, 27, 28, 64 and 280 (test conditions 1–6), is 1.21, 1.13, 1.06, 1.05, 0.91, 0.87, respectively. In terms of peak force comparison our results exhibit a lower peak force than that anticipated by this model. The difference increases with decreasing Re , where the largest difference is approximately 13 %, at $Re = 10$. This discrepancy is attributed to the initial oscillations induced by impact where the oscillation

amplitude is the greatest, and is, therefore, difficult to identify maximum force. Similarly, a quantitative value for peak time is uncertain due to the oscillation.

The force profiles enter the self-similar inertial regime for approximately $Re > 280$ (test conditions 7–14). In the inertial regime, all profiles share the same profile once normalized. Here, the normalized profile is invariant for variations in Reynolds number (between approximately $280 < Re \leq 29,800$) and Weber number (between $37 \leq We \leq 6,360$). This result has also been observed in other recent studies [21, 42]. It indicates that viscosity and surface tension do not influence the normal force exerted within the given parameter ranges. In this regard, and similar to Figure 1.3, the peak non-dimensional forces, in Figure 1.4(b), are approximately 0.85 and occur at a non-dimensional time of approximately 0.15. Note that the profiles of all test conditions exhibit no observable differences for variations in We , over the present We range. For comparison, Figure 1.4(a), shows test conditions 3 and 4 where their Weber number is 610 and 4,200 respectively, while their Reynolds numbers are relatively unchanged, 27 and 28 respectively. Despite the difference in Weber number, their force profiles are nearly identical, signifying Weber number effects are invariant both in the viscous regime (above $We = 610$) and the inertia regime (above $We = 37$). Therefore, all measurements of this study show Weber number invariance. Similarly, [60, 61] found the droplet spreading radius to be solely Re dependent, with negligible effects due to We . Additionally, [62] has shown that, during deformation, the droplet free surface adheres to self-similarity with Re alone.

1.2.5 Impulse and change in momentum

For all test conditions, the ratio between the measured impulse (i.e., area under the force profile) and the measured droplet momentum $m_e v$, where m_e is the equivalent mass calculated from the imaged droplet diameter d ; $m_e = \pi \rho d^3 / 6$, is between 0.98 and 1.10. Therefore, the impulse exerted by the droplet impact, listed in Table 2, is approximately equal to the droplet momentum just before impact. This provides an indication of the measurement system accuracy, since, by definition, impulse is equal to the change in momentum of an event. See the supplemental materials in [15], for an estimation of the measured force uncertainty [63].

The present droplets undergo a nearly perfect inelastic collision since, after the event, their momentum is zero in the wall-normal direction (the impact surface is assumed rigid), and just before impact, their momentum is mv . Therefore, the total change in momentum is mv (i.e., coefficient of restitution equals zero). It is interesting to note that if a droplet rebounds after impact (i.e., bounces), typically from a hydrophobic surface [64], then the total change in momentum will be larger than mv , since the droplet has a non-zero velocity after its interaction with the surface. This, in turn, will exert a larger impulse, compared to an identically impacting droplet that adheres to the impingement surface. Impacts within the visco-elastic regime, ($Re < 0.7$), do not result in an impulse equal to the drop momentum [21]. In this regime, a negative force is applied to the impact surface as the drop attempts to rebound. The present force profiles show approximately the same non-dimensional impulse, regardless of Re . This indicates that impacts in the viscous and inertial regimes can be modelled as perfectly inelastic collisions.

1.2.6 Free-surface configuration at peak force

The effects of viscosity are present in the deformed droplet configurations at peak force. Figure 1.5 shows the droplets of test conditions 1, 4, 6 and 13 at the time coinciding with the peak in their associated force profile. As previously mentioned, at peak force, the shape of droplets in the self-similar inertial regime have side walls perpendicular to the impact plate (test condition 13 in Figure 1.5), with circumferential side walls equal to their respective droplet diameters, d . This is not the case for impacts in the viscous regime, where the droplet base is bulged and often without a lamella. These viscous impacts do not allow the base of the droplet to reach the vertical side wall condition, making the diameter of the droplet base less than d . In addition, viscous impacts exhibit limited lamella formation owing to the high radial shear stress about the initial point of contact. The viscous stress impedes radial flow near the surface which further increases the volume of liquid about the droplet base, resulting in the observed bulged shape. In contrast, droplets in the inertial regime exhibit weak viscous stresses allowing significant lamellae to form. The effects of viscosity evidently underlie the reason for the shape deviation between the viscous and inertial regimes. In support of this, visual evidence indicates that with increasing Re , lamella jetting develops during the viscous regime, and then becomes unmistakably apparent in the inertial regime, see Figure 1.5, test condition 13. The onset of lamella formation apparently distinguishes the two regimes. This physically reflects the inertial transfer of surface-normal momentum to surface-parallel momentum. Compared to impacts in the inertial regime, where significant lamella jetting occurs, there exists more accumulated (excess) liquid around the base of the viscous regime droplets as they initially deform. This extra liquid promotes a more rapid

momentum transfer to the surface. In fact, [21] show that the pre-peak force rise, for viscous regime droplets, scales as $1/\sqrt{Re}$, leading to a more rapid increase in force for decreasing Re . Accordingly, the peak force is attained sooner and at a higher value than that of the inertial profile. Viscosity has the effect of impeding lamella formation and through this, accumulates more liquid around the base, which induces a faster deceleration of the drop.

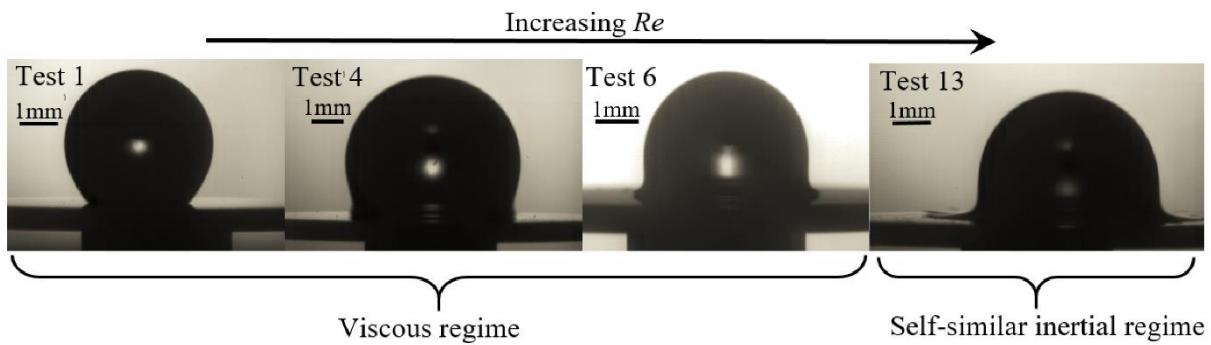


Figure 1.5: Deformed droplet configuration at the time of peak force. From (left) to (right), test conditions 1, 4, 6 and 13, with $Re = 10, 28, 280, 20,700$, respectively. The shape and lamella formation are altered in the viscous regime, while the deformed shape in the inertial regime resembles a dome with side walls perpendicular to the surface. With increasing Re the droplet base goes from curved inward to perpendicular at the time of peak force.

1.2.7 Long-time behavior of inertial profiles

In this section, the post-peak behavior is investigated of force profiles in the self-similar inertial regime. Recall that these are Reynolds and Weber number invariant. The investigation begins after peak force which occurs at a normalized time of approximately $\hat{t} = 0.15$. At the moment of peak force, the droplet side wall is perpendicular to the impact plate, while the upper surface resembles a spherical dome, see Figure 1.5. After peak force, the upper half of the free-surface slowly melds into the radially expanding lamella (slowly compared to the lamella's initial radial velocity, which can be 10 times faster than the drop's impact velocity [61]). Correspondingly, the applied force decays relatively

slowly to zero. We note that the force changes concavity at approximately $\hat{t} = 0.4$. After a normalized time of about $\hat{t} = 2$, the observed force is nearly zero, and the motion of the now pancake-like lamella is radially outward. No forces are recorded during this final spreading phase.

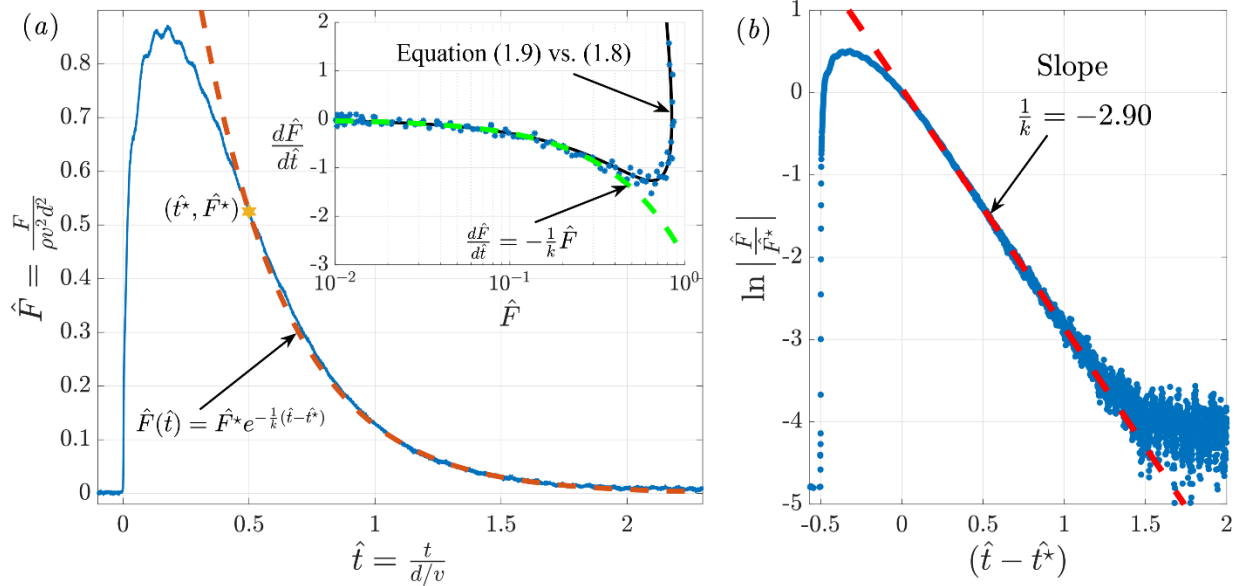


Figure 1.6: Long-time exponential behavior of the inertial droplet force profile. (a) Shows the force profile of test condition 11 with an exponential fit for the post-peak decay (dashed orange line). The decay begins at $(\hat{t}^*, \hat{F}^*) = (0.5, 0.53)$, indicated by the yellow star. The inset shows the force profile's derivative plotted against force (blue). The post-peak force decay adheres to a linear relationship between $d\hat{F}/d\hat{t}$, and \hat{F} , as indicated by the fit line (dashed green line). The black curve is Eq. (1.9) versus Eq. (1.8), indicating the suitability of Eq. (1.8) as a force model. (b) Shows a linear regression of the force profile which is valid between $(\hat{t} - \hat{t}^*) = 0$ and $(\hat{t} - \hat{t}^*) = 15$.

To begin the investigation, first, the time derivative of force is plotted against force in Figure 1.6(a). For values of normalized force below 0.5 and after peak force, the relation between $d\hat{F}/d\hat{t}$ and \hat{F} is linear, as indicated by the fit line $d\hat{F}/d\hat{t} = (-1/k)\hat{F}$, (dashed green line). Note that this is plotted on semi-log axes, so the fit line is curved instead of straight. The derivatives are calculated by the central difference method (first order accurate), on a reduced number of sample points. The fit line diverges from the data when the force is greater than approximately 0.5. This plot suggests that, during this time (i.e.,

0.5 < \hat{t} < 0.2), the time derivative of force is linearly proportional to the applied force. This enables one to employ the following empirical relationship between force and its time rate of change,

$$\hat{F}(\hat{t}) = -k \frac{d\hat{F}}{d\hat{t}}, \quad (1.4)$$

where k is a constant of proportionality. This is effectively a statement that the rate of force transfer is proportional to the available remaining force. Physically, this is treated as a lumped system. In analogy with heat transfer problems where the internal conduction within a body is fast relative to the heat transport across the body surface, the present model assumes that the internal momentum transfer is fast relative to the momentum transfer from the droplet to the surface. This rate-limiting description is consistent with the momentum transport being intimately connected to the impacting droplet shape, as described further below.

To provide further assurance of relation (1.4), the natural logarithm of force is plotted against time. There is a distinguished linear trend from $(\hat{t} - \hat{t}^*) = 0$ to $(\hat{t} - \hat{t}^*) = 1.5$, (i.e., $\hat{t} = 0.5$ to $\hat{t} = 2$). The fit line in Figure 1.6(b) has a slope of $1/k = -2.90$, which is in good agreement with the slope found using the derivative method, $1/k = -2.84$.

Due to the experimental support provided by Figure 1.6, relation (1.4) may be used to approximate the force for times after $\hat{t} = 0.5$. Equation (1.4) specifies that the rate at which force changes is directly related to the applied force and can be readily solved by separation of variables. From (1.4) it follows that

$$\int_{\hat{t}^*}^{\hat{t}} -\frac{1}{k} d\hat{t} = \int_{\hat{F}^*}^{\hat{F}} \frac{1}{\hat{F}} d\hat{F}, \quad (1.5)$$

and thus,

$$\hat{F}(\hat{t}) = \hat{F}^* e^{-\left(\frac{1}{k}\right)(\hat{t}-\hat{t}^*)}, \quad (1.6)$$

where $\hat{F} = \hat{F}^*$ at $\hat{t} = \hat{t}^*$. The linear relationship between force and its derivative, produces an exponential decay which may be used to approximate the long-time force behavior. The slope obtained from the fit line, $1/k = -2.84$, is used to approximate the force in the main plot of Figure 1.6(a) as an exponential (dashed orange line), and as shown, is in convincing agreement with the measurements (after $\hat{t} = 0.5$). Notice that the exponential fit begins to merge with the data at a normalized force of approximately 0.5. The starting point for the exponential decay begins at approximately $(\hat{t}^*, \hat{F}^*) = (0.5, 0.53)$. Note that the decay is not due to relaxation of the force sensor, as it can accurately measure dynamic loads of durations longer than 2 s (discussion on sensor decay (personal communication), PCB Piezotronics, Inc., 2018).

1.3 Force model

In this section a model equation is formulated that accurately represents the full force evolution of a droplet impinging normal to a flat rigid surface. It is assumed that the droplet Reynolds number is high and within the self-similar inertial regime. The functional form for the equation is strategically chosen from previous analytical works, while utilizing the decay model and physics educed in the present study. As previously discussed, during initial deformation, the center pressure exerted by an impinging droplet obeys a $1/\sqrt{t}$

dependence [19, 46, 47], and maintains this pressure dependence for approximately $\hat{t} = 0.5$. Our measurements show that at this time, $\hat{t} = 0.5$, the peak force has already occurred, and the force is diminishing to zero. Thus, for the initial impact force, we assume the average pressure applied on the surface has a $1/\sqrt{t}$ dependence. In addition, the spreading radius has been found to obey a \sqrt{t} dependence [61, 65, 66]. A functional form for the force profile is constructed via the product of the contact area and contact pressure. Hence, the force should obey a \sqrt{t} dependence, as analytically predicted by [19], however, this is unsuitable for large time, since \sqrt{t} diverges. Thus, in accordance with the analysis in section 1.2.7, an exponential decay is included for large times. This simultaneously preserves the \sqrt{t} dependence for the initial deformation, while bounding the function for large time. Furthermore, it is noted that the use of an exponential has shown previous success as a fitting function to match the numerical predictions of the central pressure decay for times on the order of d/v , [48]. The model equation is then

$$F(t) = c \sqrt{\frac{t}{\tau}} e^{-t/\tau}, \quad (1.7)$$

where c and τ are constants. For small time, ($t < 0.1d/v$), Eq. (1.7), behaves like \sqrt{t} , as anticipated, since the exponential approximates unity for small time. Constants, c and τ can be estimated from the present experiments. The impulse is experimentally well approximated by the measured momentum of the droplet. Therefore, equating the integral of $F(t)$ over all positive times to mv , yields $\sqrt{\pi c \tau}/2 = mv$. The time to peak force is experimentally found to occur at approximately $t = 0.15d/v$. Accordingly, the time

derivative of $F(t)$ is set equal to zero at $t = 0.15d/v$, from which one can obtain $\tau = (3/10)d/v$ and $c = (10\sqrt{\pi}/9)\rho d^2 v^2$. With these constants, the non-dimensional form of Eq. (1.7) becomes,

$$\hat{F}(\hat{t}) = \sqrt{\frac{1000\pi\hat{t}}{243}} e^{-10\hat{t}/3}. \quad (1.8)$$

Equation (1.8) is plotted in Figure 1.4(b), as a solid black line. As shown, Eq. (1.8) well approximates the force profiles of the droplet impacts in the self-similar inertial regime. Here, it is relevant to note that the analytically derived constant before the $\sqrt{\hat{t}}$ term, in Eq. (1.3) by [19], is remarkably close to our constant, $\sqrt{c^2/\tau}$. In fact, if our constant, $\sqrt{c^2/\tau}$, is replaced by $\sqrt{27/2}\rho d^{3/2}v^{5/2}$ and is used to solve for the time to peak force, using the same integral and derivative condition, then the time to peak force occurs at $t = 0.148d/v$, extremely close to our experimental observation of $t = 0.15d/v$. It is interesting to note that if $\sqrt{c^2/\tau}$ is equal to $\sqrt{27/2}\rho d^{3/2}v^{5/2}$ then Eq. (1.7) is asymptotic to Eq. (1.3) as $t \rightarrow 0^+$, i.e., early-time solution of [19]. Moreover, the derivative of Eq. (1.8) compares well with the experimentally determined derivatives. The derivative of Eq. (1.8) with respect to time is,

$$\frac{d\hat{F}}{d\hat{t}} = \sqrt{\frac{1000\pi\hat{t}}{243}} \left(\frac{1}{2\hat{t}} - \frac{10}{3} \right) e^{-10\hat{t}/3}, \quad (1.9)$$

and is plotted against Eq. (1.8) in Figure 1.6(a) inset (black). As is apparent, the black curve in Figure 1.6(a) closely follows the data, indicating the suitability of Eq. (1.8) as an accurate force model.

1.4 Long-time force decay measured from free-surface height evolution

The results of the previous section support the treatment of the decaying portion of the force curve using a lumped momentum transport model. The linear dependence between the force and the force decay rate supports the efficacy of this modelling assumption. Physically, a lumped approach also suggests that the momentum transport is rate-limited owing to processes at/near the droplet/surface interface. The corollary to this is that momentum gradients are small over most of the droplet volume. In this section, this assumption is used to construct a model for the force that is based solely on the movement of the upper free surface of the droplet. The results from this exercise further reinforce the validity of the lumped model.

For modelling purposes, assume that the impact is in the self-similar inertial regime and that the droplet is axially symmetric. Given this, the velocity within the fluid domain can be described in cylindrical coordinates as $\vec{v} = u(r, z, t)\hat{r} + w(r, z, t)\hat{z}$, with axial momentum $p = p(r, z, t)$, which can be written as,

$$p(t) = \int_V \rho w dV. \quad (1.10)$$

Here the differential volume is the area of width dr and height h revolved about the z -axis, (i.e., $dV = 2\pi hr dr$). The free surface is denoted by $z = h(r, t)$. Consistent with the

lumped model assumption introduced and validated in the previous section, the momentum variations within the droplet are taken to be negligible. Under this assumption the axial velocity within the drop is that given by the free surface. The momentum then becomes,

$$p(t) = 2\pi\rho \int_0^{R(t)} \frac{\partial h}{\partial t} h r dr, \quad (1.11)$$

where $R(t)$ is the spreading radius of the drop. For large time the axial momentum near $r = R(t)$ (i.e., in the lamella region) is approximately zero. The droplet fluid near the edge of the lamella does not contribute a significant normal force compared to the droplet fluid near the impact point ($r = 0$). For this analysis, the spreading radius is fixed to $R(t) = d/2$, which, as will be shown, is a sufficient distance away from $r = 0$ to yield accurate force estimations. To normalize the momentum, p is divided by the inertial parameters of the system; liquid density ρ , droplet diameter d , and the initial impact velocity v . This is given by,

$$\hat{p} = \frac{2\pi\rho \int_0^{d/2} \frac{\partial h}{\partial t} h r dr}{\rho d^3 v}. \quad (1.12)$$

In terms of non-dimensional variables, Eq. (1.12) becomes,

$$\hat{p} = 2\pi \int_0^{1/2} \frac{\partial \hat{h}}{\partial \hat{t}} \hat{h} \hat{r} d\hat{r}. \quad (1.13)$$

Now an equation is obtained for the impinging droplet momentum that is solely a function of the free-surface height. Upon differentiation with respect to time, the resulting force is given by,

$$\hat{F} = \frac{d\hat{p}}{d\hat{t}} = 2\pi \frac{d}{d\hat{t}} \left(\int_0^{1/2} \frac{\partial \hat{h}}{\partial \hat{t}} \hat{h} \hat{r} d\hat{r} \right). \quad (1.14)$$

From high-speed imagery one can determine the height evolution of the impinging droplet at different radial locations. The height evolution of 35 radial positions from $r = 0$ to $r = d/2$ in increments of 0.04 mm was recorded and is presented in Figure 1.7(a–c). Figure 1.7(a) shows the height as a function of radial position, while Figure 1.7(c) shows the height as a function of time for each radial location. Figure 1.7(b) shows the upper free surface for $\hat{t} > 0$. This height evolution is for test condition 11 and is representative of height evolutions in the inertial regime. Figure 1.7(d) shows the normalized momentum as a function of time calculated using Eq. (1.13). The derivative of this curve is the estimated force (per Eq. (1.14)) and is presented with the direct force measurements in Figure 1.7(e). As is apparent, the estimated force using the free-surface height closely adheres to the direct force measurements for $\hat{t} > 0.5$. The advantage of this technique is that it allows one to determine the normal force induced by droplet impacts with only knowledge of the free-surface height evolution (valid only for $\hat{t} > 0.5$). Its efficacy also reinforces the physics of the lumped model employed to describe the momentum transfer from the droplet to the surface.

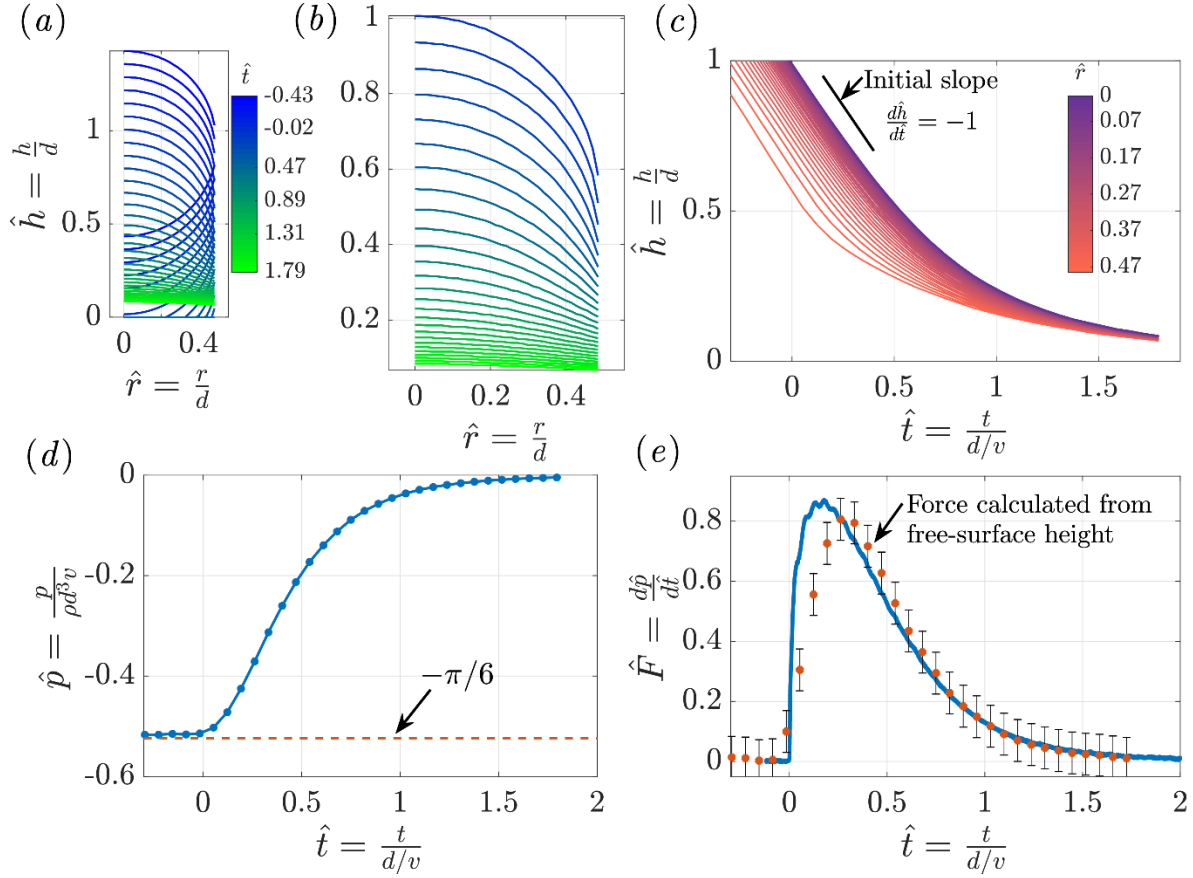


Figure 1.7: (a) Free-surface height evolution of test condition 11 measured at radial locations $0 \leq \hat{r} \leq 0.5$. (b) Shows the upper free surface for $\hat{t} \geq 0$. (c) Shows the height evolution as a function of time for each radial location. (d) Shows the total momentum calculated from the free-surface height Eq. (1.13), and (e) shows the force approximation of Eq. (1.14), compared to the measured force profile. The approximation is valid for the post-peak decay ($\hat{t} > 0.5$). Error bars are based on the camera's spatial and temporal resolution.

The force predicted by Eq. (1.14) is apparently valid for long time, however for early time the model underestimates the induced droplet force. Before impact (i.e., $\hat{t} < 0$), the drop travels toward the plate with a uniform axial momentum of $\hat{p} = -\pi/6$. Once impact occurs the drop momentum immediately decreases due to the decreasing drop volume used in Eq. (1.13). It is noted here that the lower free surface is approximated by a truncated falling sphere with velocity v , which exists for $\hat{t} < 0.5$ (see Figure 1.7a). The reason for using this model instead of the actual lower free surface is due to the erroneous effects

of the radially growing lamella and bulging of the droplet base. Owing to continuity, the impact increases the volume of liquid at the base, and in effect increases the axial velocity of the lower free surface violating the uniform momentum assumption. The use of a truncated sphere model renders the momentum uniform during the early stages of impact (i.e., when the upper free surface continues to travel at a velocity v , see Figure 1.7c). It is apparent that this model captures the sudden increase in force, however the prediction falls below the measured force response. This discrepancy is likely due to the momentum inhomogeneity during the early stages of impact [19]. The variation between the self-similar fields concentrated about the impact region and the remaining bulk of the droplet violate the uniform momentum assumption. Therefore, this model, Eq. (1.14), can only approximate the drop-induced force once the fields establish uniformity.

Another important quantity describing the droplet impingement process is the central height evolution, defined as $\hat{h}(0, \hat{t}) = \hat{h}_c(\hat{t})$. This quantity is indicative of the impact process, as it provides useful insight into underlying scales of the problem and reveals whether the impact process may be considered inertial. In addition, the central height is representative of the axial free-surface evolution. As is apparent in Figure 1.7(c), the majority of the upper free surface follows the trend of the central height (most purple color). For early time and before impact, the central height is simply ballistic, adhering to the functional form: $\hat{h}_c = 1 - \hat{t}$. As deformation ensues the central height progressively slows down and approaches a constant minimal film thickness [62]. The transition between the ballistic and constant film thickness regime has been shown to admit a self-similar form, for large Reynolds numbers, where the central height behaves as,

$$\hat{h}_c = \frac{A}{(\hat{t} + \hat{t}_0)^2}, \quad (1.15)$$

where constants A and \hat{t}_0 , are approximately 0.492 and 0.429, respectively [62]. The central height evolution of all test conditions is presented in Figure 1.8(a). Notice that the low Reynolds number impacts $Re < 280$, tend to a greater constant film thickness, while the high Reynolds number impacts, within the self-similar inertial regime, exhibit a very similar central height evolution. This becomes more apparent in the Figure 1.8(a) inset, where the height is plotted on a logarithmic scale. This reveals the transition from the ballistic to the self-similar regime Eq. (1.15), and how the viscously influenced impacts (i.e., for $Re < 280$) deviate from the inertial height evolution Eq (1.15). The central height is undoubtedly an important physical parameter. Thus, the dependence of droplet force on central height is now investigated.

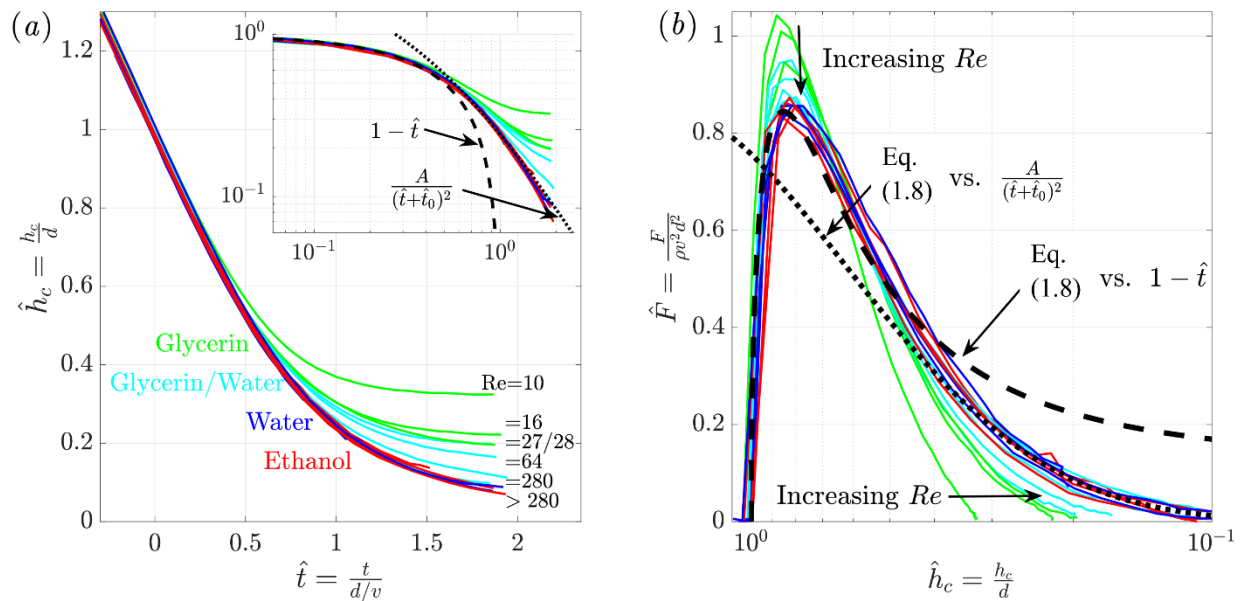


Figure 1.8: (a) Central height evolution $\hat{h}(0, \hat{t}) = \hat{h}_c(\hat{t})$, for all test conditions. Inset shows the data plotted on a logarithmic scale, with the black-dashed line representing the ballistic regime and the black-dotted line representing the self-similar inertial regime [62]. (b) Shows the impact force versus the central height. Equation (1.8) versus the ballistic and self-similar regimes are plotted with black-dashed and black-dotted lines, respectively.

In Figure 1.8(b) the force profiles of all test conditions are plotted with respect to their central heights. It is apparent that a large increase in force occurs when the height is about 1 (i.e., near initial impact), reaching a peak around $\hat{h}_c = 0.8$. It is interesting to note that this height is approximately the height of a geometric dome (with vertical side walls) whose volume is equal to that of a sphere with equal radius. After reaching peak force, the force then decreases less rapidly as it approaches zero. Figure 1.8(b) also reveals the separation between inertial self-similar profiles and the ones affected by viscosity. The viscous profiles have a higher peak force and decreases more rapidly until reaching their constant film thickness. It is apparent that with decreasing Reynolds number, the peak force increases along with the constant film thickness, while tending towards a symmetric profile. Conversely, all of the inertial profiles tend towards an invariant profile, further supporting their self-similar nature.

The inertial force profile, represented by Eq. (1.8), is plotted versus the ballistic $(1 - \hat{t})$, and inertial height evolutions, i.e., Eq. (1.15), with black-dashed and black-dotted lines, respectively. Notice that for early time, the profiles tend to follow the ballistic-dependent force (black-dashed line), while the long-time profiles tend toward the inertially dependent force (black-dotted line). The level of agreement between these predictions and the measurements further supports the force model given by Eq. (1.8).

1.5 Summary

The impact force of liquid droplets on a flat rigid surface are measured across a wide range of Reynolds and Weber numbers, four and two decades, respectively. The experiments are conducted in a sub-atmospheric pressure environment as to inhibit air-drag-induced distortion, which allows the droplets to remain spherical upon impact. When plotted non-dimensionally, the force profiles exhibit a self-similar inertial and a viscous regime, distinguished solely by the Reynolds number. The measurements also show that the force profiles are invariant with respect to Weber number. For high Re flows, the droplet impact process is inertially dominated as the only influential parameters are liquid density, impact velocity and droplet diameter. Interestingly, for inertially dominated impacts, the peak force occurs when the deformed droplet resembles a geometric dome with side-walls that are perpendicular to the impact plane. Furthermore, the experiments reveal an exponential post-peak decay in the force profile. This permits the long-time force behavior to scale as e^{-t} , and is shown to be consistent with a lumped model approximation for the momentum transport from the droplet to the surface. Overall, a single, accurate model equation is constructed for the scaling of force profiles across a wide range of Reynolds and Weber numbers. This model incorporates the \sqrt{t} short-time

behavior, analytically deduced by previous researchers, and the well-supported linear dependence between $F(t)$ and dF/dt , shown herein. This model is believed to provide a useful contribution owing to the ubiquitous occurrence of droplet impacts in nature and in industrial applications, such as in water droplet machining.

2. IMPACT FORCE OF RAYLEIGH JETS

(Text for this chapter is taken from [16], i.e., Mitchell, B. R., Klewicki, J. C., Korkolis, Y. P., & Kinsey, B. L. (2019). Normal impact force of Rayleigh jets. *Physical Review Fluids*, 4(11), 113603. My contributions to this work were all experimental and theoretical investigations.)

The impact of a liquid jet is used in numerous applications, e.g., surface cleaning [67], cooling [68, 69], coating and ink-jet printing [70], surgical applications [71, 72], and medicine delivery [73]. In most of these applications, a liquid is accelerated through a circular orifice that initially forms either a continuous, axisymmetric, cylindrical (Rayleigh) jet or is emitted as a disorganized mass of liquid droplets by a process known as atomization [74]. Many of the applications listed above utilize the former process, where an initially continuous stream of liquid travels a certain distance from the orifice until colliding with a surface. The purposes of surface impingement vary depending on the application. In coating flows or ink-jet printing, for example, it is often desirable to efficiently deposit the liquid onto the surface while minimizing splash [75, 76] (i.e., in order to enhance print quality). In surface cleaning or waterjet cutting, it is advantageous to maximize the stress imparted onto the surface (i.e., to remove dirt or to penetrate the surface for effective material removal). Upon impact with the surface, however, the liquid in the emanating jet can exhibit two distinctly different states: (i) the liquid remains intact as a continuous, axisymmetric jet, depicted in Figures 2.1(a) and 2.1(b); or (ii) the liquid jet fragments, downstream of the orifice, into a train of discrete droplets due to a surface tension induced instability [5], shown in Figure 2.1(c). Regardless of the intended application, the characteristics of the impact (i.e., splash, induced force, etc.) will change

depending on whether the liquid is in a droplet state upon impact or remains as a continuous jet. Here, it is recognized that a Rayleigh jet constitutes any of the Figure 2.1 depictions, as the only differences between these jets are their perturbation amplitudes and whether these amplitudes are large enough to permit droplet formation. The state of the liquid arriving normal to the impingement surface is then governed by the perturbation amplitude and the nozzle to plate distance, as described, in detail, in chapter sections 2.1 and 2.2.

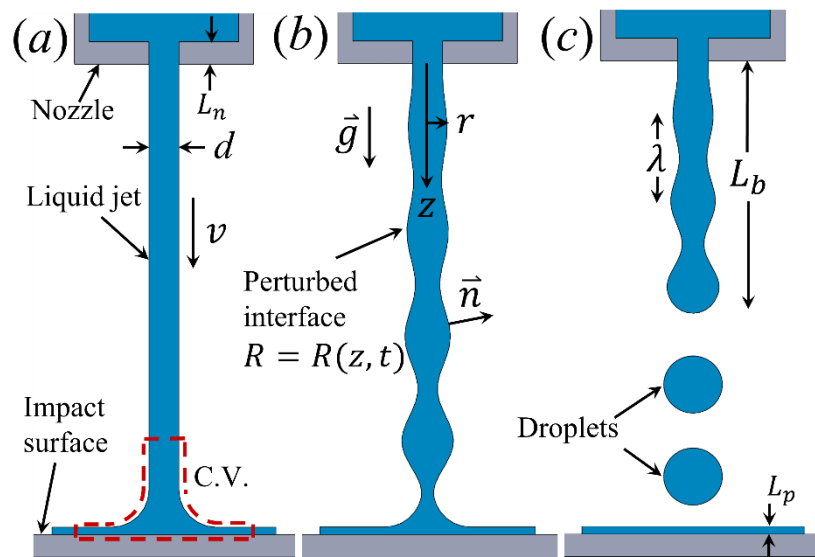


Figure 2.1: Schematic of the normal impingement of Rayleigh jets: (a) steady-state jet, (b) wavy jet, and (c) droplet train.

The droplet formation process from a continuous jet has received considerable attention since the pioneering work of Lord Rayleigh [5, 77, 78]. Similarly, the impact of a single droplet onto a flat solid surface has received a wealth of scientific interest, with particular attention paid to the underlying splashing mechanisms [29, 79]. A less prevalent research topic is the associated impact of continuous jets, and droplet trains onto flat solid surfaces, and especially the induced normal force. This area remains largely unexplored; however,

knowledge of the force induced by Rayleigh jets is of practical use in industrial applications, like water droplet machining, and is of broad scientific interest. In fact, as a unique example, archer fish (*Toxotes jaculatrix*) attack their above-surface prey with precisely aimed waterjets [80].

In this chapter, the similarities and differences of the normal impingement of a steady-state jet, a wavy jet, and a droplet train, onto a solid surface are investigated through force measurements and high-speed photography. The aim is to quantify the force imparted by these distinctly different scenarios for identical nozzle flow conditions (i.e., velocity and jet diameter). In this way, the momentum exiting the nozzle is identical for each condition, allowing for direct comparison. A quantitative understanding in the applied force of Rayleigh jets allows applications to be designed with sufficient foresight, and aids in determining whether the use of droplets is appropriate and beneficial.

This chapter begins with the regimes associated with the “breakup” of liquid jets in section 2.1, followed by a description of the droplet formation process in section 2.2. That section also characterizes the jet free-surface, which is used to formulate model equations for the force induced by continuous jets in section 2.3. Section 2.4 elucidates the force imparted by a single droplet, which is used in series to formulate a model equation for the force induced by a droplet train. These force models are then experimentally tested. In section 2.5 the experimental setup and data processing methods are introduced. This is followed by results and discussion in section 2.6, and finally, concluding with a chapter summary in section 2.7.

2.1 Classification of jet regimes

Liquid issuing from a circular nozzle has several outcomes. If the flow rate exiting the nozzle is relatively small, and there exists a quasistatic balance between the liquid inertial/gravitational force and the surface tension force, then the liquid simply drips [81] (i.e., a leaking faucet). As the flow rate increases, the liquid takes the form of a cylindrical “Rayleigh” jet, where the jet appears smooth and unperturbed close to the nozzle. The onset between the dripping regime and the Rayleigh regime occurs when the Weber number (ratio of inertial to surface tension force) exceeds a critical threshold, described by

$$We = \frac{\rho d_0 v_0^2}{\sigma} > 8, \quad (2.1)$$

where d_0 is the jet diameter, v_0 is the jet velocity relative to the nozzle, ρ and σ are the previously defined liquid density and surface tension, respectively [82–84]. A formal description of the transition from dripping to jetting can be found in [85]. Once in the Rayleigh regime, the liquid exiting the nozzle is initially columnar; however, at a certain distance downstream, wavy disturbances about the free-surface become discernible. These disturbances grow progressively in amplitude downstream until the wave amplitude becomes approximately equal to the jet radius. This is where droplet formation occurs [86]. The distance between the nozzle and the point of droplet formation is defined as the breakup length L_b , see Figure 9(c), and is linearly proportional to the jet velocity. More specifically, the normalized breakup length scales with the square root of the jet’s Weber number (i.e., $L_b/d_0 \propto We$) [78, 87–91]. This relation, however, is valid only for a

certain range of Weber numbers. As the jet velocity increases, the surrounding fluid into which the jet is immersed (typically air) begins to alter the Rayleigh regime dynamics. Aerodynamic drag causes droplet formation to occur earlier, shortening the breakup length. The breakup length begins to decrease nonlinearly with jet velocity, and the jet enters the first wind-induced regime [78]. This occurs when the aerodynamic force is about 10% of the surface tension force [92]. A further increase in the jet velocity allows the surrounding fluid to induce significant shearing stress onto the jet. This causes droplets to be stripped off the surface, rather than being pinched off in segments at the fore of the jet [86]. The jet then enters successive wind-induced and atomization regimes. The topic of this chapter focuses solely on Rayleigh jets. A comprehensive review of the subsequent regimes can be found in [78, 83, 87, 93]. The upper bound separating the Rayleigh regime from the first wind-induced regime is described by

$$We < 0.4 \frac{\rho}{\rho_{gas}}, \quad (2.2)$$

where ρ_{gas} is the density of the ambient gas [83, 84, 93]. For the experiments reported in this paper, which are conducted in standard atmosphere, the critical upper bound for velocity is 3.8 m/s. Note that Eq. (2.2) predicts that the Rayleigh regime can be extended to higher jet velocities if the surrounding atmospheric pressure is reduced. This widening of the Rayleigh regime has been experimentally verified by Fenn and Middleman in a sub-atmospheric pressure environment [94]. This motivates the use of a vacuum chamber, in water droplet machining, so that a high-speed Rayleigh jet can be produced.

2.2 Droplet formation from Rayleigh jets

As previously mentioned, a Rayleigh jet is characterized by an initially continuous, unbroken stream of liquid emanating from a nozzle that with downstream evolution may break apart into discrete droplets due to surface tension-induced instabilities. If a flat solid surface is positioned normal to the jet, before the region where wavy disturbances become noticeable, then the liquid is diverted radially along the surface, as depicted in Figure 2.1(a). If the radial disturbances have sufficiently large amplitudes, droplet formation will occur closer to the nozzle, and a flat solid surface positioned past the breakup length will experience a series of droplet impacts, like that shown in Figure 2.1(c). Figure 2.1(a) is a highly idealized scenario as disturbances are likely to occur and grow in amplitude almost immediately after the nozzle exit. There exists an intermediate scenario between the steady columnar jet impact and the droplet train impact. In this scenario, the solid surface will experience a series of continuous wave impacts, like that depicted in Figure 2.1(b). If viscous effects of the impinging jet can be neglected, and the Weber number satisfies Eqs. (2.1) and (2.2), then predicting the state in which the liquid arrives at the surface is accomplished through Rayleigh jet theory.

2.2.1 Plateau's reasoning

The first attempt to characterize the droplet formation process was done by Plateau in 1873. At this time, it was known that liquids possess a binding force at their free surface, i.e., surface tension (N/m in S.I. units) or surface energy (J/m²). In terms of total surface energy, a given volume of liquid can exhibit different surface areas (depending on its shape), which correspond to different surface energies. Based on the principle of

minimum potential energy, Plateau reasoned that an axisymmetric, wavy liquid column of radius,

$$R(z) = R_0 + ae^{ikz}, \quad (2.3)$$

where R_0 is the mean column radius (i.e., $R_0 = d_0/2$), $a \ll R_0$ is the wave amplitude, $i = -1$, and k is the wave number, exhibits a smaller surface area (and thus a lower potential energy) than that of a straight cylindrical column of equal volume, if the wavelength, $\lambda = 2\pi/k$, is larger than the column's circumference [95]. This principle of energy minimization essentially derives from the second law of thermodynamics and permits the unstable wavy liquid column to discretize into droplets whose combined surface area is less than that of the original column. Disturbances or waves that are non-axisymmetric (i.e., azimuthal modulations) are stable [78, 96, 97]. For axisymmetric jets, only wave numbers in the range $0 < kR_0 < 1$ are unstable and lead to droplet formation. Although a critical finding, this range does not identify which wave(s) are most dominant or how rapidly different waves grow in amplitude.

2.2.2 Rayleigh's local analysis

Using the equations of motion, Rayleigh determined the wave number associated with the most rapid wave amplitude growth. He considered the evolution of small axisymmetric perturbations about the free surface of a quiescent, inviscid, infinitely long liquid cylinder, with radius R_0 , density ρ , and surface tension σ , in the absence of gravity. These small perturbations (i.e., waves) allow linearization of the momentum equations, which, with the continuity equation and appropriate boundary conditions, yield their temporal growth

rates, ω . In Rayleigh's analysis, the free-surface takes the form of a perturbed sinusoidal column about the axial direction z , as described by,

$$R(z, t) = R_0 + ae^{\omega t + ikz}, \quad (2.4)$$

where ω and k are the previously defined growth rate and wave number, respectively. Negative values of ω lead to wave stabilization, while positive values lead to wave steepening and imminent droplet formation. The prominent result of Rayleigh's analysis is a dispersion relation. This describes the dependence of the wave growth rate on wave number, and it is given by

$$\frac{\rho\omega^2 R_0^3}{\sigma} = kR_0 \frac{I_1(kR_0)}{I_0(kR_0)} (1 - k^2 R_0^2), \quad (2.5)$$

where I is the modified Bessel function of the first kind. This relation is plotted in Figure 2.2. The wave number of the fastest growing wave is $kR_0 = 0.697$. Other waves can, however, lead to the discretization of the column if their initial amplitudes are sufficiently large. It should be noted that this linearized wave model accurately describes the early stages of jet segmentation. The actual pinch-off of the droplet can only be described by nonlinear theories [98]. The infinite column is allowed to travel in space with some arbitrary velocity, but waves do not propagate upstream or downstream with respect to the bulk flow. In this regard, Rayleigh's analysis can be seen as a local theory, as every wave along the column is identical to the wave upstream or downstream of it. Therefore, one only needs a portion of the column, $\lambda = 2\pi/k$, to completely describe its

characteristics. This is obviously not the case for finite liquid jets issuing from nozzles, as waves progressively grow in amplitude along the axial direction.

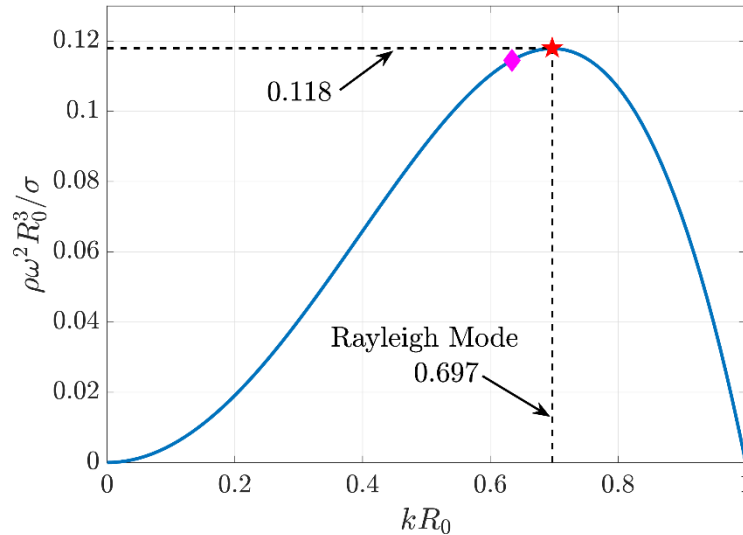


Figure 2.2: Rayleigh’s dispersion relation; identifying the dependence of wave growth rate on the normalized wave number kR_0 . The fastest growing wave (Rayleigh mode) occurs for $kR_0 = 0.697$, labeled with a red star. The wave number at impact for the present experiments is $kR_0 = 0.634$, and it is represented with a purple diamond.

2.2.3 Spatial analysis

Rayleigh’s analysis can be extended to liquid jets issuing from nozzles in a commonly used spatial theory [99–102]. In this theory, waves grow in amplitude along the z direction, rather than in time. This fixes the breakup length for steady-state jets, and is the case for our experiments. This spatial description of the free surface is the intuitive choice for the laboratory reference frame; however, there are certain assumptions that must be made. Namely, the temporal characteristics propagate downstream in the axial direction with the same velocity of the jet. This requires one to define a new parameter: the spatial wave frequency, K , which connects to the temporal wave number as $K = k = 2\pi/(vT)$, where T is the period of temporal oscillation. The period is related to the frequency by $T = 1/f$,

and the wavelength is then $\lambda = vT$. The temporal wave growth rate is related to the spatial growth rate β , through $\beta = \omega/v$. With these considerations, the free-surface of the jet takes the form,

$$R(z, t) = R_0 + ae^{\beta z} \cos(Kz - 2\pi ft + \phi), \quad (2.6)$$

where ϕ is the phase of the wave, which is arbitrary and depends on the time in which the analysis starts. The nozzle location is at $z = 0$, with positive z being the direction toward the impact surface (see Figure 2.1). Equation (2.6) indicates that the waves oscillate both in time and in space. When traveling with the wave velocity, an observer will simply see wave amplitude growth and then droplet formation. If at a fixed z location, then the observer sees waves of equal amplitude (or droplets) pass by at a rate given by f . If one droplet is produced per wavelength, then by mass conservation the diameter of the droplet D , is given by $D = (1.5\lambda d_0^2)^{1/3}$. For the Rayleigh mode, $\lambda = d_0/0.697$, the droplet diameter is nearly twice the jet diameter (i.e., $D = 1.89d_0$). Despite this, most studies [84, 103-105] show a range of droplet diameters within two distinct subsets, namely primary droplets and satellite droplets, which are significantly smaller than primary drops. Rayleigh theory does not predict satellite droplet formation, as this theory is strictly linear and only considers small perturbations from equilibrium. The formation of satellite droplets can be anticipated from nonlinear theories where breakup profiles are self-similar [106]. Satellite drops form in between primary droplets at the breakup length L_b . Although the breakup length is typically considered constant, it may vary slightly from each droplet pinch-off. It has been shown that the breakup length is well represented by a Gaussian

distribution, with Gaussian width proportional to the jet velocity [87, 88, 93]. This natural breakup length may be artificially shortened through wave-number stimulation.

2.2.4 Stimulated droplet formation

A number of methods have been used to stimulate jets in order for droplets to form closer to the nozzle. This may be done through elliptically-shaped nozzles [89, 96, 97], piezoelectric vibration [107], reservoir pressure oscillation [91], or simply by exploiting any periodic disturbance in the vicinity of the jet, which may be an audio speaker placed next to the nozzle exit [108]. Depending on the stimulation frequency f , these methods generate a large initial wave amplitude a , that is specific to the excited wavelength λ . This allows certain wave numbers to become the dominant wave (instead of the Rayleigh wave) and thus the wave responsible for droplet formation. A range of wave numbers may be stimulated, but only those in the range $0 < kR_0 < 1$ permit droplet formation. Due to the increased amplitude, artificial stimulation enables droplets to form sooner and thus closer to the nozzle. Other means may be used to shorten the breakup length, such as the choice of nozzle geometry.

2.2.5 Effects of nozzle geometry

The velocity profile exiting the nozzle is important, especially if precise control of the breakup length is required. Nozzles with short aspect ratios ($L_n/d_n < 1$), where L_n is the nozzle length (see Figure 2.1) and d_n is the nozzle diameter, are more stable and produce more consistent droplets than nozzles with long aspect ratios [93]. Pipe flow turbulence associated with long nozzle aspect ratios leads to moderate shortening of the breakup length [109]. Although the nozzle aspect ratio affects the breakup length, it also influences

the diameter of the jet itself, as the jet diameter d_0 , may not necessarily equal the nozzle diameter d_n . The study of [110] shows that the contraction ratio $\chi = d_0/d_n$ is dependent on the jet Reynolds number, defined as $Re_n = \rho d_n v_0 / \mu$, where μ is the previously defined fluid viscosity. Contraction of the jet (i.e., $\chi < 1$) occurs for $Re > 16$, while expansion (i.e., $\chi > 1$) occurs for $Re < 16$ [110]. For example, $Re = 100$ liquid flow through a nozzle of aspect ratio $L_n/d_n = 0.5$ exhibits about 7 % contraction. The velocity profile relaxation is completed after liquid from the nozzle travels approximately one nozzle length; after this, the jet diameter remains unchanged [110]. This indicates that for short nozzle aspect ratios, the jet diameter d_0 may be assessed close to the nozzle.

2.2.6 Other analyses

Rayleigh's analysis shows that the droplet formation process is governed purely by the growth of capillary waves whose wavelength is a function of the liquid properties and jet diameter only. It is worth noting that Rayleigh's theory has been extended to other analyses conducted by Weber [111], Yuen [112], Sterling and Schleicher [92], and Leib and Golstein [99], which take into account the fluid viscosity, velocity, nonlinearity, and effects of ambient air. The effects of viscosity tend to decrease the growth rate and increase the dominant wavelength [86]. For the purposes of the present analysis, the spatial form of Rayleigh's theory is instructive as it elucidates the droplet formation mechanisms and accurately represents the jet free-surface, which can be used to yield accurate models for the induced force of real jets.

2.3 Force induced by continuous jets

2.3.1 Steady state jets

The steady-state normal impingement force of a continuous unperturbed jet, like that depicted in Figure 2.1(a), can be determined through control volume analysis. The volume considered is the curved area at the base of the jet in contact with the surface revolved about the z axis. It is assumed that the incoming flow is uniform with velocity v , in the z direction, and the outward deflected radial flow travels purely in the r direction. The jet Reynolds number is assumed to be sufficiently high such that viscous effects are negligible. With these considerations, the integral momentum equation may be applied to the control volume to yield the jet impact force,

$$F = \frac{\pi}{4} \rho v_0^2 d_0^2. \quad (2.7)$$

The parameters ρ , v_0 , and d_0 provide an inertial set of normalizing parameters, such that the nondimensional form of Eq. (2.7) is $\hat{F} = F/(\rho v_0^2 d_0^2) = \pi/4$. Equation (2.7) is effectively a statement of momentum conservation, as the plate simply diverts the jet momentum from the axial to the radial direction.

If gravitational effects are considered, then the jet velocity increases with increasing z and the jet radius contracts as a consequence of mass conservation. The velocity in the axial direction at the moment of impact is defined as v , while v_0 is the nozzle exit velocity. If the Weber number is sufficiently high such that surface tension can be neglected, and air-induced drag is considered negligible, then the jet velocity at impact takes the form,

$$\frac{v(z)}{v_0} = \left(1 + \frac{1}{F_r} \frac{z}{R_0}\right)^{1/2}, \quad (2.8)$$

where the Froude number $F_r = v_0^2/(d_0 g)$ represents the ratio of fluid inertial force to gravitational force. The radius is similarly given by,

$$\frac{R(z)}{R_0} = \left(1 + \frac{1}{F_r} \frac{z}{R_0}\right)^{-1/4}. \quad (2.9)$$

The derivation for velocity and radius evolution can be found in [16]. To consider the effects of gravity on jet impingement force, Eqs. (2.8) and (2.9) are substituted into the normalized form of Eq. (2.7) to yield,

$$\hat{F}_a(z) = \frac{\pi}{4} \left(1 + \frac{1}{F_r} \frac{z}{R_0}\right)^{\frac{1}{2}}, \quad (2.10)$$

where the subscript a , refers to the scenario depicted in Figure 2.1(a), as this jet exists in a gravitational field. If gravitational effects are weak (i.e., $F_r \rightarrow \infty$), then Eq. (2.10) reduces to the normalized form of Eq. (2.7). Equation (2.10) is perhaps a more realistic model as many industrial jets are influenced by gravity, however this equation does not account for free-surface perturbations.

2.3.2 Wavy jets

To determine the effect of waves on the jet impingement force, Rayleigh's description of the free surface given by Eq. (2.6) is employed. This implies that the radius of the impinging jet is time-periodic at any given fixed plate location, defined as $z = Z$. A control

volume analysis is used, similar to the steady-state jet, but now with a spatially varying control volume. The control volume is now the area of the jet bounded by the (time-dependent) free-surface and the base in contact with the plate revolved about the z axis. The flow is assumed uniform at the top boundary of the control volume and at the exit. Rayleigh's theory indicates that there exist axial and radial velocities associated with the capillary pinching of the jet. These velocities are, however, negligible compared to the bulk velocity. Therefore, at the top boundary, there exists uniform flow of velocity v , in the z direction, with a time-varying cross-sectional area. It is assumed that the top boundary is very close to the plate, permitting evaluation at the plate location, $z = Z$. Applying the integral momentum equation to this control volume yields,

$$\hat{F}_{wavy}(z, t) = \frac{\pi}{4} [1 + 2\epsilon e^{\beta z} \cos(\zeta - 2\pi f t)], \quad (2.11)$$

where $\zeta = Kz + \phi$ is a parameter to shift the phase as required, and $\epsilon = a/R_0 \ll 1$ is the normalized initial wave amplitude. As anticipated, Eq. (2.11) is oscillatory in time and fluctuates about the steady-state force given by Eq. (2.7). Note that the amplitude of oscillation increases exponentially in the z direction. If the impact surface exceeds the breakup length (i.e., $Z > L_b$), then this model would obviously not be applicable as droplets would impact the surface instead of a wavy jet. Due to the linearized small perturbation theory incorporated into Eq. (2.11), this model is anticipated to only work for small wave amplitudes. Although Eq. (2.11) exhibits z dependence, gravitational effects are not included.

In a similar way to the steady-state jet, gravity will increase the jet velocity according to Eq. (2.8), and reduce the time-invariant radius according to Eq. (2.9). With these considerations, the gravitational dependent form of Eq. (2.11) becomes,

$$\hat{F}_b(z, t) = \frac{\pi}{4} [1 + 2\epsilon e^{\beta z} \cos(\zeta - 2\pi f t)] \left(1 + \frac{1}{F_r} \frac{z}{R_0}\right)^{1/2}, \quad (2.12)$$

where the subscript b refers to the scenario depicted in Figure 2.1(b). If gravitational effects are deemed negligible (i.e., $F_r \rightarrow \infty$), then Eq. (2.12) reduces to Eq. (2.11). In addition, if the jet does not exhibit wavy oscillations about the free-surface (i.e., $\epsilon e^{\beta z} \rightarrow 0$), then Eq. (2.12) reduces to Eq. (2.10). It must be noted that, due to gravity, waves are stretched along the axial direction. Therefore, the wave number decreases with z , and thus waves take on a range of growth rates before impact. A comprehensive report on the consequences of jet elongation was presented by Frankel and Weihs [113]. The wave number incorporating gravitational dependence is given by,

$$k(z) = \frac{2\pi f}{v_0} \left(1 + \frac{1}{F_r} \frac{z}{R_0}\right)^{-1/2}. \quad (2.13)$$

Although the waves change wave number, the wave frequency remains constant, as required by mass conservation. Equation (2.12) indicates that the jet impingement force is oscillatory in time with frequency f , and it increases in the z direction. If the impact surface is positioned past the breakup length, then a series of droplet impacts will occur.

2.4 Force induced by droplets

The impact force of a single droplet has been experimentally investigated, modeled, and extensively discussed in Chapter 1. A salient feature of this work was the development of a force-model, which accurately predicts the force evolution for droplet impacts in the self-similar, inertial regime, i.e., $Re > 280$. This model equation is given below, but with different notation than in Eq. (1.8),

$$\tilde{F}_{drop}(\tilde{t}) = \sqrt{\frac{1000\pi\tilde{t}}{243}} e^{-10\tilde{t}/3}. \quad (2.14)$$

In this section the tilde denotes quantities normalized using the droplet diameter D , while a caret denotes quantities normalized using the initial jet diameter d_0 . Aside from force, another important aspect of characterizing a droplet impact is its impulse. The impulse is the area under a force-time profile, and physically indicates the amount of momentum exchanged during a collision. The area under the curve [Eq. (2.14)] is, by design, equal to the droplet momentum just before impact. This implies that the inertially dominated droplet impact is modeled by a perfectly inelastic collision. In this case, the impulse is expressed as,

$$\tilde{I}_{drop} = \int_0^{\infty} \tilde{F} d\tilde{t} = \frac{\pi}{6}. \quad (2.15)$$

As specified, the value $\pi/6$ is equal to the momentum of the drop mv (where m is the droplet mass) normalized by $\rho D^3 v$. Note that if the droplet rebounds from the surface with the same velocity but in the opposite direction, then the impulse will be twice that given

by Eq. (2.15). In this context, the droplet impact is perfectly elastic. Superhydrophobic surfaces allow droplets to rebound [114], and consequently, the force induced by this type of impact differs fundamentally from that given by Eq. (2.14). It is important to note that Eqs. (2.14) and (2.15) model droplets impinging and adhering onto solid dry surfaces. One may wonder if these expressions, which characterize a single droplet impact, may be extended to a continuous train of droplet impacts emanating from a liquid jet, like that depicted in Figure 2.1(c).

One important feature of droplet trains is the presence of a liquid film atop the impact surface. It is likely that after the first droplet impact, a film of liquid will pool about the impact location. Droplets impacting a deep pool ($L_p \gg D$, where L_p is the pool depth, see Figure 2.1(c)), that have sufficient speed, will create a Worthington jet [115]. In contrast, droplets impacting a shallow pool, $L_p < D$, typically splash with an upward-propagating crown [26, 76, 79], which often fragments into smaller droplets. The force induced by water droplets impacting various depths of water has been measured by Yu and Hopkins using an acoustic-based wavelet deconvolution method [43]. Their results show that the force associated with capillary waves and the ascending crown tend to be negligible compared to the force induced by the initial droplet impact. Qualitatively, the presence of a shallow pool increases the peak force and time to reach peak force, making the force profile more symmetric. In addition, the presence of a pool increases the observed impulse. This increased impulse indicates that the impact tends toward conditions in which the drop momentum is redirected upward. This is indeed the case for Worthington jets as liquid is sent upward after the drop coalesces with the deep pool. In general,

however, for $L_p \rightarrow 0$, the shallow pool force profile approaches the dry-surface force profile.

If the pool depth is very shallow and has negligible effects on the droplet force profile, then the force induced by a train of droplets can be modeled by a series of single droplet impacts via Eq. (2.14). If equal-sized droplets of diameter D are formed at the breakup length L_b , at a rate f , and one droplet is produced per wavelength, then the force induced by a series of droplet impacts is given by

$$\hat{F}_c(\hat{t}) = \sum_{n=1}^N \hat{F}_n(\hat{t}), \quad (2.16)$$

where the subscript c refers to the scenario depicted in Figure 2.1(c), the subscript n corresponds to the droplet number, N is the total number of droplets, and $\hat{F}_n = F_{drop}/\rho v_0^2 d_0^2$, but shifted in time by the amount $\hat{t}_n = v_0(n-1)/(d_0 f)$. Explicitly, \hat{F}_n is the droplet impact force normalized by the jet parameters and is written as,

$$\hat{F}_n(\hat{t}) = \left(\frac{v}{v_0}\right)^{5/2} \left(\frac{D}{d_0}\right)^{3/2} \sqrt{\frac{1000\pi\hat{t}}{243}} e^{-\frac{10vd_0\hat{t}}{3v_0D}}, \quad (2.17)$$

Where $D = (3\pi d^2/k)^{1/3}$ is the droplet diameter, with v , d , and k given by Eqs. (2.8), (2.9), and (2.13), respectively. This form ensures that mass conservation is satisfied assuming that one droplet is produced per wavelength. If indeed the impact is perfectly inelastic, then Eq. (2.16) also satisfies momentum conservation, as the axial momentum of a section of the jet (which has the volume of the drop), becomes the droplet momentum,

that is then transferred to the surface upon impact. Accordingly, the impulse of one droplet in the series is equal to the impulse of the continuous (or wavy) jet of equal volume. This is perhaps not surprising since in all three scenarios in Figure 2.1 the same momentum exits the nozzle, and thus by momentum conservation the same momentum must be exchanged with the surface. Figure 2.3 shows three cycles of the droplet train force profile given by Eq. (2.16), based on the Rayleigh mode, along with the steady-state force profile given by Eq. (2.7). Note that the impulse given by Eq. (2.15) is evaluated from $t = 0$ to $t \rightarrow \infty$, and thus in order for the droplet train impulse Eq. (2.16) to be exactly equal to the steady-state (or wavy jet) impulse, one must allow $t \rightarrow \infty$. This indicates that over one cycle, from t_n to t_{n+1} , the areas under each curve are only approximately equal. To highlight this, the impulses of each profile determined for the first cycle in Figure 2.3, from $\hat{t} = 0$ to $\hat{t} = v_0/(d_0f)$, differ by only 0.12%. Therefore, the impulses experienced by the two scenarios over one cycle are approximately equal. In light of this subtlety, momentum conservation requires the droplet train force profile and the steady-state force profile to exhibit the same impulse (as $\hat{t} \rightarrow \infty$). Due to the droplet train's discrete nature, there exists periods of approximately zero induced force. Therefore, in order to satisfy momentum conservation, there must be a greater peak force induced by the droplet train than the steady stream. This is apparent in Figure 2.3, where the peak force is greater by a factor of 3.85. Note that for decreasing wave number (i.e., longer wavelengths), droplets become larger and are spaced farther apart, resulting in higher peak forces. This may be appealing for industrial use, as in the water droplet machining process. However, in practice, longer wavelengths are difficult to achieve due to secondary swellings [108]. It is worth noting that a previous study has reported that the peak force induced by a droplet

is 3.5–4 times greater than that of the continuous stream counterpart [116]. In this study, the force induced by free-falling, dripping droplets was measured and compared to the theoretical impact force of a continuous jet, i.e., Eq. (2.7). The experiment conducted in [116] differs from the experiments presented in this chapter as direct force measurements of Rayleigh jets are conducted for each of the possible outcomes (i.e., a steady jet, a wavy jet, and a droplet train), and they are compared with novel force models, i.e., Eqs. (2.12), (2.16), and (2.17).

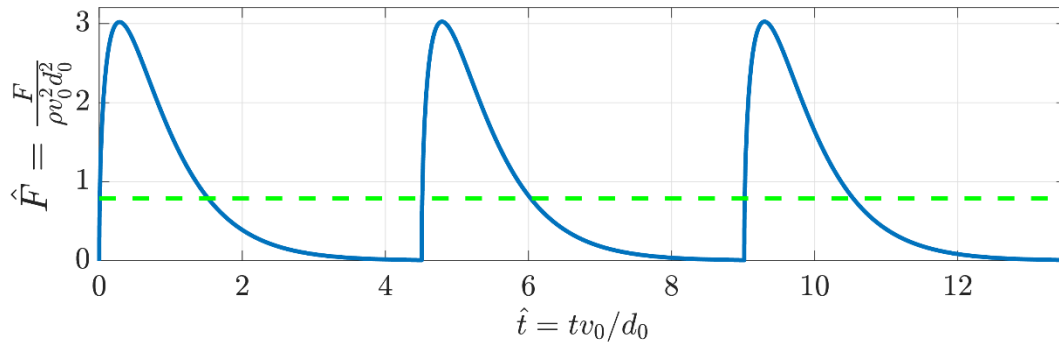


Figure 2.3: Force induced by a droplet train according to the Rayleigh mode (solid blue), and force induced by a steady-state jet (dashed green), shown for three cycles. The area under each profile (impulse) is approximately equal (i.e., both scenarios exchange the same cycle-averaged momentum with the surface). Due to its discrete nature, the droplet train experiences a greater peak force than the steady-state jet.

The jet and droplet acceleration due to gravity, via Eq. (2.8), is incorporated into Eqs. (2.10), (2.12), (2.16), and (2.17). This indicates that the velocities of the steady-state jet, the wavy jet, and the droplet train are equal upon impact, given that the nozzle to plate distance and nozzle exit conditions are equivalent. Similarly, Eqs. (2.10), (2.12), and (2.16) are all normalized with respect to the jet inertial parameters enabling direct comparison. The expressions characterizing the induced force of steady-state jets, wavy jets, and droplet trains demonstrate the roles of impulse, peak force, and momentum conservation. Many industrial applications (and natural phenomena) exhibit these types

of Rayleigh jet impacts, and thus the accuracy of the above models is of interest. Experimental comparisons with the given models are now provided.

2.5 Experimental setup and procedures

A precisely reamed aluminum nozzle with a diameter $d_n = 1.65$ mm and length $L_n = 0.38$ mm is used to form the Rayleigh jet. A 260 mm diameter reservoir supplies water to the nozzle through a 13 mm diameter hose; see Figure 2.4 for a schematic of the experimental setup. Once formed, the jet travels in the z direction and impacts a piezoelectric force sensor (PCB model 209C11), located a distance $Z = 106$ mm from the nozzle exit. The bottom of the force sensor is threaded to a large steel plate. On top of the sensor rests a 17.9 mm diameter polyoxymethylene plastic impact plate and it is the target for the impinging jet. Note that a 12.3 mm diameter aluminum impact plate is used for the wavy jet experiments. The excitation voltage necessary for the force sensor is supplied by a PCB model 482 signal conditioner. A Lecroy Wavesurfer 64MXs-B oscilloscope sampling at 100 kHz is used to acquire the force sensor response. A Photron SA4 Fastcam is used to take high-speed photographs of the impinging jets at a frame rate of 13,500 fps and with an exposure time of $74 \mu\text{s}$. The camera is positioned next to the force sensor revealing the last 15 mm of the jet before impact. Time is synchronized between the camera and force sensor through the oscilloscope. A 0.2 W audio speaker is placed perpendicular to the stream at the nozzle exit to provide wave-number stimulation (only used for the wavy jet and droplet train experiments). The orientation of the speaker perpendicular to the jet assures negligible momentum is added to the jet by the sound wave. A function generator provides the speaker with a sinusoidal stimulation frequency of 340 Hz and imposes a peak-to-peak voltage of 1.5 and 20 V for the wavy jet

and droplet train experiments, respectively. The imposed frequency corresponds to a wave number of $kR = 0.634$ at impact. This is close to the wave number of the Rayleigh mode (i.e., $kR = 0.697$); see Figure 2.2. The camera field of view is small relative to the length of the jet. This allows one to assume a constant wave number at the impingement zone of the wavy jet. With this field of view, approximately two wave crests are observed at any given time. By tracking the free surface, the wave growth rate β may be determined as well as the equivalent initial wave amplitude a . Once obtained, these parameters permit use of Eq. (2.12) to compare with experimental results. If one droplet is produced per wavelength, then the droplet diameter would be 2.7 mm. However, satellite droplets form in between primary drops, and thus the primary droplet diameter is smaller than this value. In general, it is difficult to precisely measure the droplet diameter as the droplet oscillates between an irregular prolate and oblate shape after pinch-off. The droplet impact velocity is approximately equal to the impact velocity of the steady state and wavy jet as indicated by high-speed images and position-tracking software.

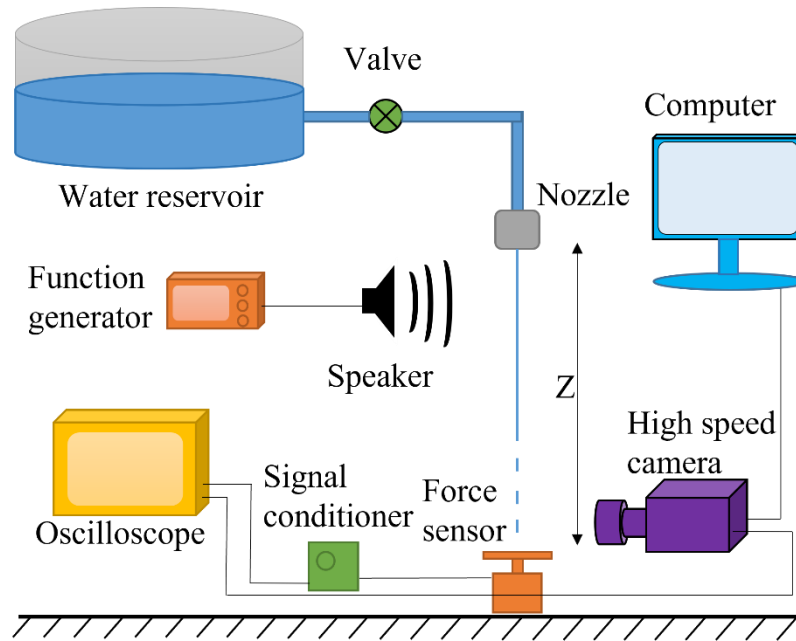


Figure 2.4: Schematic of the experimental setup. A Rayleigh jet is formed and impacts normal to a piezoelectric force sensor. A speaker stimulates the free surface to form a wavy jet/droplet train.

Nozzle exit velocity is controlled by the hydrostatic water level in the tank. Flow-rate measurements determine the nozzle exit velocity to be $v_0 = 1.84$ m/s. The velocity change due to reservoir drainage is negligible: after 60 s of continuous flow, the velocity decreases by about 1%, corresponding to a 2% decrease in induced force (i.e., force scales as v^2 in the inertial limit). The duration of one droplet impact or one wave impact occurs on a millisecond time scale. Therefore, the change in velocity during the experiment is much smaller than 1%, permitting a constant flow velocity assumption. According to images taken at the nozzle exit, the diameter of the jet contracts to $d_0 = 1.56$ mm, corresponding to a contraction ratio of $\chi = 95$ %. This decrease in jet diameter is consistent with the study of Gavis and Modan [110]. The density and viscosity of the water are $\rho = 998$ kg/m³ and $\mu = 1.0$ cP, respectively. The Reynolds and Weber numbers of the jet are $Re = \rho d_0 v_0 / \mu = 2860$ and $We = \rho d_0 v_0^2 / \sigma = 73$, respectively. These ratios identify the inertial force as dominant compared to viscous and surface tension forces.

With the ambient gas being stagnant air, this Weber number satisfies Eqs. (2.1) and (2.2), and therefore the jet is considered to be within the Rayleigh regime.

To mitigate transient effects associated with mechanically opening the nozzle supply valve, a sheet metal plate is positioned in front of the stream close to the force sensor while opening the valve. This diverts the stream from the sensor and allows the jet to reach steady state. After about 2 s, the shielding plate is quickly removed, allowing the jet to freely impinge the force sensor. In this process, a liquid globule at the fore of the jet always develops (see the Supplemental Material [16]). Although undesirable, the duration of the transient effect associated with the globule is much shorter than that of opening the valve.

2.6 Results and discussion

Images of the steady-state jet, the wavy jet, and the droplet train are shown in Figure 2.5, while the force induced by these impacts is shown in Figure 2.6 for a duration of 60 ms. The flow conditions exiting the nozzle in all three scenarios are identical, as is the nozzle to plate distance. The state of the jet upon impact is governed by the artificial stimulation induced by the audio speaker. The series of images displayed in Figure 2.5 reveal the jet evolution in 12 increments of $370 \mu\text{s}$ for the steady state and wavy jet, and eight increments of $593 \mu\text{s}$ for the droplet train. These durations correspond to slightly more than one time period. Notice that the steady-state jet, Figure 2.5(a), appears to be time-invariant as expected, while the wavy jet, Figure 2.5(b), exhibits a series of wave impacts. The droplet train, Figure 2.5(c), displays a series of droplet impacts. To correlate the time in which the impacts in Figure 2.5 occur with their corresponding force, green-shaded

regions are outlined in Figure 2.6. These regions allow the force to be directly compared with Figure 2.5. Supplemental movie files show how the force evolution compares with the images of the jets' impact [16].

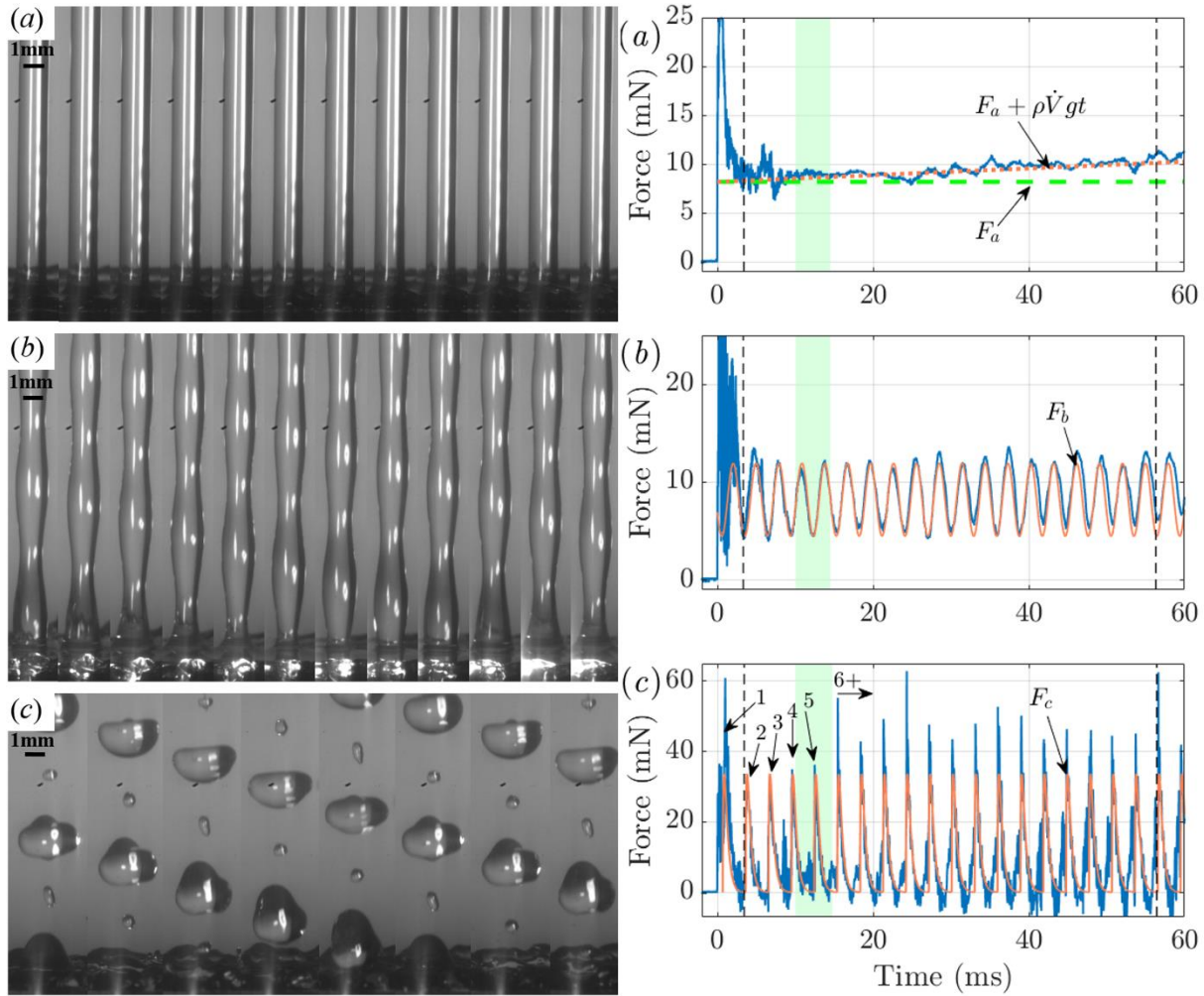


Figure 2.5 (left): High-speed images of the normal impingement of Rayleigh jets: (a) steady-state jet, (b) wavy jet, and (c) droplet train. The progression of images is from left to right in increments of $370 \mu\text{s}$ (a), (b) and $593 \mu\text{s}$ (c). The time in which these impacts occur corresponds to the shaded green regions in Figure 2.6.

Figure 2.6 (right): Force induced by Rayleigh jets: (a) steady-state jet, (b) wavy jet, and (c) droplet train. Arrows indicate model predictions (orange/green), e.g., F_a , F_b , and F_c from Eqs. (2.10), (2.12), and (2.16), respectively. The (dashed black) lines indicate integration bounds.

2.6.1 Steady state jet

Figure 2.6(a) shows the force induced by the steady-state jet. Here, the transient effect associated with the globule at the fore of the jet is apparent from 0 ms (initial impact) to about 3 ms. Here, a large increase in force is observed due to the sudden redirection of momentum from the axial to radial direction of the jet. Once the transient effect subsides, the force induced by the steady-state jet remains close to the inviscid prediction (dashed green line), while slight deviations exist presumably due to random oscillations of excess liquid on the plate. The steady-state force given by Eq. (2.10) is 8.2 mN and compares well with the experimental results immediately following the transient. As time increases, however, the force increases slightly due to mass accumulation on the force sensor. High-speed images reveal that the excess liquid adheres to the plate and does not flow off the edge. Therefore, to account for the additional weight on the force sensor, a mass accumulation term is included in Figure 2.6(a), represented by a dotted orange line. The additional weight is simply the accumulated liquid given by $\rho \dot{V} g t$, where \dot{V} is the jet flow rate. This modification to Eq. (2.10) follows the data trend.

2.6.2 Wavy jet

The force induced by the wavy jet is shown in Figure 2.6(b). As is apparent, the force oscillates in accordance with the sinusoidal free-surface radius at the fixed plate location. Physically, as the jet's cross-sectional area expands, the plate diverts more momentum, thus corresponding to a greater force. Equivalently, when the area contracts, less momentum is diverted by the plate driving the force toward its lower bound. The force amplitude is approximately 3.7 mN and fluctuates about the steady-state jet force. The average oscillation frequency of the peak-to-peak force is 340 Hz, corresponding to the

stimulation frequency. In contrast to the steady-state jet, the excess liquid in the wavy jet flows off of the impact plate due to the smaller diameter plate used. Therefore, the linearly dependent mass accumulation term used in Figure 2.6(a) is not required. To use Eq. (2.12) to compare with the experiments, the wave growth rate β and the equivalent initial wave amplitude a , must be determined.

High-speed images and edge detection software were used to record the free surface of the wavy jet. The free surface of the jet is measured at fixed z locations, from $t = 10$ to 30 ms, representing about six cycles. The axial locations range from $z = 91$ to 105 mm in 26 increments of about 0.55 mm. Recall that in the laboratory reference frame the wavy jet oscillation amplitude increases with axial distance. A linear regression performed on the observed amplitudes was used to estimate their growth rate and equivalent initial wave amplitude. Figure 2.7(a) shows the free surface at $t = 10$ ms, with an orange line, where two waves are observed. It is clearly noticeable that the amplitude of oscillation increases with the z direction. The time-averaged amplitude is recorded and plotted in Figure 2.7(b) with blue dots. The line of best fit, using linear least squares, is presented with a green line. This yields $\beta = 58.7 \text{ m}^{-1}$ and $a = 3.52 \times 10^{-7} \text{ m}$ for the model $\beta z + \ln a$. With these parameters, the time-averaged envelope is plotted in Figure 2.7(a) with a dashed blue line. Figure 2.7(c) shows the free-surface radius with respect to time for axial locations of $z = 91$ and 104 mm, respectively. Notice that the $z = 104$ mm location oscillates with a greater amplitude (by a factor of 2.01). This is due to the exponentially increasing free-surface radius along the z direction, as predicted by Rayleigh jet theory. The mean free-surface radius is 0.71 mm, which is also the radius obtained for the steady-state jet. These values fall within 3% of the predicted radius, see Eq. (A11) in [16]. The edge detection

software also allows us to measure the jet wavelength, which is $\lambda = 6.61$ mm. This value is within 4% of that expected through Eq. (2.13). In addition, the wave frequency may be measured by the frequency of the peak-to-peak free-surface amplitude at a fixed z distance. This method is in agreement with the artificially induced frequency. Note that the droplet impact frequency may also be measured in a similar manner.

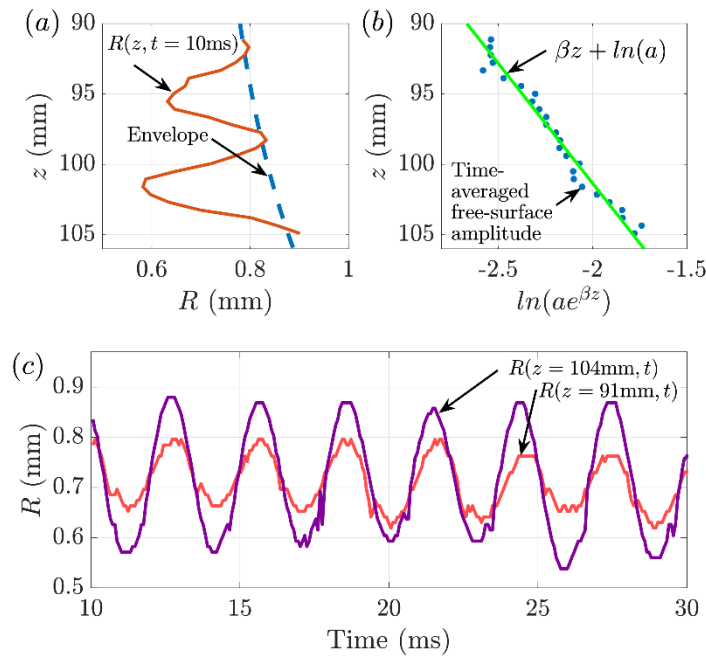


Figure 2.7: Wavy jet free-surface profile. (a) The free-surface along the axial direction z , at $t = 10$ ms (red line), with an envelope representing the time-averaged amplitude (dashed blue line). (b) The time-averaged amplitude of z locations near the plate (blue dot), with the line of best fit (green line). (c) The free-surface with respect to time at locations $z = 104$ mm (purple line) and $z = 91$ mm (red line).

The predicted oscillatory force, through Eq. (2.12), is plotted with an orange line in Figure 2.7(b). Equation (2.12) compares well with the measured force, containing the same frequency and approximately the same amplitude. Note that the phase in Eq. (2.12) is arbitrary, depending only on the time in which the analysis starts, thus the phase is chosen to coincide with the measurements, and it is set to $\zeta = 1.39\pi$. The wave amplitude at impingement is roughly 30 % of the jet radius, which is rather large. Despite the small

wave-amplitude assumption considered in deriving Eq. (2.12), there is good agreement with the theoretical prediction and the measurements. At $t = 0$ ms, the transient effect is apparent and occurs along a similar time duration to that for the steady-state jet. The droplet train does not exhibit the same transient effect as the continuous jets, rather two droplets at the fore of the train impact at similar times.

2.6.3 Droplet train

High-speed footage of the droplet train reveals that an irregularly shaped large droplet first impacts the plate away from the center (at roughly $r = 4$ mm; see the Supplemental Material in [16]). The first primary droplet and all subsequent droplets impact the force plate center. The first irregular droplet is the remnant of the transient effect associated with rapidly removing the shielding plate as previously described. In Figure 2.6(c), the primary droplet force profiles are labeled in sequence (i.e., 1, 2, 3, etc.).

Coincident with the irregular drop and the first primary drop, the force sensor shows a long period of induced force, from $t = 0$ to 3 ms, with two distinct peaks, the first being from the irregular drop and the second caused by the first primary drop. The ensuing four droplet impacts exhibit similar force characteristics to one another. These are labeled as 2–5 in Figure 2.6(c) and also in Figure 2.8, which is a magnified version of Figure 2.6(c). For each of these impacts, the force-time profiles exhibit a rapid increase in force, reaching a maximum of about 30 mN. This is followed by a longer fall-time to zero force. The total loading time for each droplet is about 3 ms. Comparatively, peak force is attained rapidly, just 200 μ s from initial impact. The characteristics of these four initial force profiles are similar to the profiles of individual droplet impacts onto dry surfaces [15]. The profiles

of these impacts are clearly shown in Figure 2.8(a), as well as the profiles of successive drops, shown in Figure 2.8(b). After the initial impacts (2–5), the successive force profiles (labeled as 6+) exhibit greater peak forces while becoming more symmetric about the time of peak force. This effect is attributed to the presence of a growing pool of excess liquid [43]. High-speed images show that most of the liquid from the droplet train remains on the plate, creating a pool about the impact location. The pool depth varies chaotically as droplets impinge, but in general the pool depth at the plate circumference is larger than at its center. Qualitatively, the presence of a pool increases the peak force and causes the force profile to become more symmetric about the time of peak force. These observations coincide with the study of Yu and Hopkins [43], where the authors measure the force of single droplets impinging a pool of water. It is therefore asserted that the force induced by droplet trains is influenced by shallow pools.

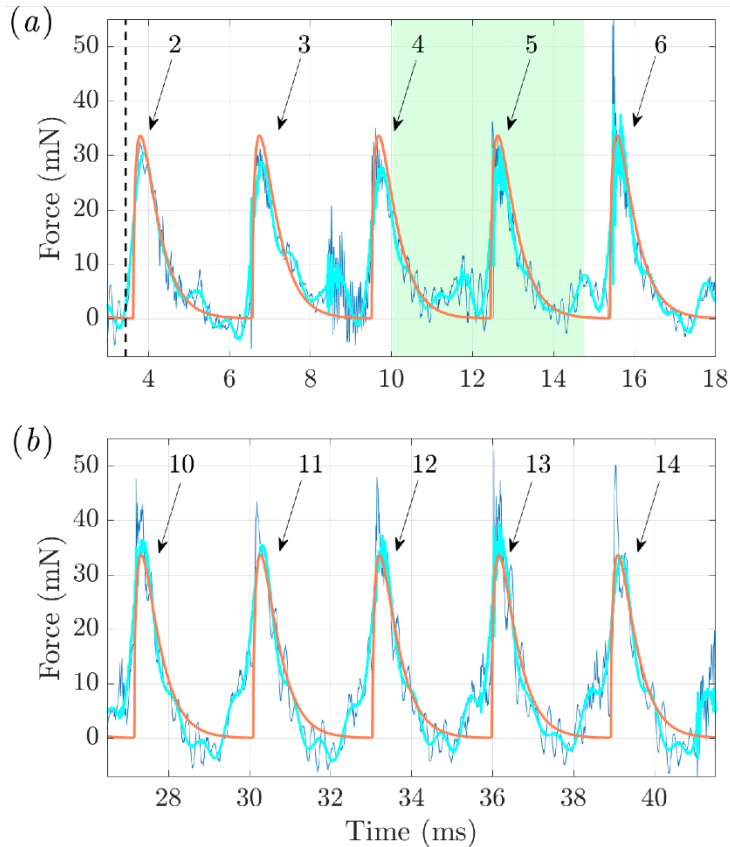


Figure 2.8: Force induced by the droplet train (blue-raw), and (cyan-filtered) for primary droplet impact numbers 2–6 (a) and 10–14 (b). The force predicted by Eq. (2.16) is shown in orange. For successive impacts (b), the presence of a liquid pool increases the peak force and alters the force profile toward symmetric conditions about the peak force.

The physical rationale for the increased peak force and the altered force profile (toward conditions of symmetry) due to the presence of a pool is that the water layer fundamentally changes the transmission of momentum from the droplet to the surface. In the case of a dry surface, all of the momentum mv , is transmitted to the surface; see Eq. (2.15). Due to the compliant nature of the water layer, a portion of the axial momentum is redirected upward. In this context, the impact behaves toward conditions of a perfectly elastic impact where all of the momentum is reflected. For such an idealized impact, the total impulse experienced by the surface would be $2mv$, and the force profile would be symmetric about the peak force. Due to the increased impulse (i.e., the area under force-

time curve), the peak force increases correspondingly - as long as the time durations are approximately equal. It is evident from Figure 2.8 that with successive impacts, the individual force profiles deviate from the dry-surface profile, given by Eq. (2.14). Therefore, the effects associated with the growing pool of liquid begin to invalidate the perfectly inelastic collision assumption incorporated in Eq. (2.16). Accordingly, as the pool depth grows, the force predicted by a series of individual droplet impacts, via Eq. (2.16), becomes less accurate.

The force predicted by Eq. (2.16) is plotted in Figs. 14(c) and 16 with an orange line. Due to the first irregular transitory drop, Eq. (2.16) is shifted in time by 0.7 ms to coincide with the measurements. It is apparent that Eq. (2.16) satisfactorily predicts the cyclic response of 340 Hz. However, the peak force of successive impacts (6+) is underestimated. Again, this is attributed to the pool, as the profiles of primary drops 2–5 compare reasonably well with Eq. (2.16), exhibiting a fast rise to maximum force followed by a progressively slower transition to zero. In all of the individual profiles, however, high-frequency oscillations exist.

Superimposed oscillations hamper the underlying response of the droplet train. This effect has been found in other droplet impact force studies [15, 21, 42, 43]. The oscillations are attributed to the resonant vibration of the force sensor system [41]. The undesired ringing can be mitigated by reducing the droplet impact velocity, or by spectrally filtering the response. In addition, for these experiments plates of low mass are used, which reduce the influence of superimposed oscillations [41]. The measured forces in Figures 2.6(a)–(c) are not filtered, revealing the sensor's direct response. The droplet train data

presented in Figure 2.8 are filtered with a low-pass filter attenuating frequencies above 2000 Hz (cyan line). The steady state and wavy jet exhibit oscillations as well, due to the suddenly applied load, but they diminish at about $t = 3$ ms; see Figures 2.6(a) and 2.6(b). Unlike the continuous jets, however, each droplet impact in Figures 2.6(c) and 2.8 appears to induce its own oscillations, therefore facilitating continuous ringing. Despite the ever-present oscillations, their amplitudes are small, roughly 15% of the peak force magnitude. Note that the pool of water randomly fluctuates and thus also introduces an additional, irregular force.

In contrast to the steady-state jet results, which show a linearly increasing force attributed to the accumulated liquid, the droplet train response does not appear to exhibit such a feature. One possible explanation for this is that the weight of the accumulating mass is insignificant compared to the large force induced by the droplets and their associated ringing. In addition to these abnormalities (compared to a single droplet impact onto a dry surface), the force dips below 0 mN, indicating that an upward force on the sensor is applied. According to high-speed images, after a droplet impinges, its liquid travels radially from the center colliding with the annular globule at the perimeter. It is suspected that capillary forces prevent the liquid from flowing off the plate edge, thus allowing liquid to accumulate and preventing further radial flow. Due to this restriction, a component of radial momentum is then directed upward only to yet again be bound by surface tension. Despite the greater peak forces experienced by successive droplet impacts, the negative force experienced by the ascending liquid renders a net momentum change of zero. Therefore, the impulse experienced by successive droplet impacts may be regarded as equivalent to primary drops.

In Figure 2.5(c) and in the Supplemental Material [16], the impingement of satellite droplets in-between primary droplets is clearly observed. The satellite drops are equally spaced in between primary drops and have a diameter of roughly 0.65 mm. With this diameter and equal impact velocity as primary drops (i.e., $v = 2.34$ m/s), the peak force of satellite drops, via Eq. (2.14), is 1.96 mN. This small level of force is hardly noticeable in Figures 2.6(c) and 2.8, especially among the ringing. Due to this, the force of satellite drops can be regarded as negligible compared to primary drops.

One additional artifact of the droplet train is that the droplets are not spherical upon impact. Indeed, the drops oscillate between an irregular prolate and oblate shape. Upon impact, the drops are slightly prolate. This indicates that the duration of momentum transmission from the drop to the surface is longer compared to a perfectly spherical drop. The consequences of this are a decrease in peak force and an increase in time duration. Although Eq. (2.16) suitably predicts the force induced by the initial droplets impacts, Figure 2.8(a) shows that the peak force falls slightly lower than that predicted by Eq. (2.16). Despite this, and the inconvenient ringing, Eq. (2.16) compares reasonably well with the measurements.

2.6.4 Impulse and momentum conservation

The jet momentum is assessed by integrating the force with respect to time (i.e., impulse). It is important that the domain of integration covers an integer number of cycles for the wavy jet and droplet train. In this way, the quadrature is representative of the total number of waves or drops that impact the surface. The force is integrated over 18 cycles for the wavy jet and droplet train. The dashed black lines in Figure 2.6, which represent the lower

and upper bounds of integration, are at $t = 3.5$ and 56.4 ms, respectively. The momentum of the steady-state jet is also assessed on the same domain. The measured impulse of the steady-state jet, the wavy jet, and the droplet train is $I_a = 5.00 \times 10^{-4}$ N s, $I_b = 4.70 \times 10^{-4}$ N s, and $I_c = 4.99 \times 10^{-4}$ N s, respectively. It appears that the impulse exerted by the steady-state jet and the droplet train are similar due to the accumulated mass on the sensor. In contrast, the wavy jet has a slightly smaller impulse. If the contribution from the mass accumulation term is subtracted from the steady-state jet impulse I_a , then the steady-state jet impulse is 4.46×10^{-4} N s. This value is close to the impulse of the wavy jet, differing by about 5%. In light of the subtleties surrounding the accumulated mass, it may be regarded that in all three scenarios the plate diverts the same n -cycle momentum. This should not be surprising as the same momentum exits the nozzle. Only the planar area of the liquid arriving at the plate differs between the scenarios. In this regard, the only inertial difference is the duration of momentum transmission from the liquid to the surface. This statement essentially outlines a tradeoff between a constant steady momentum flux (a) and discrete packets of momentum arriving in short bursts (c), with the momentum imparted by the wavy jet (b) being an intermediate scenario.

2.6.5 Steady-state jet versus droplet train

The normalized force induced by the steady-state jet (green line) and the droplet train (blue line) is shown in Figure 2.9. Here, the remarkable difference is with respect to the force signature. Despite the identical nozzle flow conditions and equal nozzle to plate distance, the peak force induced by the droplet train is significantly greater than the steady-state jet. Nevertheless, there exist periods of approximately zero induced force for the droplet train. For the first several primary droplets, before the pool affects the force

profile, the peak force is about three times greater. For the successive primary drops, the peak force is about five times greater than the steady-state jet. For industrial applications such as waterjet cutting or surface cleaning, it may be advantageous to use a droplet train in lieu of a steady-state jet due to the greater peak forces experienced by the impingement surface. Although there is a considerable difference in force between these two scenarios, their n -cycle momentum is approximately the same, as required by momentum conservation.

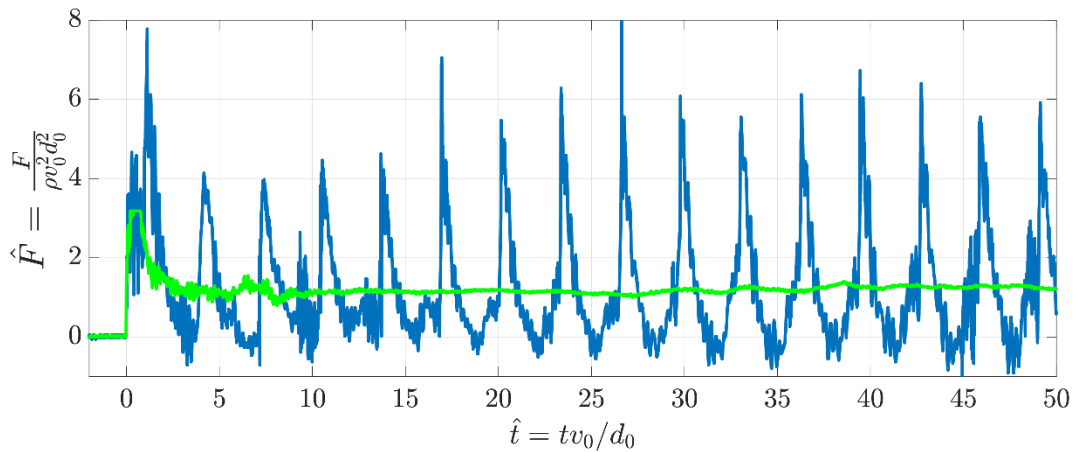


Figure 2.9: Normalized force of the steady-state jet (green) and droplet train (blue). Both jets have identical nozzle flow conditions, yet peak force induced by the droplet train is over three times greater. Both profiles exhibit approximately the same impulse, as required by momentum conservation.

2.7 Summary

The normal force induced by Rayleigh jets is measured with a high-sensitivity piezoelectric sensor. A high-speed camera records the jets' impingement and their free-surface profile. The force of these jets is measured for identical nozzle flow conditions and for equal nozzle to plate distance. Upon impingement with the surface, the state of the jet is categorized as either a steady-state jet, a wavy jet, or a droplet train. The wavy jet and droplet train are created by artificially stimulating the jet with an audio speaker

placed next to the nozzle exit. The prescribed frequency excites wave numbers associated with fast wave growth rates allowing wave amplitudes to be larger than if left to occur naturally.

An accurate force model for wavy jets, Eq. (2.12), is presented using the spatial form of Rayleigh jet theory. The level of agreement between the model and experimental results is excellent, validating the model's accuracy. In addition, a series of single droplet impact force profiles are combined to provide a model for the force of droplet trains. This model, which is based on momentum conservation, accurately captures the force induced by the initial primary droplets; however, as a liquid pool develops about the surface, the force changes fundamentally. The pool increases the peak force and delays the rise time, making the profile more symmetric.

Compared to the steady-state jet, the droplet train exerts a significantly greater peak force. However, due to its discrete nature, the droplet train also exhibits periods of approximately zero induced force. While its force varies periodically, its n -cycle momentum may be regarded as equivalent to the steady-state jet case, i.e., conservation of momentum. It may be more beneficial for industrial applications to use a train of droplets instead of continuous jets, due to the greater forces experienced by the impingement surface. The normal impingement of Rayleigh jets demonstrates the roles of inertia, impulse, and momentum conservation, while providing a fundamental platform for the examination of impact force.

3. ANALYSIS OF HERTZIAN CONTACT USING PHOTOELASTICITY

(The text and results in this section are in preparation for a paper titled “Determination of stress components for a Hertzian contact on a soft material using integrated photoelasticity.” This is ongoing work with Professor Yoshi Tagawa and Yuto Yokoyama, from the Tokyo University of Agriculture and Technology, and Professor Yannis Korkolis and Dr. Ali Nassiri from Ohio State University. My contributions to this work are theoretical models and numerical simulations, which are compared to experimental results conducted by the team in Japan.)

With a fundamental understanding of the force evolution of droplets impinging a solid surface (see Chapters 1 and 2), the next progression of research aims to understand the stress a material will experience when subjected to a droplet impact. As previously mentioned, the erosion mechanisms in the water droplet machining process are ill-understood; therefore, as a first step, this chapter aims to uncover the stresses in a material subject to quasi-static, axisymmetric “droplet-like” loading, i.e., a Hertzian contact. This provides the framework and methodologies for studying the dynamic droplet impact problem, which future work will investigate. This chapter analyzes a Hertzian contact problem of a static sphere pressed into an elastic material, and, through integrated photoelasticity, a method is developed to determine the maximum stress within the material. This aids in identifying the onset of material yielding.

The contact of a sphere with the flat surface of a homogeneous material presents a useful platform for analyzing the mechanics of Hertzian contact. The stress field within the material is of particular importance because it can be used to identify the contact zone

and the region where the onset of yielding occurs. The pioneering work of Huber (1904) showed that the point of maximum equivalent stress occurs inside the material, beneath the surface, and is the region where plastic deformation is initiated [117]. The magnitude of stress at this crucial point is highly sought-after since it can be used to predict yielding, and therefore, determine whether the material will experience permanent deformation. Analytical and numerical models have been used to calculate the stress inside a material subject to Hertzian sphere loading [118-122]; however, experimental methods are far less prevalent. This is due to the difficulty in measuring stress inside of a material subject to mechanical deformation. One tool that is particularly suited for this is photoelasticity.

Photoelasticity is a stress-analysis technique that correlates polarized light with principal stress difference. Measurements acquire the lights' change in phase, i.e., phase retardation (denoted δ), after it has passed through the photoelastic model. The technique has gained widespread adoption due its nondestructive nature, whole-field graphic capability, visual appeal, and relative ease of testing. It has shown success in measuring stress distributions in a variety of mechanical testing specimens, e.g., residual stress in glass, and the determination of stress concentration factors [123-129]. Despite these achievements, there are several restrictions to the method. A major limitation is that only materials which exhibit optical birefringent properties are suitable for photoelastic analysis. In addition, the technique has been primarily used for planar loading conditions, where a direct relationship between principal stress difference and the measured optical phase retardation is permitted [130, 131]. Circumstances where the stress state varies along the light propagation direction do not admit trivial solutions. This is due to the complex propagation qualities of light passing through optically anisotropic media, which

render the governing equations non-linear and make the problem ill-posed [132-135]. Despite these constraints, there has been success in analyzing 3-dimensional stress states using the approximation of geometrical optics in integrated photoelasticity [136-138]. However, this approximation places limitations on the degree of phase retardation that the photoelastic model can support, and in particular, is only applicable to situations where birefringence is weak [136]. Nevertheless, integrated photoelasticity can be a good tool for analyzing the stress in 3-dimensional Hertzian contact problems.

The aim of this study is to analyze the sub-surface stress in the Hertzian contact problem of a sphere pressed into an elastic material using integrated photoelasticity. Through this, information can be gathered about the contact zone and the maximum equivalent stress can be quantified. Photoelastic experiments are conducted and are compared with the theoretical phase retardation fields calculated using Hertzian contact theory. This comparison allows for verification of the integrated photoelasticity model and is also used to determine its limitations. Furthermore, the substrate used in the experiments is a highly deformable soft solid, gelatin, which has numerous uses in the medical, soft robotics, pharmaceutical, and culinary fields. Analysis of this material subject to Hertzian contact through photoelasticity is an innovation on this classical mechanics problem and is important because it serves as a tool for nondestructive stress measurement, while providing verification of the approximation of geometrical optics and Hertzian contact models applied to soft solids. The results and methodologies used in this study establish a framework for analyzing axisymmetric loading conditions on soft materials, and therefore, serve as a benchmark for future studies, such as the impact of a droplet.

This chapter is organized as follows. Section 3.1 describes the experimental methods, while section 3.2 describes integrated photoelasticity in terms of the optically equivalent model. Section 3.3 derives the theoretical stresses expected in the Hertzian loading scenario. These stresses are used in the optically equivalent model to obtain theoretical phase retardation fields, which can be directly compared to the experiments. In addition to theoretical stresses, numerical determination of stresses induced in the Hertzian contact problem are simulated using Abaqus. This is described in section 3.4 where simulations are used in conjunction with the integrated photoelasticity model to compare with theory and experiments. Section 3.5 discusses the results and demonstrates the ability to determine equivalent stress and each principal stress component at the point of highest stress, given only the phase difference field obtained from integrated photoelasticity. Section 3.6 summarizes the findings and provides recommendations for future studies. Future research will study the ability to measure equivalent stress and principal stress components for dynamic water droplet impact on gelatin media. This will help to understand further the erosion mechanisms observed during WDM.

3.1 Experimental methodologies

To probe the stress state inside of a material subject to a Hertzian contact, an experiment is devised using integrated photoelasticity. A schematic of the setup is shown in Figure 3.1(a) where a 15 mm diameter styrol sphere is placed on the top surface of a 44 x 44 x 47 mm³ gelatin cuboid. This produces a Hertzian contact scenario in the vicinity of the sphere and within the gelatin. Polarized light is incident upon the front surface of the cuboid, and as it propagates through the material, it accumulates phase retardations corresponding to the state of stress along the light ray. The light then emerges from the

back side of the cuboid and is acquired for analysis. An (x, y, z) Cartesian coordinate system is chosen for the cuboid where the y -direction coincides with the light propagation direction, while the z -direction coincides with the loading axis of the sphere, which is the vertical direction. The x -direction is transverse to the light rays and is the horizontal direction. Since the Hertzian loading condition entails axial symmetry, a cylindrical coordinate system, i.e., (r, θ, z) , is superimposed onto the Cartesian system. The radial direction coincides with the x -direction when $\theta = 0$ and coincides with the y -direction when $\theta = \pi/2$. The r - z plane of the cylindrical coordinate system is shown in Figure 3.1(b), where axial symmetry is assumed. The use of this coordinate system will be further elaborated in section 3.3.

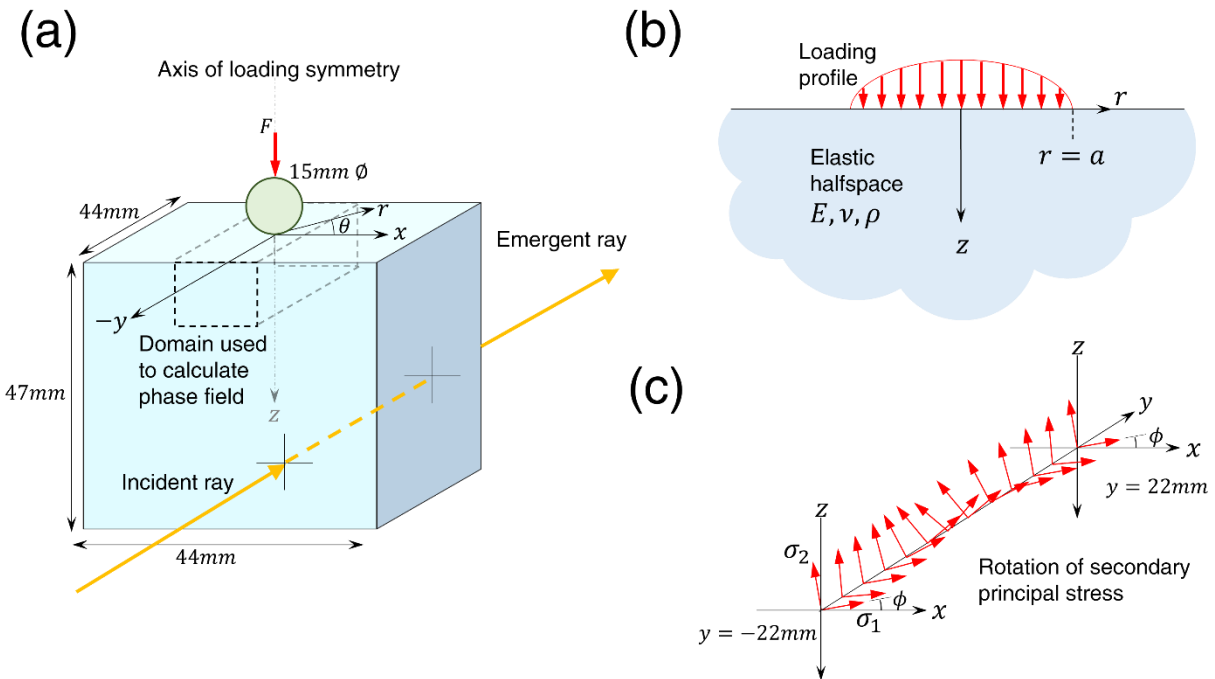


Figure 3.1: (a) Schematic of gelatin cuboid subject to axisymmetric Hertzian contact at center of top surface. Circular polarized light is incident upon the front surface of the cuboid ($y = -22$ mm), with emergent light exiting the back side of the cuboid ($y = 22$ mm), carrying with it accumulated stress-induced phase retardation δ . (b) Diagram of axisymmetric Hertzian loading configuration on top surface of an elastic half-space. (c) Illustration of secondary principal stress rotation along a given light ray.

3.1.1 Material properties

The gelatin was created by mixing gelatin powder from porcine skin (Sigma Aldrich G6144-1KG) with hot water (90°C) at a concentration of 5% weight. The solution was stirred until the temperature reached 30 °C, then the mixture was poured into an acrylic container with inside dimensions of 44 x 44 x 47 mm³ (container not shown in Figure 3.1(a)). The material was then placed in a refrigerator at 4 °C to allow solidification. Before conducting the experiments, the material was taken out of the refrigerator and given 2 hours to reach room temperature (20°C). The gelatin was kept in the container throughout the duration of experiments. The container contacts with the bottom and sides of the gelatin, and the boundary conditions that these impose, will be elaborated in section 3.3.

The elastic modulus of the gelatin was determined using the surface deformation technique [139, 140]. Here, a sphere is placed on the center of the gelatin with force F , and a camera is used to determine the maximum surface displacement induced by the sphere. This occurs directly underneath the sphere along the z-axis and is done for a range of applied forces. The relationship between maximum surface displacement and the force the sphere applies to the gelatin is given by:

$$u_z^{max} = \left(\frac{9F^2}{8DE^*2} \right)^{1/3}, \quad (3.1)$$

where D is the diameter of the sphere, and E^* is the effective modulus of the material [122, 141]. The effective modulus is given by:

$$E^* = \frac{E}{1 - \nu^2}, \quad (3.2)$$

where ν is the Poisson ratio [122, 141]. Due to the soft and nearly incompressible properties of gelatin at small strains, its Poisson ratio is approximately $\nu = 0.49$ [139, 142, 143]. It is assumed that the gelatin used in this study also features the same Poisson ratio value. Using Eqs. (3.1) and (3.2), along with the experimentally determined maximum displacements, the elastic modulus is calculated to be 4.22 kPa. This elastic modulus has reasonable agreement with other established moduli of gelatin [142-144]. The density of gelatin at 5% wt. is 1010 kg/m³ [145]. The stress-optic coefficient of the gelatin cuboid, which is a material property, has been determined to be $c = 3.3\text{E-}08 \text{ Pa}^{-1}$ by fitting the maximum theoretical to maximum experimental phase retardation. This value is in good agreement with previously established values for gelatin [124, 146]. The material properties and experimental parameters used in the study are presented in Table 3.

Table 3: Material properties and experimental parameters

Youngs modulus	E	4.22 kPa
Poisson's ratio	ν	0.49
Density	ρ	1010 kg/m ³
Stress-optic coeff.	c	3.3e-08 Pa ⁻¹
Wavelength	λ	540 nm
Sphere radius	R	7.5 mm
Sphere mass (effective)	$m = F/g$	1, 2, 3, 4, 5, 6, 7, 8, 9, 10, 12, 14, 16, 18, 20, 22, 24, 26, 28 & 30 grams

3.1.2 Experimental setup

Figure 3.2 shows an image of the experimental setup. The gelatin cuboid and acrylic container rest on top of a digital scale, which is used to measure the force applied to the

top of the sphere. The applied force F is related to the effective sphere mass m , by $F = mg$, where $g = 9.81\text{m/s}^2$. This is done to study the relationship between applied force and optical phase retardation. Under a planar load assumption, a purely elastic material will exhibit a linear relationship between applied force and phase retardation. For the Hertzian contact scenario, however, this is not the case, as a non-linear relationship between applied force and phase retardation is observed.

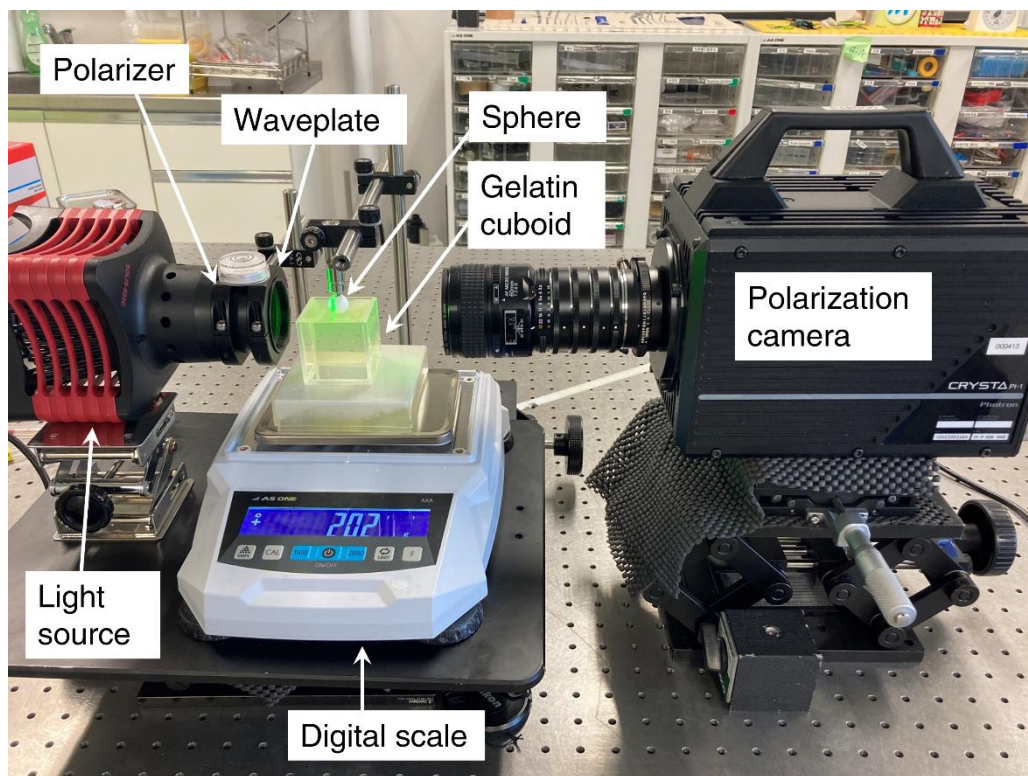


Figure 3.2: Image of experimental setup (courtesy of Yuto Yokoyama). A green light laser (520nm) is used to create coherent light, which first passes through a collimating lens, then through a linear polarizer (0°) and quarter waveplate (45°) to create left-handed circular polarized light. The light is incident upon the gelatin cuboid and emerges with an accumulated phase retardation Δ and rotation ψ and is then recorded by a Photron Crysta PI-1 high-speed polarization camera.

The gelatin cuboid is positioned in a polariscope with the following optical elements. A Thorlabs SOLIS-525C provides a coherent monochromatic light source of wavelength $\lambda = 540\text{ nm}$, which first passes through a plane polarizer whose transmission axis is

horizontal and aligned with the x-direction. The light then passes through a quarter-wave plate positioned with its fast axis at +45 degrees with respect to the x-axis. This creates left-handed, circular polarized light, which is then incident upon the gelatin cuboid. As the light propagates through the material, it accumulates phase retardations and rotations corresponding to the stress state along the given light ray. It is assumed that the clear acrylic plates on either end of the gelatin do not alter the phase nor orientation of the polarized light. Finally, the light emerges from the model as elliptically polarized light and is recorded by a Photron Crysta polarization camera, which features an array of “super-pixels.” Each super-pixel is discretized into four quadrants, which measures the polarization state at orientations of 0, 45, 90, and 135 degrees with respect to the x-axis. The four polarizer orientations enable the linear Stokes parameters to be identified (see Section 3.2.2), from which the degree and angle of linear polarization can be determined. The recorded light intensity fields are then post-processed using MATLAB to obtain phase retardation fields.

3.2 Integrated photoelasticity

While the experiments directly provide phase retardation fields, a method that converts phase retardation into stress tensor information is not available for the general case. This is known as the inverse problem of 3D photoelasticity, which is the reconstruction of the 3D stress distribution along the light path given only knowledge of the light vector before and after it has passed through the specimen [135, 147, 148]. The problem is nontrivial because of the complicated optical phenomena in a 3D, inhomogeneously-stressed photoelastic model. A comparatively simple relationship between measurement data and integrals of the stress components are only valid in circumstances where birefringence is

weak, or in cases where the principal stress orientation does not rotate along the light path [132-136]. Figure 3.1(c) depicts the phenomenon whereby the secondary principal stress orientation (see section 3.3.2) varies along the light path. This causes nonlinearity and complexity in the governing equations and is one of the primary concerns in integrated photoelasticity [149-151]. In the absence of secondary principal stress rotation, a relatively simple equation relating phase retardation and secondary principal stress difference is realized. As discussed in section 3.2, the phase retardation is proportional to the principal stress difference. However, in Hertzian contact problem, that difference varies continuously along each light path, see Figure 3.1(c). As a result of that, the emerging ray carries a cumulative phase retardation, which is what requires the use of integrated photoelasticity in this work.

3.2.1 Integral Wertheim law

In cases where the stress state varies along the light ray but where rotation of secondary principal stress is absent, or where birefringence is weak, the governing equations provide a relatively simple correlation between measurement data, i.e., phase retardation, and secondary principal stress difference [136-138]. This is given by,

$$\delta = c \int_a^b (\sigma_1 - \sigma_2) dy, \quad (3.3)$$

where δ is the phase retardation, σ_1 and σ_2 are the secondary principal stresses, which are the principal stresses in the plane orthogonal to the light propagation direction, and are, in general, functions of y . Since the light travels in the y -direction, this is the variable of integration, and its bounds are from where the light is incident upon the model, i.e., $y =$

a , to where it is emergent from the model, i.e., $y = b$. If the secondary principal stresses are constant along y , then Eq. (3.3) is reduced to the classic planar photoelasticity equation,

$$\delta = c(\sigma_1 - \sigma_2)t, \quad (3.4)$$

where t is the thickness of the model, i.e., distance through which the light travels in the photoelastic model.

Although the integral Wertheim law, i.e., Eq. (3.3), provides a relatively simple equation, it still does not directly yield the principal stress difference due to the presence of the integral. Hence, knowledge of the stress variation along y is needed in addition to measurement data in order to solve the inverse problem. For the Hertzian contact problem presented in Figure 3.1, the only region, where the principal stress orientation is constant along the y -direction, is on the $x = 0$ plane. Here, the secondary principal stress orientations coincide with the x and z directions. Therefore, the integral Wertheim law is valid only for light rays traveling along this plane. The application and validity of using Eq. (3.3) and (3.4) in the Hertzian contact scenario will be discussed in section 3.5. For the general case where rotation of secondary principal stress exists, a more elegant formalism is required.

3.2.2 Stokes parameters and the optically equivalent model

Due to the complexity involved with the inverse problem of integrated photoelasticity, determination of the stress state at arbitrary points along the light ray are not obtainable given the measurement data. Therefore, the aim of the present study is to compare

measurement data, i.e., phase retardation, with theoretically derived phase retardation of the Hertzian contact problem. Agreement between the experiments and theory will then allow for the theory to be used in determination of stress states. This will also verify the assumptions used in the theoretical models, specifically the premise of small strains and linearly elastic behavior.

To predict the phase retardation field in the Hertzian contact problem, an integrated photoelasticity model is needed, one which allows for rotation of secondary principal stresses. The optically equivalent model is one method that is particularly suited for handling 3D photoelastic specimens where rotation is present [152]. In this model, the specimen is discretized along the light propagation direction into a series of photoelastic plates. Each plate acts as either a linear retarder, linear rotator, or a combination of both. This effectively induces a small retardation and/or rotation to the light vector as it passes through each plate. The term “optically equivalent model” indicates that the series of discretized plates affects the light vector in the same way as the full specimen does, but with the added benefit of simplifying the analysis to an array of linear polarizing elements. To keep track of the polarization state as the light passes through each element, the Stokes parameters are employed.

The Stokes parameters are a set of values which describe the polarization state of light, and are written as a vector given by,

$$S = \begin{bmatrix} S_0 \\ S_1 \\ S_2 \\ S_3 \end{bmatrix}, \quad (3.5)$$

where S_0 is related to the total light intensity, S_1 is related to the intensity of light polarized in the 0° and 90° directions, S_2 is related to the intensity of light polarized in the 45° and 135° directions, and S_3 is related to the intensity of light that is circularly polarized. Three of these parameters are independent and are related through the following identity,

$$S_0^2 = S_1^2 + S_2^2 + S_3^2. \quad (3.6)$$

For the present analysis, the Stokes vector of the unpolarized light emitted from the laser source is given by,

$$S = \begin{bmatrix} 1 \\ 0 \\ 0 \\ 0 \end{bmatrix}. \quad (3.7)$$

As the light passes through the polarizing elements and each plate of the optically equivalent model, the Stokes vector will change. A convenient way of accounting for this change is through Mueller calculus [153]. The effect of each polarizing element can be represented by a Mueller matrix which, through Mueller calculus, is used to determine the Stokes vector of the light emergent from the polariscope. This can then be used to determine the theoretical phase retardation induced by the optically equivalent model.

The Mueller matrices of each of the polarizing elements in the polariscope are listed as follows. The Mueller matrix of the linear polarizer oriented at 0° is given by,

$$P_0 = \frac{1}{2} \begin{bmatrix} 1 & 1 & 0 & 0 \\ 1 & 1 & 0 & 0 \\ 0 & 0 & 0 & 0 \\ 0 & 0 & 0 & 0 \end{bmatrix}, \quad (3.8)$$

while the Mueller matrix of the quarter-wave plate oriented at 45° is given by,

$$Q_{45} = \begin{bmatrix} 1 & 0 & 0 & 0 \\ 0 & 0 & 0 & -1 \\ 0 & 0 & 1 & 0 \\ 0 & 1 & 0 & 0 \end{bmatrix}. \quad (3.9)$$

For each of the i^{th} plates in the optically equivalent model, the Mueller matrix is given by,

$$X_{\Delta,\psi}^i = \begin{bmatrix} 1 & 0 & 0 & 0 \\ 0 & 1 - (1 - \cos \Delta) \sin^2 2\psi & (1 - \cos \Delta) \sin 2\psi \cos 2\psi & -\sin \Delta \sin 2\psi \\ 0 & (1 - \cos \Delta) \sin 2\psi \cos 2\psi & 1 - (1 - \cos \Delta) \cos^2 2\psi & \sin \Delta \cos 2\psi \\ 0 & \sin \Delta \sin 2\psi & -\sin \Delta \cos 2\psi & \cos \Delta \end{bmatrix}, \quad (3.10)$$

where Δ is the phase retardation in radians, and is related to the phase retardation in meters δ by,

$$\Delta = \frac{2\pi}{\lambda} \delta. \quad (3.11)$$

The variable ψ is the principal angle, measured with respect to the x-axis, which specifies the orientation of the light ellipse, see Figure 3.1(c). For each plate in the optically equivalent model the phase retardation is calculated using Eq. (3.4), with thickness $t^i = 0.1$ mm being the distance in-between each of the equally thin plates. It is assumed that the orientation of the light ellipse ψ , coincides with the orientation of secondary principal stress ϕ . The Mueller matrix for the analyzer with orientations of $\theta = 0^\circ, 45^\circ, 90^\circ$, and 135° , with respect to the x-axis, is given by,

$$A_\theta = \frac{1}{2} \begin{bmatrix} 1 & \cos 2\theta & \sin 2\theta & 0 \\ \cos 2\theta & \cos^2 2\theta & \sin 2\theta \cos 2\theta & 0 \\ \sin 2\theta & \sin 2\theta \cos 2\theta & \sin^2 2\theta & 0 \\ 0 & 0 & 0 & 0 \end{bmatrix}, \quad (3.12)$$

After the light passes the analyzer, the output Stokes vector is given by,

$$S' = \begin{bmatrix} S'_0 \\ S'_1 \\ S'_2 \\ S'_3 \end{bmatrix}. \quad (3.13)$$

The output Stokes vector is determined using Mueller calculus by multiplying the Mueller matrices of the complete optical system used in the present study as,

$$S' = A_\theta X_{\Delta,\psi}^N \dots X_{\Delta,\psi}^i \dots X_{\Delta,\psi}^2 X_{\Delta,\psi}^1 Q_{45} P_0 S, \quad (3.14)$$

where N is the total number of plates in the optically equivalent model. By applying the phase shifting method, where the analyzer is rotated through the orientations of $\theta = 0^\circ$,

45°, 90°, and 135°, four distinct output Stokes vectors are obtained [154, 155]. The output intensity, i.e., S'_0 , of each of these Stokes vectors are denoted by I_1 , I_2 , I_3 , and I_4 , respectively, and are related by,

$$I_0 = \frac{I_1 + I_2 + I_3 + I_4}{2}. \quad (3.15)$$

After applying the phase shifting method to obtain the four Stokes vectors, and the corresponding light intensities, the phase retardation induced by the optically equivalent model is calculated as follows,

$$\Delta = \sin^{-1} \frac{\sqrt{(I_3 - I_1)^2 + (I_2 - I_4)^2}}{I_0}, \quad (3.16)$$

while the output principal orientation of the light ellipse induced by the optically equivalent model is given by,

$$\psi = \frac{1}{2} \tan^{-1} \frac{(I_3 - I_1)}{(I_2 - I_4)}. \quad (3.17)$$

Therefore, if given the secondary principal stresses and orientation at each of the i^{th} plates and applying the phase shifting method, the phase retardation can be determined for the optically equivalent model. This provides a theoretical expectation for the results obtained in an integrated photoelasticity experiment. In order to obtain the theoretical phase retardation in the Hertzian contact problem, the stress field is required.

3.3 Hertzian contact theory

To determine the stress state in a material subject to Hertzian contact, where a sphere of diameter D is pressed into the top of a flat surface with force F , a theoretical model is derived. In this model, the sphere is rigid while the substrate material bears all deformation. In the present experiment, the sphere is made of styrol, which has an elastic modulus of approximately 2 GPa. Therefore, the sphere is approximately rigid with respect to the gelatin, i.e., 2 GPa \gg 3.0 kPa. The theoretical analysis is greatly simplified if axial symmetry is assumed, along with allowing the substrate material to extend to a semi-infinite domain, see Figure 3.1(b). This analysis also assumes that the material is linearly elastic and that the small strain approximation is valid, despite the large displacements expected with such a soft material like gelatin. The contact between the sphere and substrate is assumed to be frictionless; therefore, only a normal pressure is transmitted by the sphere to the substrate. The validity of these assumptions will be evaluated in section 3.3.3.

3.3.1 Derivation

Consider an elastic half-space in cylindrical coordinates, which extends from $0 \leq z < \infty$, and $0 \leq r < \infty$, of Young's modulus, $E = 3.0$ kPa, and Poisson ratio, $\nu = 0.49$. The half-space is subject to a Hertzian pressure distribution on the $z = 0$ plane, along $0 \leq r \leq a$, where $r = a$ is the contact radius, see Figure 3.1(b). The normal pressure distribution corresponding to a sphere loaded along the epicentral z axis, with force F , and radius $R = D/2$, is given by [122],

$$\sigma_{zz}(r, z = 0) = p_0 \sqrt{a^2 - r^2}, \quad \text{for } 0 \leq r \leq a, \quad (3.18a)$$

$$\sigma_{zz}(r, z = 0) = 0, \quad \text{for } r > a, \quad (3.18b)$$

where,

$$p_0 = \frac{3F}{2\pi a^2}, \quad (3.19)$$

is the maximum pressure [122]. The contact radius is given by,

$$a = \left(\frac{3FR}{4E^*} \right)^{1/3}. \quad (3.20)$$

The radial, circumferential, axial, and shear stress components, which define the stress tensor in the axisymmetric half-space, are designated by σ_{rr} , $\sigma_{\theta\theta}$, σ_{zz} and σ_{rz} , respectively. Since frictionless contact is assumed, all other stress components on the surface are zero, i.e., $\sigma_{rr} = \sigma_{\theta\theta} = \sigma_{rz} = 0$ on $z = 0$. The sphere contacts the surface of the half-space with a constant force F ; therefore, static equilibrium equations are employed and are written as follows,

$$\frac{\partial \sigma_{rr}}{\partial r} + \frac{\sigma_{rr} - \sigma_{\theta\theta}}{r} + \frac{\partial \sigma_{rz}}{\partial z} = 0, \quad (3.21)$$

$$\frac{\partial \sigma_{rz}}{\partial r} + \frac{\sigma_{rz}}{r} + \frac{\partial \sigma_{zz}}{\partial z} = 0. \quad (3.22)$$

Notice that body forces are absent from Eq. (3.21) and (3.22). This is done to promote a more straightforward analysis. The stresses induced by gravity will be added at the end using the principal of stress superposition. Gravity induces a hydrostatic stress to the material, which does not alter the secondary principal stress difference. Therefore, gravity does not affect the phase retardation in the photoelastic measurements.

In order to ensure a physically meaningful displacement field, the stress compatibility relations are utilized and are given by,

$$\nabla^2 \sigma_{rr} - \frac{2}{r^2} (\sigma_{rr} - \sigma_{\theta\theta}) + \frac{1}{1+\nu} \frac{\partial^2 e}{\partial r^2} = 0, \quad (3.23)$$

$$\nabla^2 \sigma_{\theta\theta} - \frac{2}{r^2} (\sigma_{rr} - \sigma_{\theta\theta}) + \frac{1}{1+\nu} \frac{1}{r} \frac{\partial e}{\partial r} = 0, \quad (3.24)$$

$$\nabla^2 \sigma_{zz} + \frac{1}{1+\nu} \frac{\partial^2 e}{\partial r^2} = 0, \quad (3.25)$$

$$\nabla^2 \sigma_{rz} - \frac{\sigma_{rz}}{r^2} + \frac{1}{1+\nu} \frac{\partial^2 e}{\partial r \partial z} = 0, \quad (3.26)$$

where the Laplacian is given by,

$$\nabla^2 = \frac{\partial^2}{\partial r^2} + \frac{1}{r} \frac{\partial}{\partial r} + \frac{\partial^2}{\partial z^2} = 0, \quad (3.27)$$

and where $e = tr(\bar{\sigma}) = \sigma_{rr} + \sigma_{\theta\theta} + \sigma_{zz}$. Love (1929) derived a biharmonic stress function $\xi = \xi(r, z)$, which identically satisfies the equilibrium equations, as well as the compatibility relations [156]. The stress components (in cylindrical coordinates) can be derived from the Love stress function as follows,

$$\sigma_{rr} = \frac{\partial}{\partial z} \left(\nu \nabla^2 \xi - \frac{\partial^2 \xi}{\partial r^2} \right), \quad (3.28)$$

$$\sigma_{\theta\theta} = \frac{\partial}{\partial z} \left(\nu \nabla^2 \xi - \frac{1}{r} \frac{\partial^2 \xi}{\partial r} \right), \quad (3.29)$$

$$\sigma_{zz} = \frac{\partial}{\partial z} \left((2 - \nu) \nabla^2 \xi - \frac{\partial^2 \xi}{\partial z^2} \right), \quad (3.30)$$

$$\sigma_{rz} = \frac{\partial}{\partial r} \left((1 - \nu) \nabla^2 \xi - \frac{\partial^2 \xi}{\partial z^2} \right). \quad (3.31)$$

Similarly, the radial and axial displacements in the half-space can be determined using the Love stress function and are given by,

$$u_r = -\frac{1 + \nu}{E} \frac{\partial^2 \xi}{\partial r \partial z}, \quad (3.32)$$

$$u_z = \frac{1 + \nu}{E} \left(2(1 - \nu) \nabla^2 \xi - \frac{\partial^2 \xi}{\partial z^2} \right), \quad (3.33)$$

respectively. To determine the Love stress function the biharmonic equation is solved, which is given by,

$$\nabla^4 \xi = \nabla^2 \nabla^2 \xi = 0. \quad (3.34)$$

The Hankel transform method, explained by Ike [157], is used to solve this equation while enforcing the boundary conditions given by Eq. (3.18). The resulting Love stress function for the Hertzian contact problem is then,

$$\xi(r, z) = \int_0^\infty f(k) \left[\left(\frac{2\nu}{k} + z \right) \frac{J_0(kr)}{k^2} \right] e^{-kz} dk, \quad (3.35)$$

with

$$f(k) = p_0 \frac{(\sin ak - ak \cos ak)}{ak^2}, \quad (3.36)$$

where J_0 and J_1 specifies the Bessel function of first kind of order one and order two, respectively, and p_0 and a are given by Eqs. (3.19) and (3.20), respectively. The dummy variable of integration “ k ” is termed the wavenumber. The Love stress function is not provided as a closed form solution, although despite this, the function can be approximated numerically by using a sufficiently large number for the wavenumber

variable, k . Using the Love stress function along with Eqs. (3.28-3.31), the stress components are given explicitly as follows,

$$\sigma_{rr}(r, z) = \int_0^{\infty} f(k) \left[(1 - kz)J_0(kr) + (2\nu - 1 + kz) \frac{J_1(kr)}{kr} \right] e^{-kz} dk, \quad (3.37)$$

$$\sigma_{\theta\theta}(r, z) = \int_0^{\infty} f(k) \left[2\nu J_0(kr) + (1 - 2\nu - kz) \frac{J_1(kr)}{kr} \right] e^{-kz} dk, \quad (3.38)$$

$$\sigma_{zz}(r, z) = \int_0^{\infty} f(k) [(1 + kz)J_0(kr)] e^{-kz} dk, \quad (3.39)$$

$$\sigma_{rz}(r, z) = \int_0^{\infty} f(k) [2(1 - \nu)J_1(kr) + (2\nu - 2 + kz)J_1(kr)] e^{-kz} dk. \quad (3.40)$$

The effect of gravity, which manifests as hydrostatic pressure, can be added to the stress tensor as follows,

$$\bar{\sigma} = \begin{bmatrix} \sigma_{rr} & 0 & \sigma_{rz} \\ 0 & \sigma_{\theta\theta} & 0 \\ \sigma_{rz} & 0 & \sigma_{zz} \end{bmatrix} + \begin{bmatrix} -\rho g z & 0 & 0 \\ 0 & -\rho g z & 0 \\ 0 & 0 & -\rho g z \end{bmatrix}. \quad (3.41)$$

The Love stress function is also used to determine the displacements with Eq. (3.32) and (3.33), and are given as,

$$u_r(r, z) = -\frac{\nu + 1}{E} \int_0^\infty f(k) \left[(2\nu - 1 + kz) \frac{J_1(kr)}{k} \right] e^{-kz} dk, \quad (3.42)$$

$$u_z(r, z) = \frac{\nu + 1}{E} \int_0^\infty f(k) \left[(2\nu - 2 - kz) \frac{J_0(kr)}{k} \right] e^{-kz} dk. \quad (3.43)$$

With the stress state inside the half-space fully defined, the secondary principal stresses on planes perpendicular to the light propagation direction, i.e., the y axis, see Figure 3.1, can now be determined.

3.3.2 Secondary principal stress

Secondary principal stresses are the principal stresses in the plane orthogonal to the light propagation direction, and are used in calculating the optically equivalent model. In the schematic shown in Figure 3.1(a), the light propagates along straight lines parallel to the y -axis. This indicates that the secondary principal stresses lie on planes parallel to the x - z plane. It is, therefore, more convenient to determine secondary principal stresses from a cartesian coordinate system.

The stress tensor can be rewritten in terms of cartesian coordinates through a coordinate system transformation. Let the x and y stress components be designated by σ_{xx} and σ_{yy} , while the xz , and yz , shear stress components are designated by σ_{xz} and σ_{yz} , respectively. Note that, due to axial symmetry and the absence of torsion, the xy shear stress is zero, i.e., $\sigma_{xy} = 0$. The z stress component, σ_{zz} , remains unchanged since both coordinate systems' z axes coincide. The stresses in cylindrical coordinates are converted to cartesian coordinates through the following coordinate transformation,

$$\begin{bmatrix} \sigma_{xx} & 0 & \sigma_{xz} \\ 0 & \sigma_{yy} & \sigma_{yz} \\ \sigma_{xz} & \sigma_{yz} & \sigma_{zz} \end{bmatrix} \quad (3.44)$$

$$= \begin{bmatrix} \cos(\theta) & -\sin(\theta) & 0 \\ \sin(\theta) & \cos(\theta) & 0 \\ 0 & 0 & 1 \end{bmatrix} \begin{bmatrix} \sigma_{rr} & 0 & \sigma_{rz} \\ 0 & \sigma_{\theta\theta} & 0 \\ \sigma_{zr} & 0 & \sigma_{zz} \end{bmatrix} \begin{bmatrix} \cos(\theta) & \sin(\theta) & 0 \\ -\sin(\theta) & \cos(\theta) & 0 \\ 0 & 0 & 1 \end{bmatrix},$$

where θ is the angle between the r and x directions, see Figure 3.1(a). While all of the cartesian stress components are determined through Eq. (3.44), only the σ_{xx} , σ_{zz} and σ_{xz} , stress components are needed to determine the secondary principal stresses, which are calculated from,

$$\sigma_{1,2} = \frac{\sigma_{xx} + \sigma_{zz}}{2} \pm \sqrt{\left(\frac{\sigma_{xx} - \sigma_{zz}}{2}\right)^2 + \sigma_{xz}^2}. \quad (3.45)$$

The orientation of secondary principal stresses is given by,

$$\tan(2\phi) = \frac{\sigma_{xz}}{\sigma_{xx} - \sigma_{zz}}, \quad (3.46)$$

where ϕ is measured with respect to the x axis, see Figure 3.1(c). Note that in this analysis, only the in-plane (i.e., x - z plane, see Figure 3.1(a)) stresses are considered to contribute to the retardation (i.e., to stress-induced optical anisotropy), and no effect of stresses with components along the y -axis is considered. This is in line with the understanding that birefringence is induced by the stressing of a thin lamina in its plane and not by out-of-plane stresses.

To provide a representative model which approximates the experimental gelatin cuboid, the elastic half-space is segmented into a cuboid at sufficiently large distances away from the loading center. This segmented cuboid, with its secondary principal stresses determined, can then be used to determine the theoretical phase retardation in integrated photoelasticity.

3.3.3 Boundary effects

The elastic half-space is segmented into a cuboid with dimensions equal to the dimensions of the experimental cuboid in Figure 3.1(a). This segmentation exposes tractions on each of the side walls as well as the bottom surface. In the experiment, it is likely that friction exists between the gelatin and acrylic container during the Hertzian loading. This boundary condition will influence the stress state in the cuboid. To ensure that these tractions and boundary conditions are small in comparison to the Hertzian contact stress, the load applied to the sphere must be limited. Reasonable approximations can be obtained if the boundary is at least 4 contact radii away from the center of loading.

After the half-space is segmented into a cuboid, the secondary principal stresses and orientations are used in conjunction with Eqs. (3.14-3.16) to determine the phase retardation in the optically equivalent model. This provides a theoretical basis to compare with experiments. For the sake of comprehensiveness, the phase retardation can also be calculated using the optically equivalent model with stress states obtained through numerical simulations.

3.4 Numerical simulation

The goal of the simulations is to obtain the state of stress inside a material subject to a Hertzian contact and use this to obtain a simulated phase retardation field to compare with theory and experiments. Furthermore, the simulation can consider finite strains, which is analytically intractable, and assess the extent that the infinitesimal strain assumption negatively affects the results. The simulation aims to be representative of the Hertzian contact theory. Therefore, an axisymmetric domain is used where a rigid sphere is pressed into the top surface. The simulations are performed with computer aided engineering (CAE) software, Abaqus/Implicit, using a fine, rectangular 0.1 x 0.1 mm mesh with 4-node, reduced-integration, first-order, axisymmetric solid element (CAX4R) elements. The material properties match the theory and experiment, which have a linear elastic modulus of $E = 4.22$ kPa, Poisson ratio of $\nu = 0.49$, and density of $\rho = 1010$ kg/m³ (see Table 3). The contact between the sphere and material is frictionless and the applied force is given by $F = mg$, where m is the mass of the sphere, and $g = 9.81$ m/s² is the gravitational constant, which is also applied to the material to incorporate the effects of gravity. See Table 3 for the problem parameters and range of applied loads. The axial and radial length of the planar, axisymmetric domain is 60 x 60 mm², which is larger than the experimental domain so that boundary effects do not affect the results. The bottom edge is supported by an encastre boundary condition, while the vertical edge is supported by a frictionless boundary condition, which allows the material on the edge to move freely in the vertical direction but is restricted from movement in the radial direction. Figure 3.3 shows the simulation results on the r-z plane in terms of the von Mises equivalent stress. Figure 3.3(a) shows a zoomed-in view of the contact region where the largest von Mises

stress occurs. This is below the surface and is 0.959 kPa for a $m = 5$ gram sphere. Figure 3.3(b) depicts the entire domain where it is apparent that most of the stress is localized in the subsurface region directly below the sphere. The stress components obtained from the simulation are given in cylindrical coordinates, so, like in the theoretical derivation, Cartesian stresses are calculated using the coordinate transform of Eq. (3.44), while the secondary principal stresses and orientations are obtained using Eq. (3.45) and (3.46). This provides the stresses needed to determine the phase retardation in the optically equivalent model, which can then be compared to its theoretical and experimental counterparts. For this calculation, the axisymmetric simulation domain, i.e., cylinder, is segmented into a cuboid of dimensions $44 \times 44 \times 47 \text{ mm}^3$, as in the schematic shown in Figure 3.1(a).

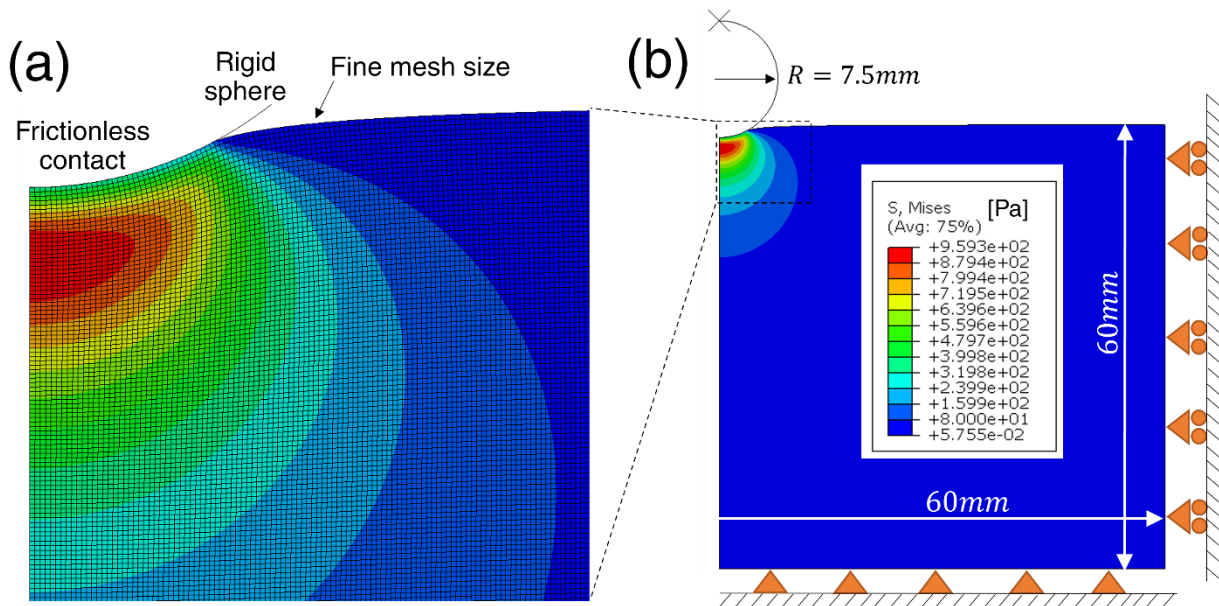


Figure 3.3: (a) Zoomed-in view of loading region depicting the Hertzian contact and FEA mesh-size. (b) Axisymmetric Abaqus model showing equivalent stress distribution on the r-z plane for $m = 5$ gram mass case.

3.5 Results and discussion

3.5.1 Phase retardation fields

Using the experimental setup devised in section 3.1.2, phase retardation fields are acquired for a variety of applied loads, see Table 3. Each of these loads are used to calculate the theoretical and numerical stress states, which are then used in determining the optically equivalent model and, thus, the theoretical and numerical phase retardation fields. Figures 3.4-3.7 show the phase retardation fields for the $m = 1, 5, 10,$ and 16 gram loading scenarios, respectively. Each figure contains an (a) experimental, (b) theoretical, and (c) numerical phase retardation field. The interrogation windows range from $0 \leq z \leq 10$ mm, and $-10 \leq x \leq 10$ mm, (normalized window of $0 \leq z/R \leq 1.33,$ and $-1.33 \leq x/R \leq 1.33$), which is outlined in Figure 3.1(a) as a dashed black line. This is also the domain used in determining the theoretical and numerical phase retardation fields. The center of the camera lens is aligned and parallel with the top surface of the gelatin, i.e., $z = 0$. The sphere is progressively submerged below this plane as the load increases in Figures 3.4 through 3.7.

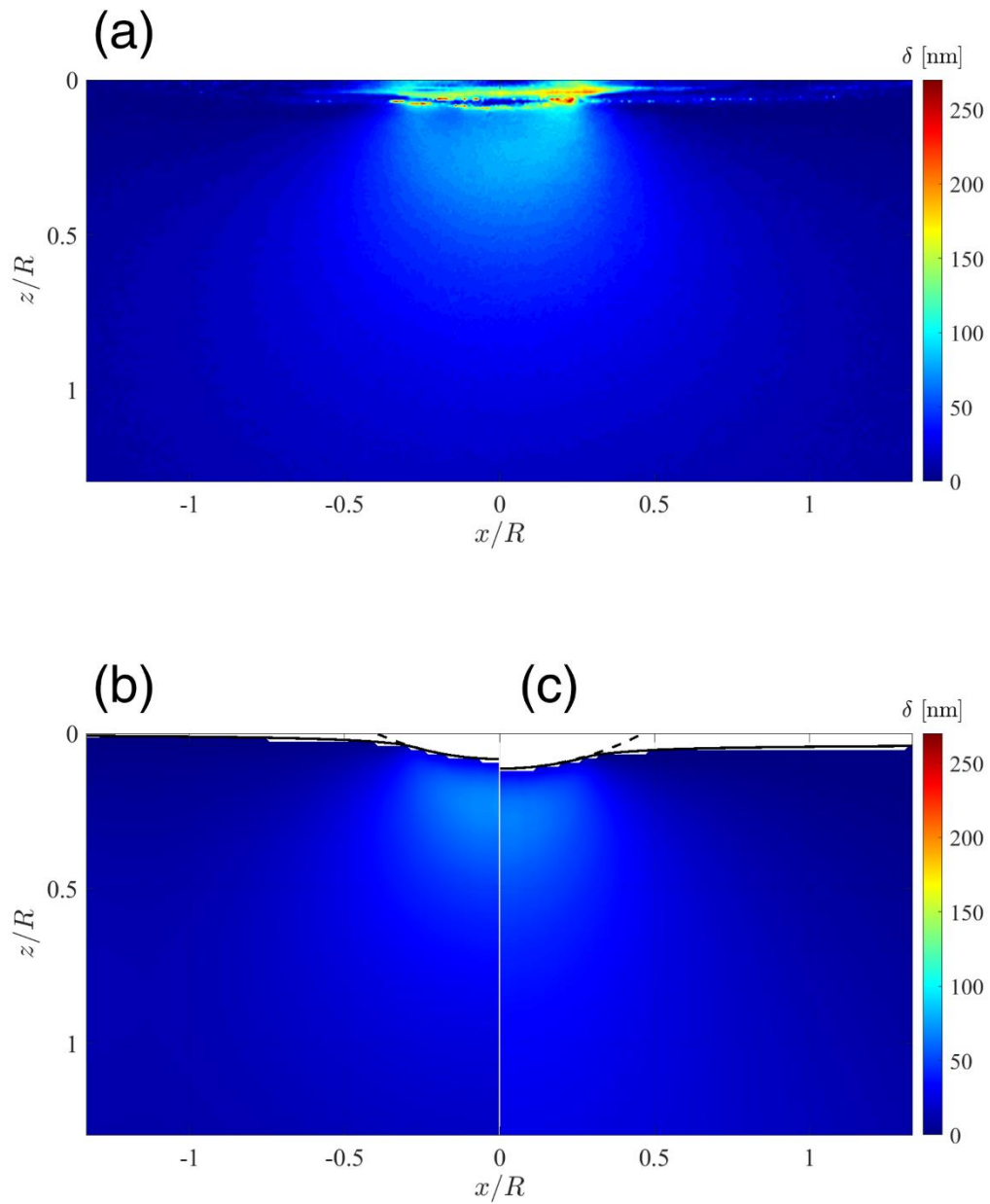


Figure 3.4: (a) Experimental, (b) theoretical, and (c) numerical phase retardation field for the $m = 1$ gram mass case.

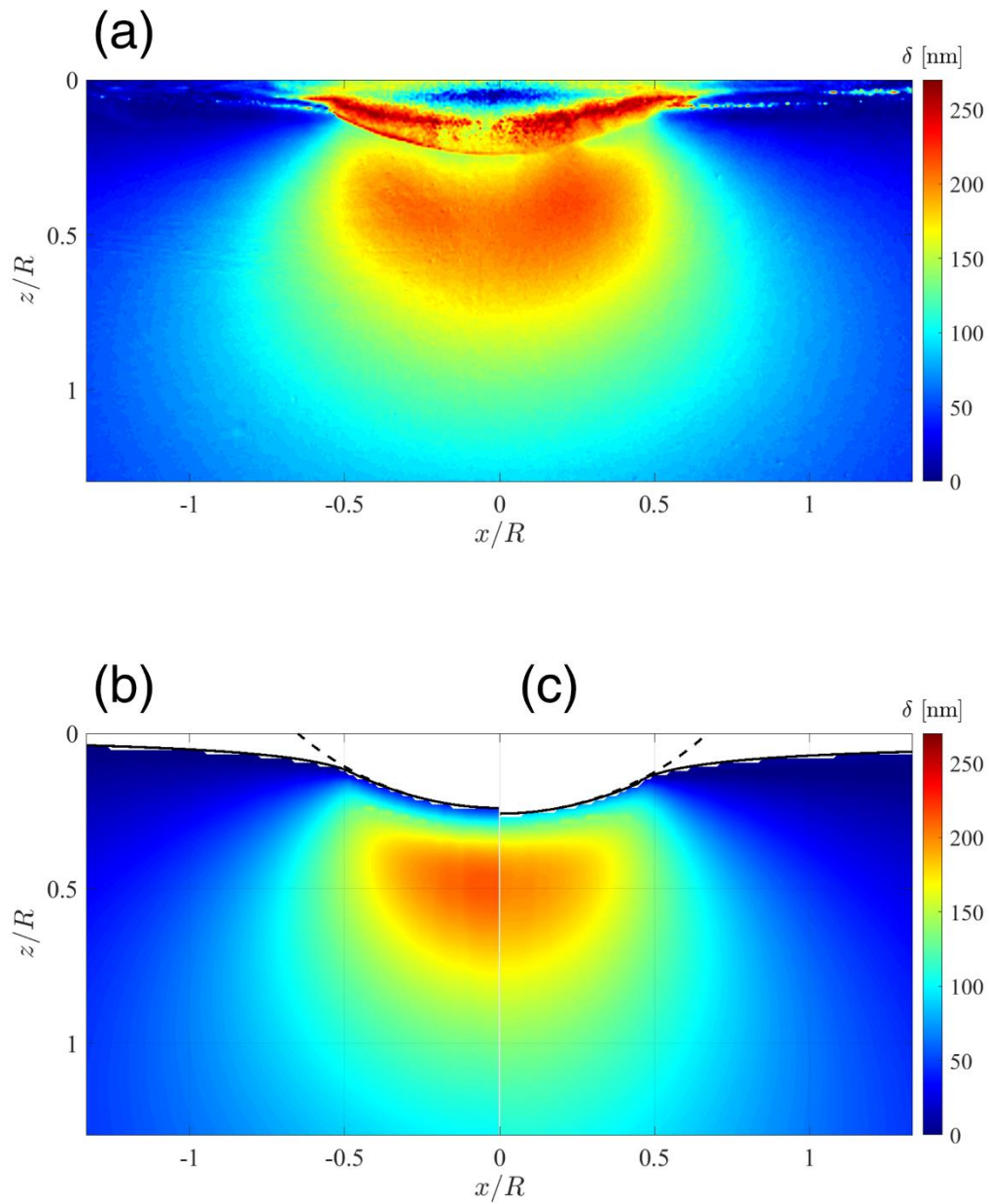


Figure 3.5: (a) Experimental, (b) theoretical, and (c) numerical phase retardation field for the $m = 5$ gram mass case.

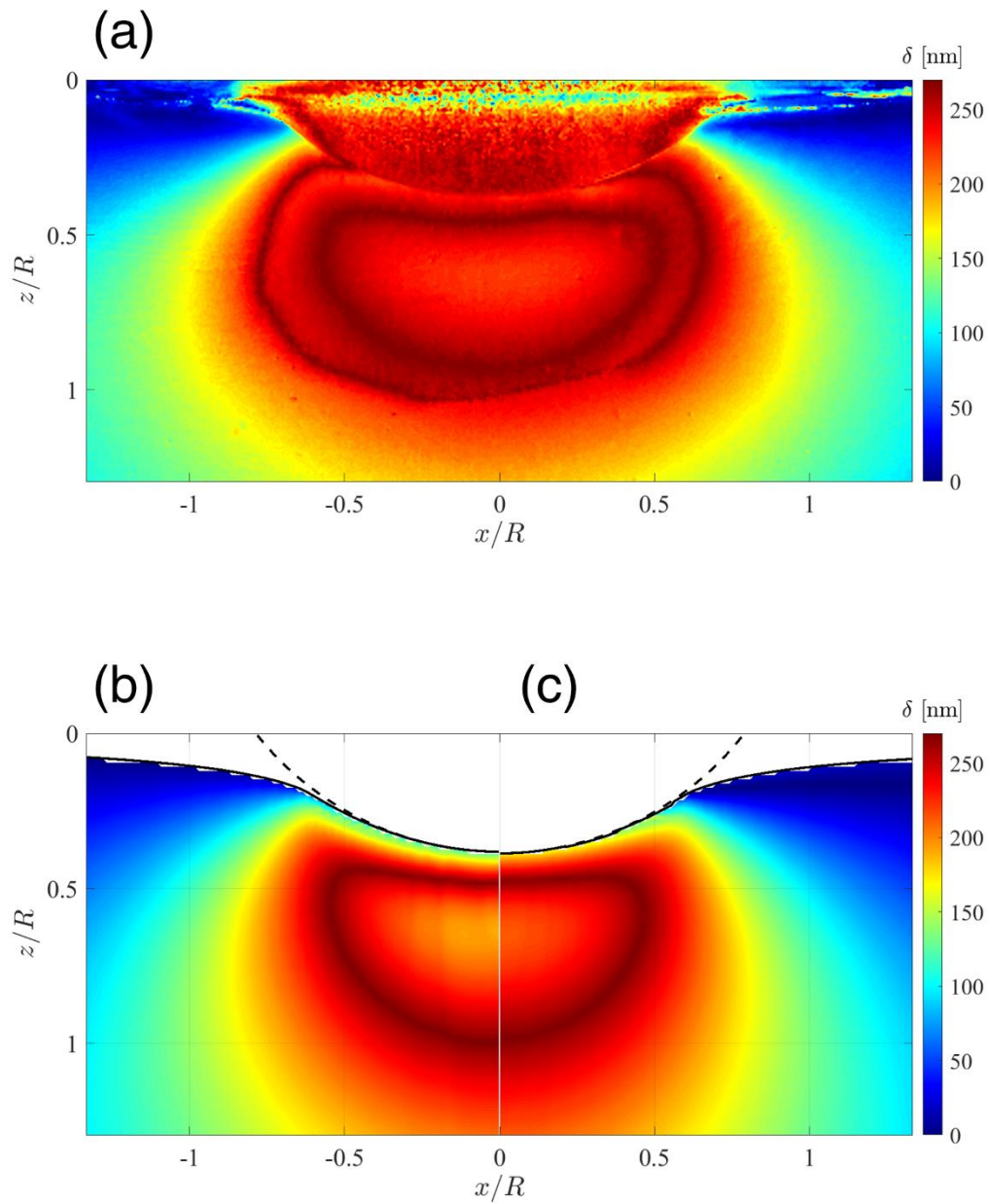


Figure 3.6: (a) Experimental, (b) theoretical, and (c) numerical phase retardation field for the $m = 10$ gram mass case.

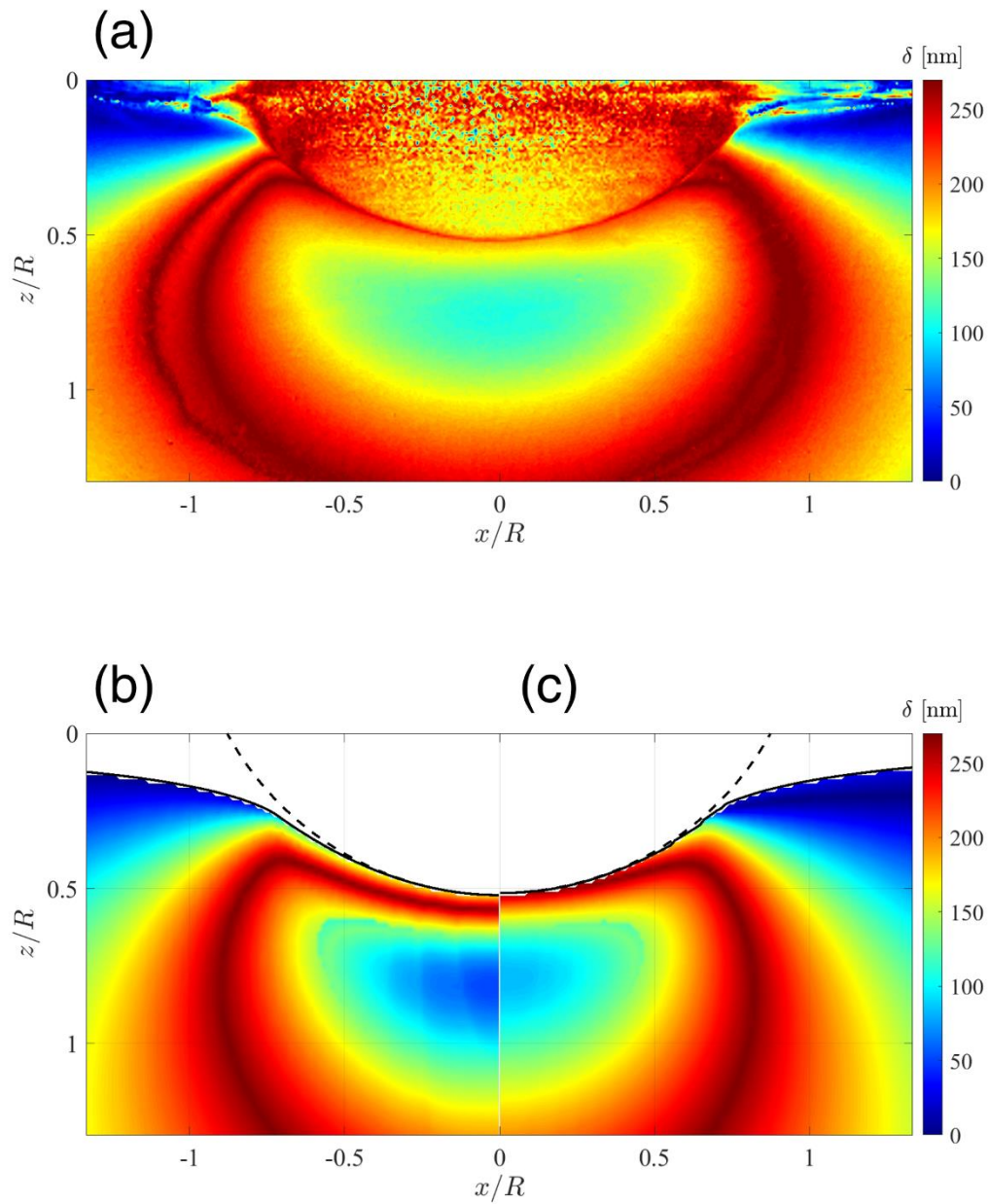


Figure 3.7: (a) Experimental, (b) theoretical, and (c) numerical phase retardation field for the $m = 16$ gram mass case.

It is apparent that all of the figures reveal a semicircular-shaped region of phase retardation in the center, underneath the sphere, and below the surface. The dark blue and dark red extremes correspond to the bounds of the experimental phase retardation field, which are 0 and 270 nm, respectively. The upper limit corresponds to one half of the wavelength of the light used, i.e., $\lambda/4 = 270$ nm. This range of phase retardation, i.e., $0 \leq \delta < 270$ nm, corresponds to an angular phase retardation of $0 \leq \Delta < \pi$. The experiments are limited to this range since, in photoelasticity, the emergent light is interpreted as major and minor electric field strengths on a light ellipse that range from 0 to π . When the actual phase retardation induced by the stressed material exceeds 270 nm, i.e., π , the measured phase will be recorded at a value less than 270 nm. This phenomenon is known as phase wrapping and can cause ambiguity in interpretation of measurement results. For the loading scenarios represented in Figures 3.4 and 3.5, the maximum phase does not exceed 270 nm; therefore, phase wrapping is not present. However, in Figures 3.6 and 3.7 phase wrapping exists and must be taken into account. In Figure 3.6(a), it can be seen that the maximum phase reaches 270 nm, i.e., red colored ring, while a relatively smaller phase retardation, indicated by the light red color, exists in the region inside the ring, below the sphere. It is here where care must be taken in analyzing the results. The light red region under the sphere, and inside the dark red ring, is interpreted as the highest phase retardation, which, according to the scale, is approximately 220 nm. For this scenario, the unwrapped maximum phase retardation is calculated as $\delta^{max} = 270 + (270 - 220) = 320$ nm. A similar phase wrapping situation exists for the theoretical and numerical fields of Figure 3.6(b) and (c). Here, the unwrapped maximum phase retardation is 348 nm and 326 nm, respectively. This identifies fair agreement between the maximum phase

retardation of the experiment and its theoretical and numerical counterparts. The semicircular shaped contours and their relative positions in Figures 3.4-3.6 also show qualitative agreement. This suggests that the experiments are capturing the phase retardation induced by the Hertzian contact.

The phase retardation fields of the $m = 16$ gram mass, shown in Figure 3.7, begin to identify discrepancies between experiments, theory, and numerics. Although they share the same general shape and qualitative characteristics, the maximum phase retardation, inside the dark red rings, do not exhibit the same value. The experiments show a light green color, while the theory and numerics reveal a blue and cyan color, respectively. Here, deviations in maximum phase retardation become apparent. It is possible that, in the experiments, the stress field is extending toward the container boundaries resulting in an alteration of the Hertzian contact. Furthermore, the contact radius is becoming large and close to the radius of the sphere, which violates the Hertzian contact assumptions. These results, shown in Figure 3.7, are characteristic of large loads and displacements.

The maximum (unwrapped) phase retardation is determined for each of the fields shown in Figures 3.4-3.7, as well as for the theoretical and experimental tests listed in Table 3. Figure 3.8 shows the relationship between maximum phase retardation and applied force for the experiment (red circles), theory (blue dots), and numerical (green triangles). For small load cases, i.e., $F < 100$ mN, excellent agreement is observed between experiment, theory, and numerical simulations. However, for higher load cases, the experimental phase retardation deviates from the theoretical and numerical phase retardations. Again, this deviation is likely due to the excessive load, which makes the contact radius approach the radius of the sphere, where the Hertzian contact

approximation becomes invalid. It is evident that the relationship between maximum phase and applied force is non-linear. This relationship is examined, in detail, in the following section.

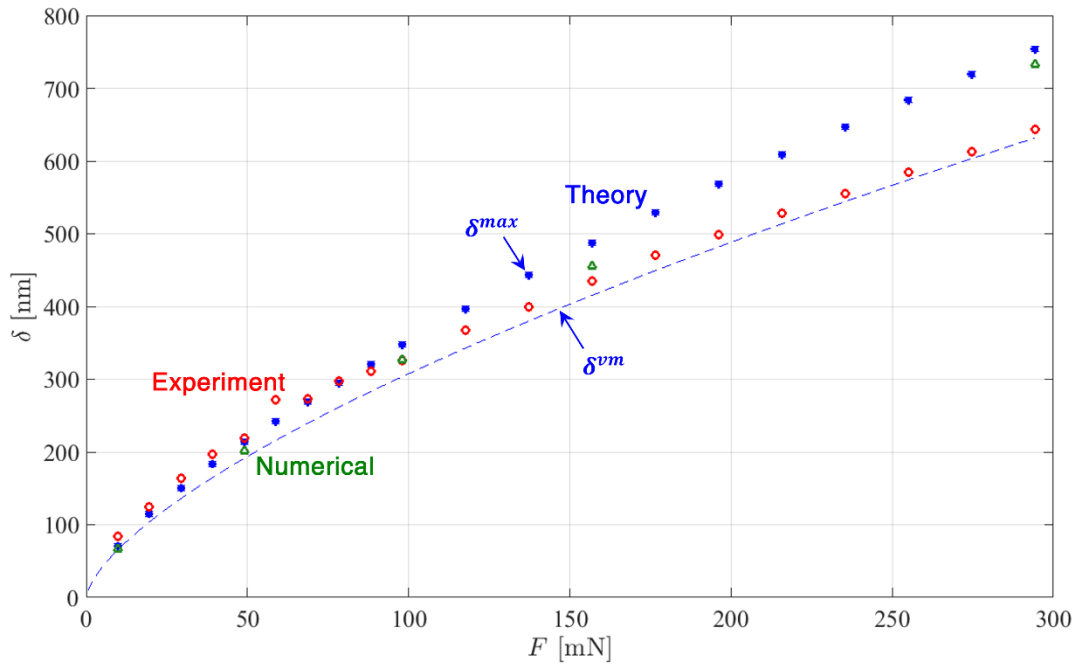


Figure 3.8: Relationship between maximum phase retardation and applied force for experiment (red circles), theory (blue dots), and numerical (green triangles). The phase retardation passing through the point of maximum von Mises stress, given by Eq. (3.50), is presented with a dashed blue line.

Overall, for small load cases, i.e., $F < 100$ mN, good agreement is established between experiment, theoretical, and numerical phase retardation results, for each of the loading conditions. This indicates that the theoretical and/or numerical models can be used for interpreting the stress state inside the gelatin. Again, it is not possible to solve the inverse problem in integrated photoelasticity, where, in a tomographic sense, stress fields are determined solely from an experimental phase retardation field for the entire domain. The fact that agreement is established suggests that the models used, and assumptions made are appropriate for this specific problem. In addition, this agreement serves to validate

the Hertzian contact theory as well as the numerical model. Phase retardation fields provide insight into the mechanics and identify areas of maximum phase retardation; however, the most important parameter, with respect to the onset of yielding, is the equivalent stress.

3.5.2 Maximum equivalent stress and principal stress components

In each of the loading scenarios, the maximum phase retardation occurs below the surface and along the z-axis. Everywhere along the z axis the Cartesian stress components σ_{xx} and σ_{zz} , coincide with the principal stresses σ_1 and σ_2 . The out of plane stress component σ_{yy} , coincides with the third principal stress σ_3 , and is equal to the x stress component $\sigma_{yy} = \sigma_{xx}$, [122]. Furthermore, due to symmetry, the shear stress components are zero along the z-axis, i.e., $\sigma_{xz} = \sigma_{yz} = 0$. Using these relations, it is straightforward to see that the von Mises equivalent stress, which is given by,

$$\sigma_{VM} = \sqrt{\frac{(\sigma_1 - \sigma_2)^2 + (\sigma_2 - \sigma_3)^2 + (\sigma_3 - \sigma_1)^2}{2}}, \quad (3.47)$$

is reduced to a simple relationship given by,

$$\sigma_{VM} = (\sigma_1 - \sigma_2). \quad (3.48)$$

Here, the Mises stress is simply the difference between first and second principal stresses. This relationship holds everywhere along the z axis, which includes the point of maximum von Mises stress. For points outside of the z axis, Eq. (3.47) is used to calculate

von Mises stress. The von Mises stress, according to the theoretical model, is evaluated at the $y = 0$ mid-plane, for the $m = 5$ gram loading case and is shown in Figure 3.9. It is apparent that the largest magnitude (dark red) occurs at the center, i.e., $x = 0$, and below the surface. The contours of constant von Mises stress are elliptically shaped with vertices that extend upward, towards the surface.

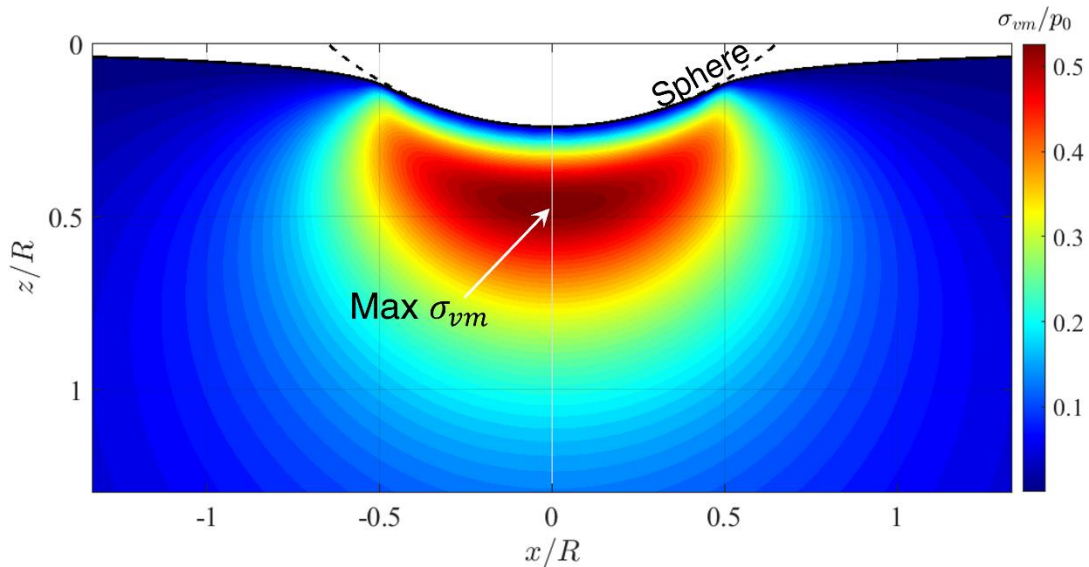


Figure 3.9: Theoretical von Mises stress evaluated on the $y = 0$ mid-plane for the $m = 5$ gram load case. The maximum stress occurs below the surface as anticipated by Hertzian contact theory.

For light rays passing through the z axis, i.e., $x = 0$ plane, the integral Wertheim law, Eq. (3.3), is applicable, as there is no rotation of principal directions along this plane. Also, along the $x = 0$ plane, there is no σ_{xz} shear. Therefore, the secondary principal stresses reduce to $\sigma_1 = \sigma_{zz}$, and $\sigma_2 = \sigma_{xx} = \sigma_{\theta\theta}$. With these variables it may seem like this integral, i.e., Eq. (3.3), is reduced in complexity, however, a closed form solution of the integral does not exist, according to the authors' knowledge.

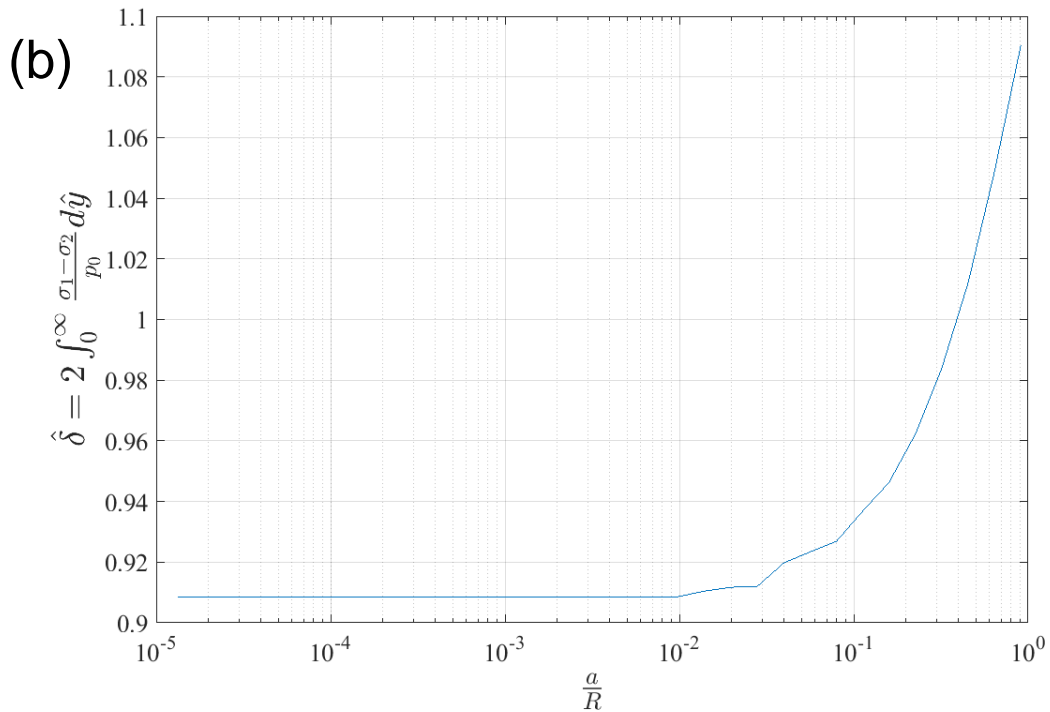
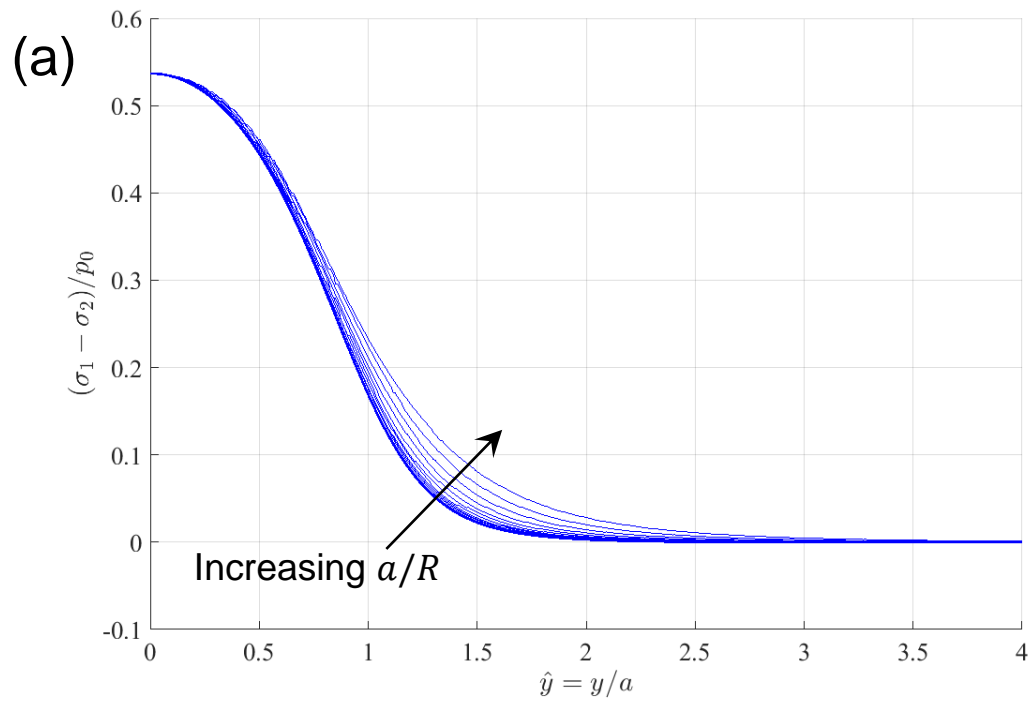


Figure 3.10: (a) Secondary principal stress profile along the light propagation direction, $\hat{y} = y/a$, of rays passing through maximum von Mises stress σ_{vm} , for a range of load cases, i.e., $10^{-5} < a/R < 1$. For small loads, i.e., $a/R \ll 1$, stress profiles are self-similar. (b) Normalized area under the stress profiles shown in (a), where a constant value, i.e., $\hat{\delta} = 0.91$, is observed for $a/R \ll 1$.

To examine the behavior of this integral, stress profiles are plotted for a variety of load cases, $10^{-5} < a/R < 1$, in Figure 3.10(a), for light rays passing through the point of maximum von Mises stress. For small loads, i.e., $a/R \ll 1$, the stress profiles are invariant, revealing self-similarity. However, for increasing loads, $a/R \rightarrow 1$, stress profiles deviate from the self-similar profile, and show a greater secondary principal stress difference in the range, $1 < \hat{y} < 2$, see Figure 3.10(a). The normalized area under each of these profiles, which is given by,

$$\hat{\delta} = \frac{\delta}{cp_0a} = 2 \int_0^{\infty} \frac{(\sigma_1 - \sigma_2)}{p_0} d\hat{y}, \quad (3.49)$$

is shown in Figure 3.10(b) for each load case. It is apparent that for small loads, i.e., $a/R \ll 1$, the integral value is a constant $\hat{\delta} = 0.91$, while for large loads, $a/R \rightarrow 1$, the integral value is ever-increasing. For these large loads, the contact radius approaches the sphere radius, where the Hertzian contact approximation becomes invalid. For the small loads, however, the constant $\hat{\delta} = 0.91$ identifies a relatively simple relationship between the phase retardation passing through σ_{vm}^{max} and applied force, which is given by,

$$\delta^{vm} = 0.91 \frac{c}{\pi} \left(\frac{9E^* F^2}{2R} \right)^{1/3}. \quad (3.50)$$

This equation is plotted in Figure 3.8 as a dashed blue line. It is apparent that this line qualitatively follows the data trends, but deviates from the blue dots with increasing load.

For increasing load, the stress profiles, passing through σ_{vm}^{max} , deviate from the self-similar profile, producing a larger integral value, i.e., Eq. (3.49), and thus, yield a phase retardation greater than that predicted by Eq. (3.50). Hence, Eq. (3.50) is only applicable in the small load limit, i.e., $a/R \rightarrow 0$. Nonetheless, Eq. (3.50) provides insight into the relevant parameters of the Hertzian, integrated photoelasticity problem. For example, it is evident that phase retardation scales with force to the $2/3^{\text{rd}}$ power. Using this relation, one could use Hertzian loading in integrated photoelasticity as a load cell (within the small load approximation).

Using Eq. (3.48), the maximum von Mises stress is calculated for each load case, using the theoretical and numerical stresses. The axial position of maximum von Mises stress is approximately the same axial position as the maximum phase retardation. Figure 3.11 shows the relationship between maximum von Mises stress (which is also the maximum secondary principal stress difference) and maximum phase retardation for each of the loading conditions. The theoretical data points are presented with blue dots, while the numerical data points are shown with green triangles. For increasing load, the numerical results deviate from theory. This may be attributed to the difference in loading conditions between theory and numerics, as the theory uses a pressure boundary condition while the numerical simulation use rigid contact, i.e., displacement boundary condition.

One may be tempted to use the experimental results and the classic “2D” stress optic law, Eq. (3.4), to obtain the principal stress difference; however, this would yield erroneous results, as they would produce the averaged principal stress difference across the depth of the cube. Another method is needed to use the experimental results.

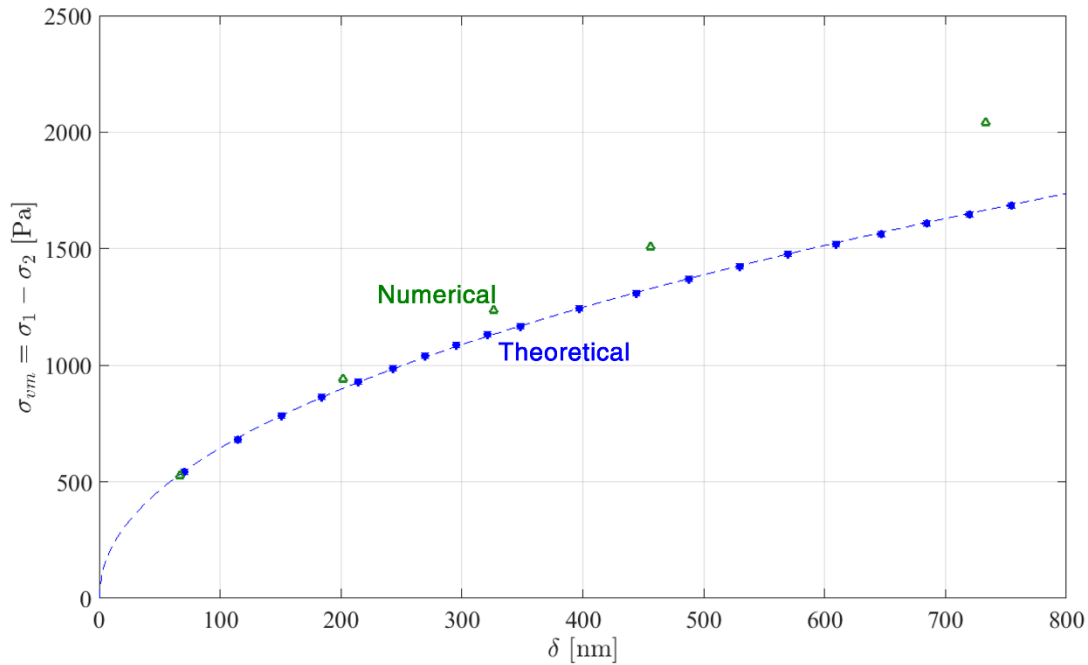


Figure 3.11: Relationship between maximum von Mises stress and the maximum phase retardation, evaluated on the $y = 0$ mid-plane, according to theory (blue) and numerical simulation (green). A fit line is applied to the theoretical data, given by Eq. (3.51).

In order to use the experimental data for stress reconstruction, (specifically, using the maximum phase retardation to calculate the maximum von Mises stress), the theoretical fit line in Figure 3.11 can be employed which is given by,

$$\sigma_{vm} = (\sigma_1 - \sigma_2) = a\delta^n, \quad (3.51)$$

where fit parameters a and n , are 71.9 Pa/nm and 0.48, respectively. Therefore, if given only a maximum phase difference, the maximum von Mises stress can be determined using this relationship. Hence, information about the stress state can be obtained from experimentation.

The von Mises stress is an important parameter when identifying the maximum stress state; however, it is also advantageous to know each individual principal stress component. Equation (3.51) cannot provide each principal stress component directly (only their difference is provided). Another equation is needed to determine each stress value. Here, it is recognized that the ratio between first and second principal stress components can be evaluated using Eq. (3.37) and (3.39) at any point along the z axis. This relationship is evaluated at the axial position where von Mises is maximum, and is given by,

$$\frac{\sigma_1}{\sigma_2} = \frac{\int_0^\infty f(k)[1 + kz]e^{-kz} dk}{\int_0^\infty f(k) \left[\frac{1}{2}(1 - kz) + \nu \right] e^{-kz} dk}. \quad (3.52)$$

This ratio is invariant with respect to E , although is dependent on ν . However, since gelatin exhibits nearly incompressible behavior, the Poisson ratio is almost always $\nu = 0.49$. In the limit of small loads, i.e., $a/R \ll 1$, this ratio is constant, $\sigma_1/\sigma_2 = 3.3$. By using this ratio, in conjunction with Eq. (3.48), the first and second principal stresses can be determined, and since $\sigma_3 = \sigma_2$ everywhere along the z axis, all three principal stresses are known at this location. This fully defines the stress state where the von Mises stress is maximum, providing crucial insight for yield forecasting.

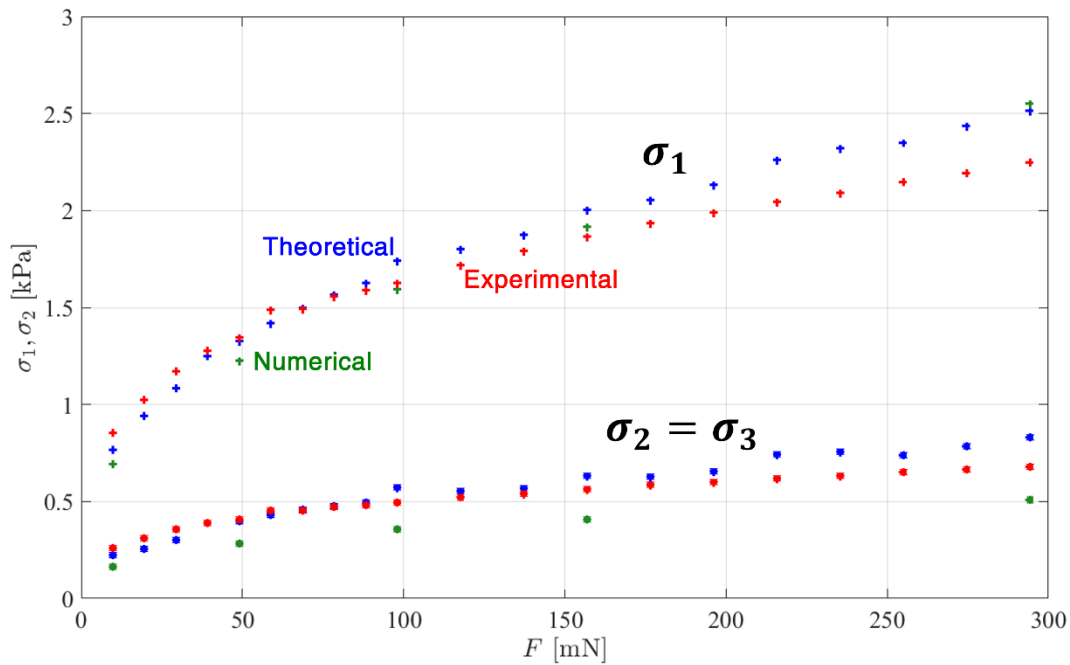


Figure 3.12: Principal stress components at the point of maximum von Mises stress for theory (blue), experiments (red) and numerical simulation (green). ‘Plus’ symbols are used for σ_1 , while ‘dots’ are used for σ_2 , respectively.

Using the experimental maximum phase retardation δ^{max} , the von Mises stress is calculated using Eq. (3.51), and using the stress ratio of 3.3, the first and second principal stress components are determined for each of the load cases, which are plotted in Figure 3.12. Blue, red and green crosses represent the theoretical, experimental and numerical first principal stresses, respectively, while blue, red and green dots represent the theoretical, experimental and numerical second principal stresses, respectively. Satisfactory agreement is observed between theory and experiment for each stress component. This demonstrates that, by determining the phase retardation through experimentation, one can fully determine the stress state at the most critical point within the material.

3.5.3 Maximum surface displacement and contact radius

Another important parameter in the Hertzian contact problem is the displacement of the surface immediately below the sphere. According to Hertzian contact theory [122], the maximum displacement is given by Eq. (3.1). Figure 3.13 shows this relationship with respect to applied force, as a dashed blue line. The maximum experimental displacements, recorded by the camera, are represented by red circles. This is the distance between the $z = 0$ surface and the location of the sphere bottom. The maximum displacements found in the numerical simulations are also plotted on Figure 3.13 as green triangles. From the figure, it is apparent that the experimental displacements follow the trend of the theory and numerical simulations, as expected. Recall that the Young's modulus is determined by fitting the theoretical and experimental displacements through Eqs. (3.1) and (3.2).

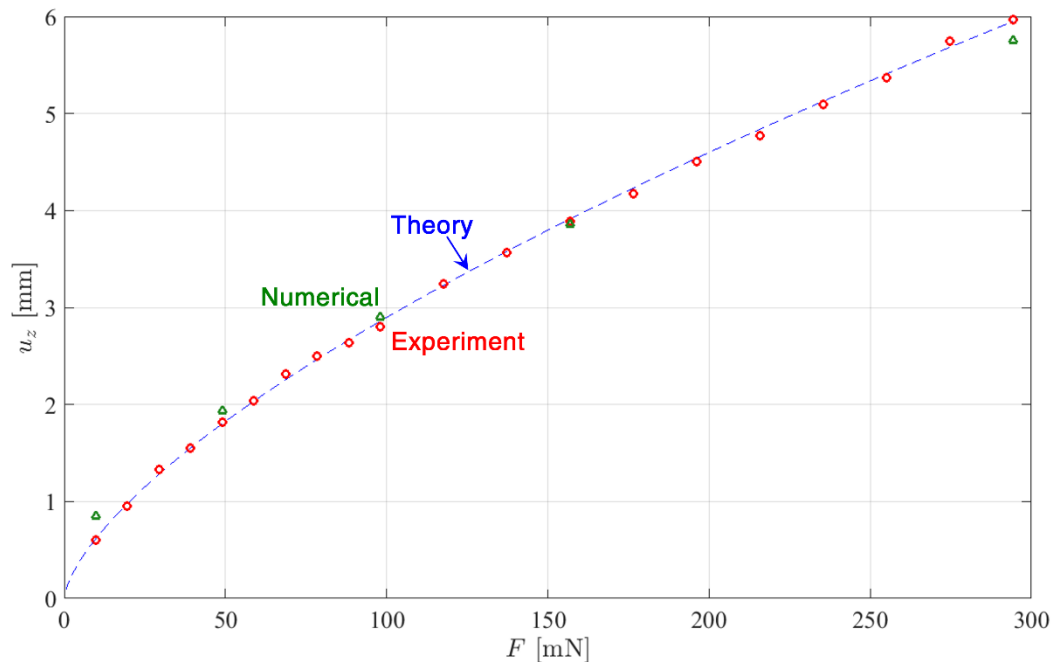


Figure 3.13: Relationship between maximum displacement and applied force for theory (blue dashed line, Eq. (3.1)), numerical (green triangle), and experiment (red circles).

The theoretical radius of contact between the surface of the gelatin and sphere is given by Eq. (3.20), where contact radius, a , scales with applied force to the $1/3^{\text{rd}}$ power. This relationship is shown in Figure 3.14 as a dashed blue line, while the numerical contact radius is plotted with green triangles. The experimental contact radius is defined as the distance between the center of the sphere and the point where the sphere separates from the gelatin, which is determined using the camera. It is noted that the experimental uncertainty in contact radii measurements are larger than the uncertainty in determining maximum displacement due to the ambiguity in identifying the radial coordinate where the sphere separates from the gelatin. The experimental data points are represented by red circles in Figure 3.14, where reasonable agreement is established with respect to theory and numerical simulations. The differences here are only a fraction of a millimeter. This agreement supports the assumptions made in section 3.3 and appear to be valid even for the largest loading scenario.

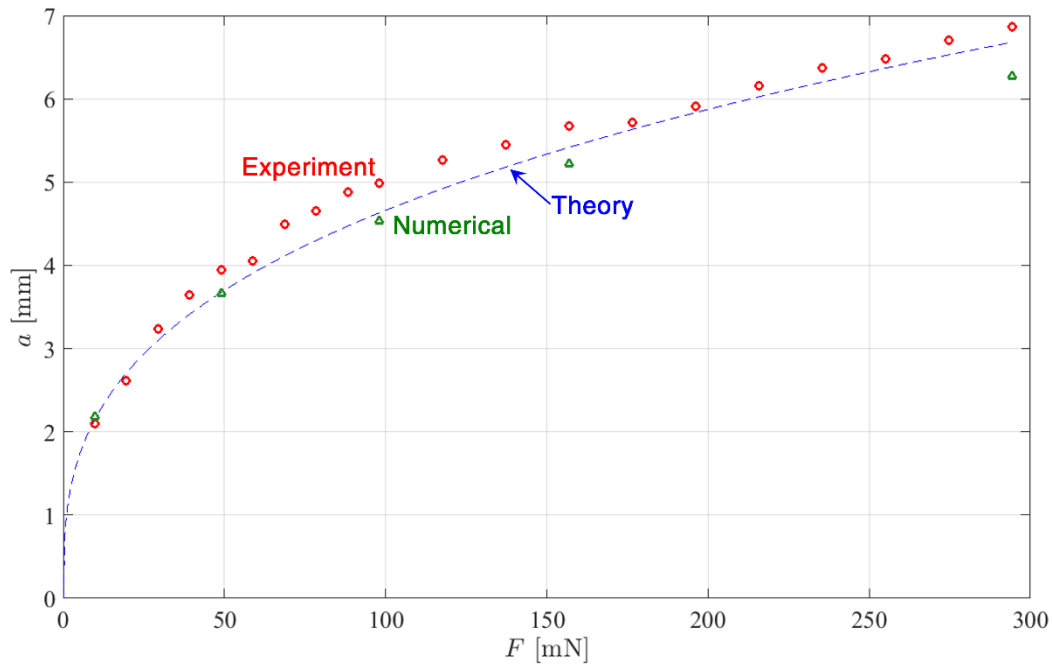


Figure 3.14: Relationship between contact radius and applied force for theory (blue dashed line, Eq. (3.20)), numerical (green triangle), and experiment (red circles).

3.6 Summary

Integrated photoelasticity is used to analyze the Hertzian contact problem of a rigid sphere loaded onto the top surface of a soft-solid, gelatin. The theoretical stress state of the gelatin is derived using the Love stress function and Hankel transform method, which provides the stress tensor across the entire problem domain. The stress inside the gelatin is also calculated using numerical simulations. Both theoretical and simulated stress states are used in conjunction with the optically equivalent model to predict the phase retardation field expected in an integrated photoelasticity experiment. Experiments are carried out on a gelatin cuboid where excellent agreement is observed between theoretical and numerical predictions and the experimental phase retardation fields. A non-linear correlation is established between the maximum phase retardation and maximum equivalent stress for a variety of sphere loading conditions. This allows one to

determine the maximum stress state in the Hertzian contact problem solely by conducting an integrated photoelasticity experiment. This is important because it identifies the position and magnitude where stress is maximum and, therefore, signifies where material yielding is expected to occur first.

The agreement between experimental and theoretical results is also assessed through the maximum surface displacement and contact radius. The experiments show excellent agreement with theory according to surface displacement, while fair agreement is observed regarding the contact radius. The successful determination of maximum equivalent stress and principal stress components at this location with integrated photoelasticity suggests that this method can be applied to similar, axisymmetric loading scenarios. Future studies will explore the viability of measuring equivalent stress and principal stress components for dynamic loads on gelatin media, such as the impact of a droplet. Knowing the stress components during droplet collapse will be essential in order to understand the erosion mechanisms during WDM.

4. WATER DROPLET MACHINING PROCESS AND EROSION CHARACTERISTICS

(Although most of the work presented in this section is new and unpublished, some of it is taken from taken from [158], i.e., Mitchell, B. R., Demian, S. A., Korkolis, Y. P., & Kinsey, B. L. (2020). Experimental comparison of material removal rates in abrasive waterjet cutting and a novel droplet stream technique. *Procedia Manufacturing*, 48, 586-592. My contributions were all experiments and analyses. The construction of the WDM device shown herein was also a significant undertaking.)

Waterjet cutting is a conventional manufacturing process, used widely across industries such as aerospace, automotive, medical, electronics and robotics [159]. Industrial waterjets are often classified as either an abrasive waterjet (AWJ) or pure waterjet (PWJ). Both types feature high-speed liquid, i.e., 100 m/s, emanating from an orifice with high backing pressure, i.e., 400 MPa, and are favorable for cutting temperature-sensitive materials as low thermal damage is produced compared to other cutting processes such as milling, sawing, plasma, and laser cutting. An AWJ machine utilizes a multi-phase slurry of abrasive particles mixed with high-speed water (and entrained air), to collide with and erode a workpiece. These machines are favorable for their ability to cut high-strength materials, where plowing of abrasive particles is the dominant material removal mechanism [160-162]. This produces high erosion rates, which, therefore, facilitates fast manufacturing times. In contrast, the drawbacks of AWJ include a high manufacturing cost due to the purchase and disposal of abrasives, the associated environmental cost, as well as embedment of abrasives into the workpiece, which reduces its surface integrity. A PWJ does not feature these drawbacks but suffers from low erosion rates and is limited

to soft materials, e.g., rubber, wood, plastic. It has been shown, however, that when PWJ is pulsed, such that a spray of droplets is produced, material removal is enhanced [163-165]. This is attributed to the high impact pressures and stress waves generated when a droplet impinges a surface [24, 166, 167]. The spray produced by a pulsed PWJ propels droplets away from the jet axis, and into the transverse direction. This leads to wide erosion footprints, i.e., much larger than the orifice diameter, which is beneficial for applications such as coating removal and surface profiling, where scouring a large surface area is desired. However, this is unfavorable for through-cutting applications, where precise and narrow kerfs are required. Through-cutting with a PWJ is typically performed at small standoff-distances SOD, i.e., < 5 mm, which is the distance between the waterjet orifice and workpiece. In this scenario it is likely that the waterjet is a continuous/semi-continuous stream upon impact with the workpiece. In Chapter 2 it is shown, experimentally, and through theory, that higher forces occur when a train of droplets impact a surface, rather than a continuous Rayleigh jet, of equal momentum. This finding suggests that a droplet train has a higher erosive potential, and hence, using a PWJ in the droplet-train configuration would perform better than its continuous stream counterpart.

To create a droplet train capable of material erosion, sufficiently high impact velocities are most likely required. In order to form a Rayleigh jet at high-speed, the Weber number condition must be satisfied, i.e., $We_{gas} = \rho_{gas}dv^2/\sigma < 0.4$, which is difficult to achieve as the Weber number scales quadratically with jet velocity. Industrial PWJs (almost always) use water as the cutting liquid, which, therefore, limits many of its intrinsic properties, including surface tension. PWJs, can satisfy the Weber number condition for small jet

diameters and for small ambient gas densities. A PWJ diameter decrease can easily be done by swapping-out the machine's orifice with the smallest industrial orifice available, i.e., 75 μm , but decreasing the ambient gas density is non-trivial in most atmospheric pressure environments. It has been postulated, however, that the low Weber number can be achieved by immersing the PWJ in a sub-atmospheric pressure environment [4]. It is imperative that the low ambient pressure be maintained on the backside of the workpiece, during a through-cut, to preserve the Weber number condition at/near the droplet impact location. Hence, contrary to the proposal [4], isolating both the workpiece and waterjet in the low-pressure environment would be most practical for through-cutting applications. It can be deduced that the use of high-speed droplet impacts, as a method to erode and cut through workpieces, is an effective manufacturing tool, while simultaneously eliminating the drawbacks of AWJ. This manufacturing technique is referred to, herein, as water droplet machining (WDM). The cut characteristics of this of this novel technique are currently absent in the scientific literature, and a thorough description of its performance as a manufacturing tool is lacking. It is, therefore, worthwhile to explore the erosion characteristics, and process parameters which render WDM an effective machine tool. This chapter aims to achieve this by experimentally assessing the erosion footprint of WDM on high-strength materials, like steel, through a variety of test conditions.

4.1 State of the art

To effectively erode a workpiece material, the water droplet machining process relies on the generation of large impact pressures, which is facilitated by high-speed droplet impingement at the workpiece surface. It is necessary to perform the technique within a

low-pressure environment to mitigate aerodynamic drag and atomization of the waterjet/droplet train into a fine, ineffective mist. For through cutting, it is advantageous to decrease the width of the waterjet and droplet train to reduce kerf width, and therefore, increase cut precision. To achieve this, lowering the jet Weber number towards the Rayleigh-jet configuration is highly sought-after. It is also imperative that a series of droplet impacts occur instead of a continuous jet. Accordingly, the distance between the orifice and droplet formation zone is a parameter of significant importance. Poor erosion rates are expected if the stand-off distance is less than the droplet break-up length. Limited studies have investigated this length for extremely fast jets [168, 169], such as the $O(100 \text{ m/s})$ waterjet used in this study. Therefore, the experimental setup is designed to explore unconventionally large SOD and characterize the influence of SOD on erosion rate. Note that the droplet break-up length can be shortened by methods described in section 2.2.4, however, in the experiments outlined in this chapter, droplet formation is left to occur naturally.

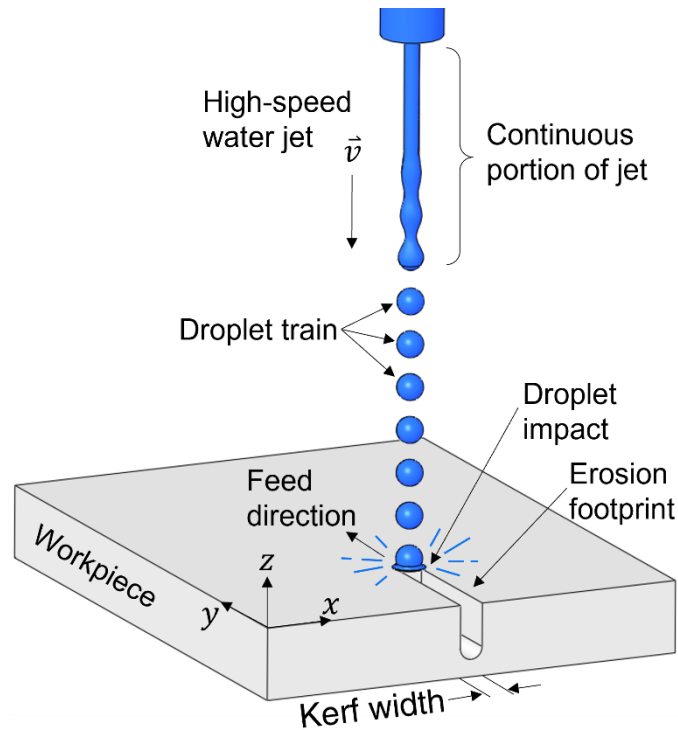


Figure 4.1: Diagram of the idealized Water Droplet Machining process, in through-cutting mode, using a high-speed Rayleigh jet, which produces a train of droplets that impact and erode a workpiece. As the jet moves across the workpiece an erosion footprint is created which resembles a trench (or through-cut) with depth related to jet feed rate.

A generalized diagram of the WDM process is shown in Figure 4.1, where high pressure water is accelerated through an orifice producing a continuous jet, which, with downstream evolution, segments into droplets. WDM is performed within a vacuum chamber to isolate the droplets and workpiece from atmospheric pressure, i.e., air. The gas surrounding the waterjet/droplet train is mixture of water vapor and small fragmented droplets formed after colliding with the workpiece. When high-speed droplets impinge the workpiece, large pressures are generated due to the “water-hammer” effect. Upon impact, the liquid at the base of the droplet behaves in a compressible manner, where the impact pressure is given by,

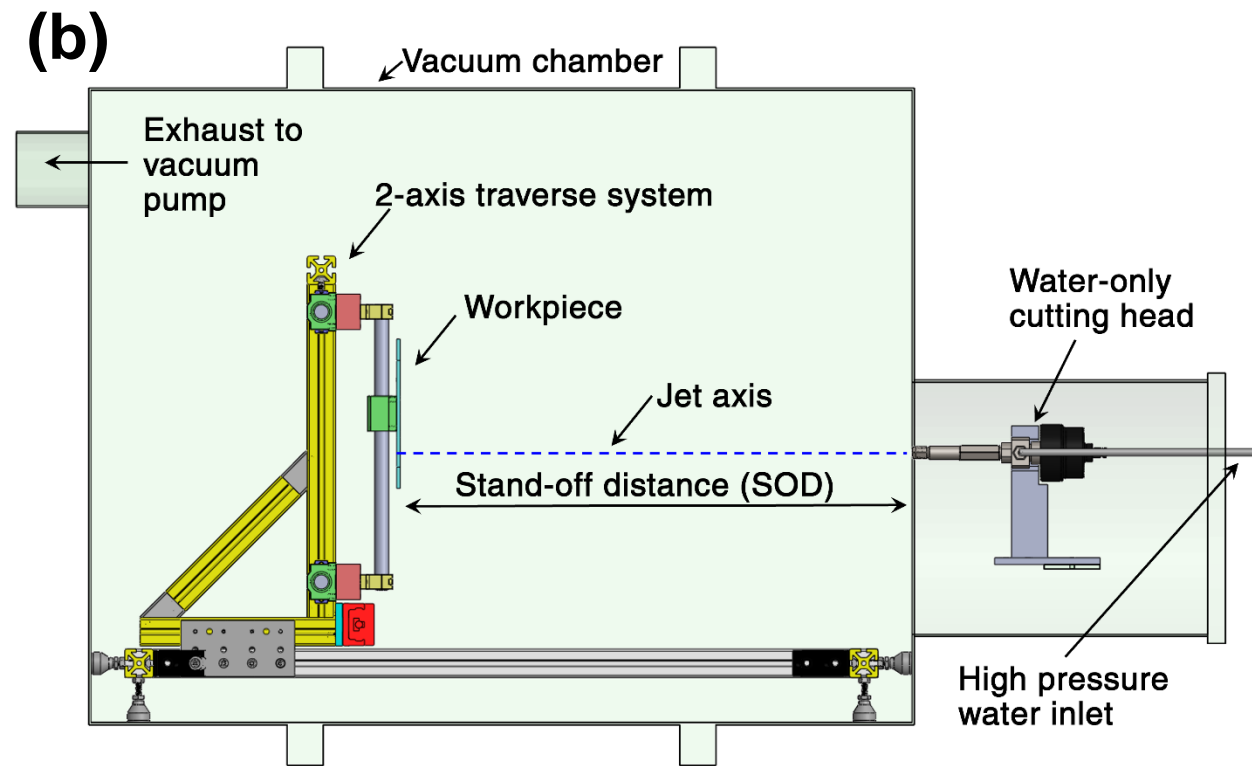
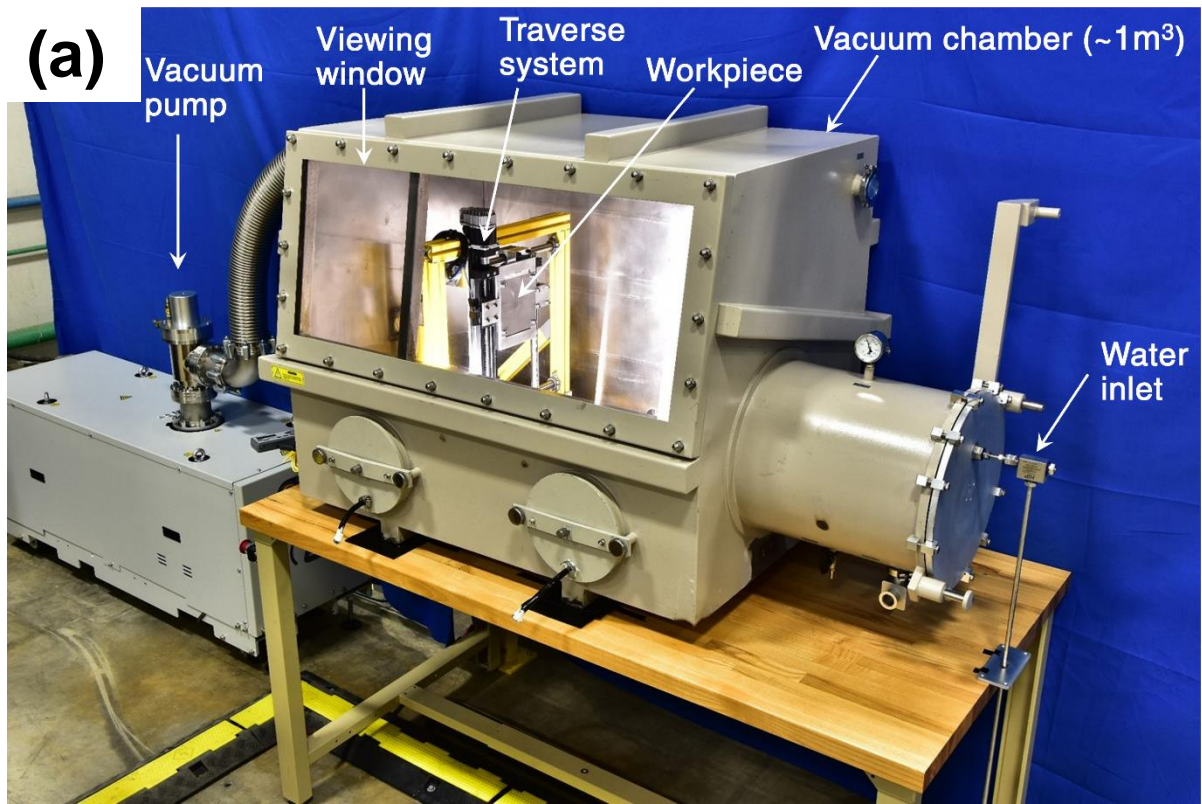
$$p = \rho cv , \quad (4.1)$$

where $\rho = 998 \text{ kg/m}^3$ is the water density, $c = 1450 \text{ m/s}$ is the sound speed of water, and v is the impact velocity [13]. This pressure gives rise to propagating shock waves both in the workpiece and in the collapsing droplet, as a sudden redirection of momentum from the plate normal to parallel direction occurs. This is called lateral liquid jetting, which can reach speeds faster than the speed of sound, i.e., supersonic [23]. These high velocities and pressures induce shear and compressive stresses onto the workpiece (e.g., see Ch. 3 for the quasi-static case) resulting in deformation and ultimate material failure and removal. Repeated droplet strikes rapidly erode the surface resulting in a dwelled pocket. When the jet traverses linearly across the workpiece, a trench profile is created. For relatively slow traverse speeds or for thin materials, the droplet stream can penetrate through the material resulting in a complete cut. In this scenario, some of the droplet stream will pass through the material untouched, which can lead to ambiguous interpretation of erosion rate results. Therefore, it is the goal of this chapter to form a trench which is used to assess the erosion characteristics and trench dimensions.

4.2. Experimental setup and methodologies

An image of the experimental WDM device is shown in Figure 4.2(a). A vacuum chamber of approximately 1 m^3 in volume is used to isolate the waterjet and workpiece from atmospheric pressure and is equipped with a window for viewing and photography. The large volume of the chamber mitigates rapid changes in vacuum pressure and provides ample room for excess (impinged) liquid to vacate the impact region. An Edwards GXS 750

vacuum pump, running at full speed, is used during each test. The vacuum pump pulls water vapor and diminutive, atomized droplets out of the chamber, to achieve constant vacuum pressure and steady operating conditions, see section 4.3 for more details. A Hypertherm Hyprecision 60S high-pressure waterjet pump supplies water to a standard PWJ cutting head. Unlike typical AWJ and PWJ systems, the WDM cutting head is fixed, while the workpiece, mounted on a 2-axis traverse system, moves relative to the jet axis, to produce the erosion footprint. Also, unlike traditional waterjets, the WDM jet axis is oriented in the horizontal direction, which is done to accommodate large stand-off-distances in the vacuum chamber. For the high velocities expected in WDM, it is reasoned that the ballistic effects due to gravity are negligible, and therefore, WDM is expected to work in any orientation, with respect to gravity. Figure 4.2(b) shows a cross-sectional, side-view of the experimental setup, drawn in computer aided design (CAD), where the jet axis and SOD are clearly shown. The traverse system is mounted on a sliding rail system for SOD adjustments.



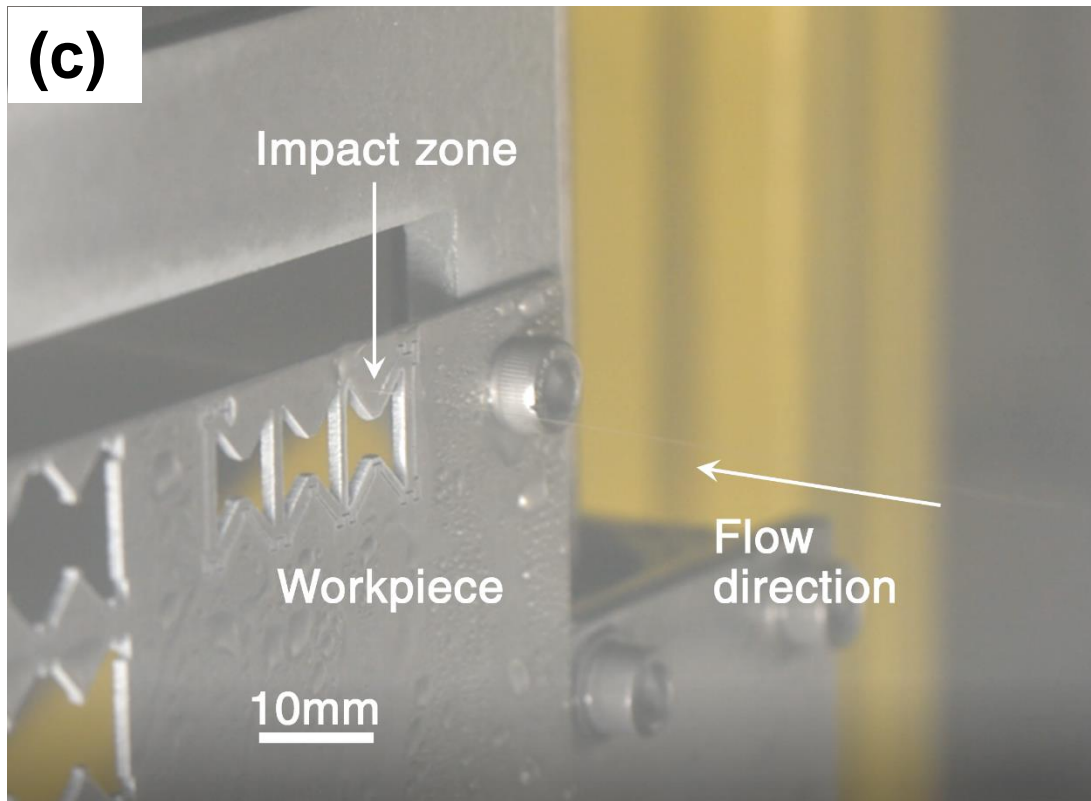


Figure 4.2: (a) Image of experimental setup showing workpiece mounted onto the traverse system inside vacuum chamber. (b) Cross-sectional side view of CAD (computer aided design) model identifying the cutting head, workpiece, and stand-off distance (SOD), and (c) image taken, through viewing window, of WDM performing a through cut of aluminum 6022-T4.

Aside from varying the SOD, the other WDM parameters considered are water pressure P (which controls the jet velocity), orifice diameter d , ambient vacuum pressure P_{vac} , and traverse speed, also referred to as feed rate in industry, denoted by f . Most of these parameters influence the type of waterjet formed, e.g., Rayleigh jet, atomized jet, etc., see section 2.1 for classification of jet regimes. For large Weber number, $We_{gas} \gg 1$, the waterjet atomizes, while for small weber number, $We_{gas} < 0.4$, a Rayleigh jet is created. These two extremes exhibit inherently different droplet streams; the former is wide-spread with a variety of droplet diameters, while the latter is narrow with a series of consistent-sized droplets. The impingement of these two droplet streams result in varied erosion

patterns, and will be discussed in detail in the subsequent sections. To obtain the desired jet-type, process parameters are adjusted to achieve the appropriate Weber number. All jet types are possible given the range of operating conditions; $130 < P < 415 \text{ MPa}$, $50 < d < 760 \mu\text{m}$, $0.1 < P_{vac} < 101 \text{ kPa}$ and $5 < SOD \leq 686 \text{ mm}$. It is expected that high erosion rates are brought about by high impact velocities, therefore, in all of the experiments presented here, the maximum water pressure is used, i.e., $P = 414 \text{ MPa}$. This is customary in industrial AWJ and PWJ cutting, as the goal is to cut material as fast as possible to maximum productivity, therefore the maximum water pressure of the system is almost always used. There are some instances where the water pressure is lowered to pierce brittle materials, such as glass, for shatter prevention. However, after the piercing is complete the pressure is brought back up to its highest setting to perform the remainder of the cut. In present experiments, the WDM vacuum pump is operated at its highest setting to achieve the lowest vacuum pressure possible, which will attenuate aerodynamic drag the most, and, therefore, encourage high velocity droplet impacts to occur. The process parameters which are varied in this study are SOD, jet diameter and feed rate. The influence of these parameters on erosion rate is investigated quantitatively.

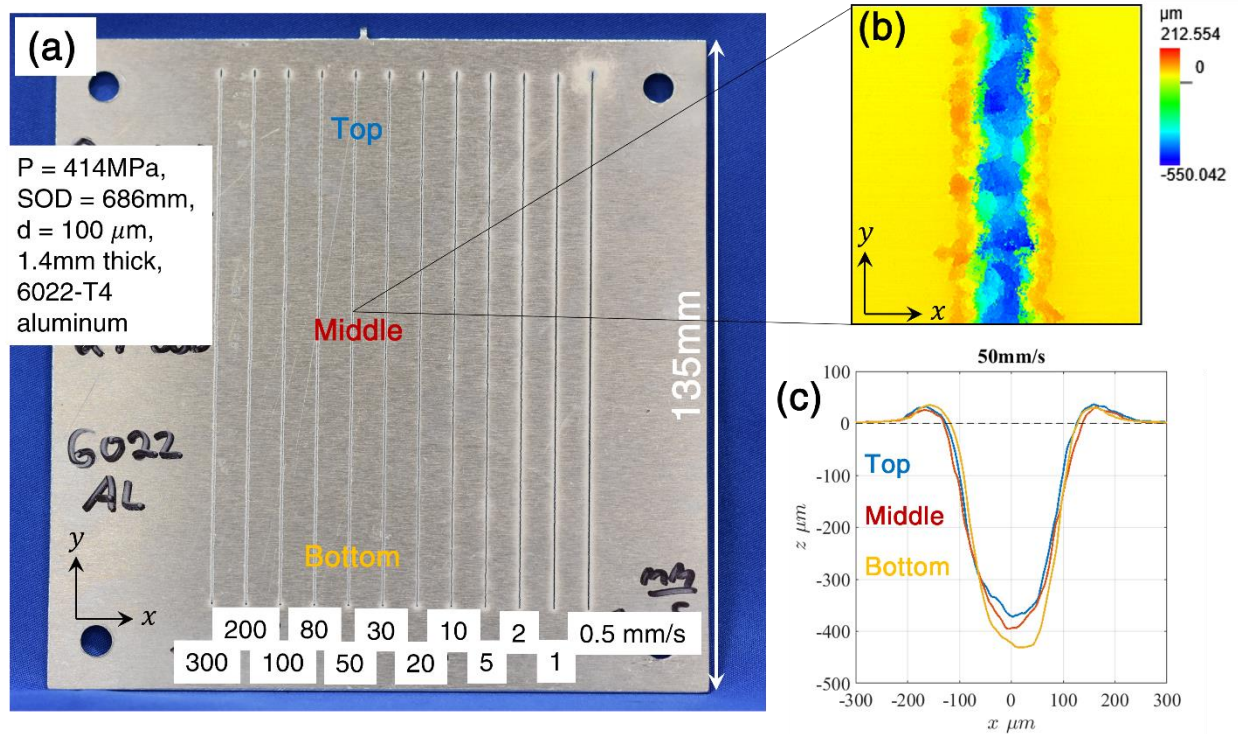


Figure 4.3: (a) Image of typical WDM workpiece with multiple trenches and through-cuts produced, each corresponding to given jet feed rate. (b) Topographic height map of 50 mm/s trench showing raised edge features and depth. (c) Cross-sectional profile of 50 mm/s trench measured at the Top (blue), Middle (red), and Bottom (orange) locations, as indicated by (a).

A common way to assess the erosion rate of a material removal machining operation, e.g., waterjet, plasma, laser, etc., is by measuring its material removal rate (MRR) for a given metal [170-171]. This is the volume of material removed per unit time, in SI units [mm^3/s], and is usually obtained by creating and measuring a trench feature in the material surface by traversing the beam across at constant speed, i.e., feed rate. The depth of the trench is controlled by the feed rate. For slow feed rates, the beam erodes a given location for a longer period of time, resulting in a deeper trench than if a comparatively higher feed rate is used. To study the influence of feed rate on erosion rate, the experiments employ a variety of feed rates. This is done by starting the jet in one location of the workpiece, moving the workpiece at constant velocity for 100 mm, stopping

the jet, and then moving on to create the next trench (at a different feed rate). Figure 4.3(a) shows a typical workpiece test specimen where a variety of trenches and through-cuts are produced. The specimens are 135 x 135 mm² plates with 4 mounting holes in each corner, which are used to fix the workpiece to the traverse system. After machining, topographic measurements of each trench are performed with an Olympus OLS5000 laser-scanning microscope, at the top (blue), middle (red) and bottom (orange) of the trench, as indicated by Figure 4.3(a). A typical topographic height map is shown in Figure 4.3(b), for the 50 mm/s trench, measured at the middle-trench location. For each measurement at the top, middle and bottom, averaged cross-sectional profiles are obtained, and are plotted in Figure 4.3(c). It is apparent that each profile resembles a “U-shape,” with a slight build-up of material on either side of the trench. These profiles are used to determine the average cross-sectional area of removed material A , which is the area bounded by the profile and the top surface of the workpiece, i.e., $z = 0$, black-dashed line. The material removal rate is then calculated by,

$$MRR = Af, \quad (4.2)$$

where f is the feed rate used to produce the trench. The MRR quantifies the rate of erosion for a given material and is used as a metric to gauge the erosive potential of WDM for a specific set of operating conditions, i.e., SOD, d , etc.

4.3. Start up and steady-state operating conditions

Most high-pressure pumps that supply water to an AWJ or PWJ generate heat, which is partially absorbed by the water. Pipe flow turbulence also introduces heat to the supply

water and by the time the water is discharged from the cutting head, its temperature can be as high as 80 °C [172]. The WDM in this study uses the same type of high-pressure pump and similar thick-walled piping (to transport supply water from the pump to the cutting head), as a typical AWJ or PWJ system. Therefore, it is expected that the water temperature entering the vacuum chamber in WDM, is above room temperature. After the water collides with the workpiece, it is expelled onto the chamber walls and floor, where it is permitted to evaporate. Part of this liquid water changes phase into water vapor, since the ambient pressure within the chamber is, at times, lower than the saturation pressure of water. In this evaporation process, the liquid, which changes into water vapor, increases its internal energy. By doing this, the water vapor, in effect, pulls thermal energy out of the chamber walls, thus decreasing the chamber and ambient gas temperature.

Upon WDM start-up, the vacuum pump is turned on and removes the air within the chamber to a pressure of approximately 0.1 kPa. (For reference, standard atmospheric pressure is 101 kPa). During this process, the temperature of the small amount of air left inside the chamber decreases due to the rapid expansion of the gas, but then quickly returns back to room temperature, 20 °C, from heat supplied by the chamber walls and traverse system, which are initially at room temperature. This temperature and pressure remain constant until the jet is turned on and water is introduced into the system. For small orifice diameters, e.g., 100 μm , the water flow rate entering the chamber is approximately 0.5 Liters/min. (Note that a flow meter is installed on the intake side of the waterjet pump to measure volumetric flow rate.) This small amount of water quickly evaporates and allows the chamber temperature to decrease due to evaporative cooling.

It can be reasoned that performing a WDM experiment during these transient conditions will yield ambiguous erosion results.

To identify the chamber pressure and temperature at steady state, two pressure sensors and three thermocouples are installed, each reading approximately the same value, respectively. Figure 4.4(a) shows the pressure and temperature response when the jet is initially turned on at WDM start up. When this occurs, at $t = 0$ min, a rapid increase in pressure takes place, up to 1.8 kPa, i.e., the saturation pressure of water. During this rapid increase, which takes approximately 5 seconds, all of the water entering the chamber is vaporized. Once the saturation pressure is reached, most of the water entering the system remains as a liquid, while the remaining amount of water evaporates and causes a cooling effect. In a way, the WDM system is akin to a refrigeration system, but differs in that the refrigerant runs “open-loop,” and not all of the liquid is removed by the vacuum pump. The excess water simply gathers on the chamber floor, which is removed after a set of experiments are complete.

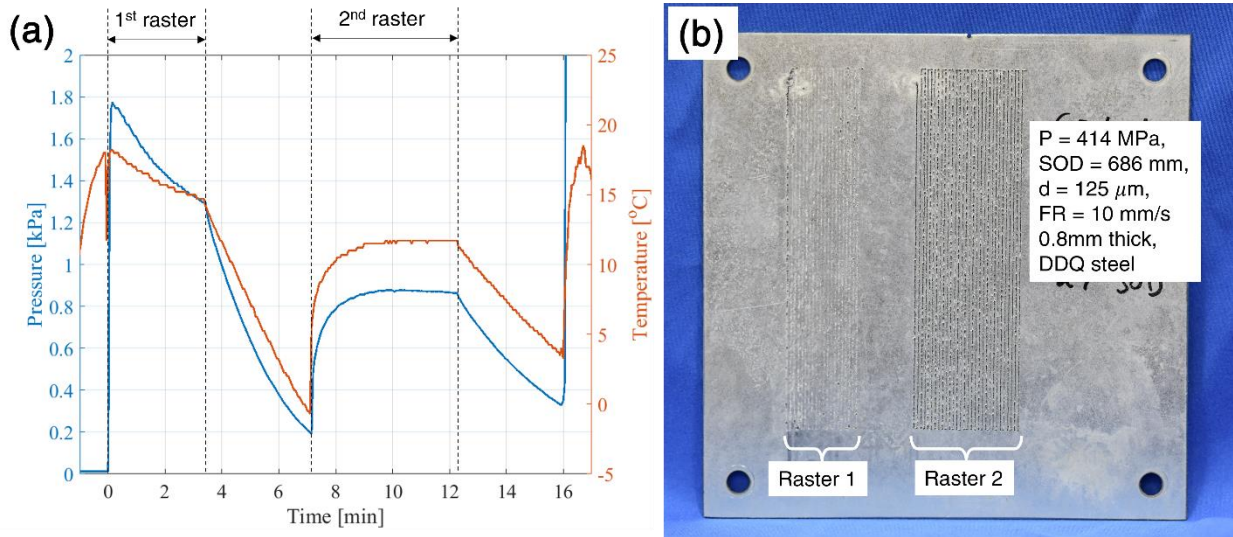


Figure 4.4: WDM start-up conditions; (a) Pressure (blue) and temperature (orange) response during cool-down procedure. Black dashed lines indicate the period when the jet is turned on, corresponding to the raster paths created in (b) Image of sacrificial cool-down workpiece, where the jet traverses up and down, relative to the workpiece, to create a raster path. The state of the ambient gas clearly affects the WDM erosion rate, as indicated by the amount of material removed in each raster.

During the time when the jet is on and the chamber is cooling, Figure 4.4(a), shows that both temperature and pressure continuously decrease, which takes place on an order of minutes. To avoid dwelling a hole in the chamber wall opposite the cutting head, a sacrificial workpiece is used to absorb the erosion due to the jet. This workpiece, shown in Figure 4.4(b), moves up and down in a raster path, where it is apparent that at the beginning, i.e., Raster 1, the material removal is poor. The pressure and temperature during this raster, are decreasing from $0 < t < 3.5$ min. After the raster is complete, the jet is turned off and the pressure and temperature fall at a faster rate, to 0.2 kPa and 0 °C, respectively. Then, a second raster is performed, i.e., Raster 2, where about 2 minutes is required to reach the steady operating pressure and temperature of 0.9 kPa and 12 °C, respectively. This cooling procedure is performed before each set of experiments in order to conduct experiments at (approximately) steady-state conditions. It also should be noted that “steady” pressure and temperature change depending on the

ambient conditions in the facility where WDM is performed, i.e., the UNH John Olson Advanced Manufacturing Center. In WDM tests conducted during the summer months, where the ambient room temperature and humidity are high, a higher steady-state operating temperature and pressure is observed, than if tests are performed during the winter months, when the facility is cold. It is also noted that different steady operating conditions occur for various orifice diameters. As orifice diameter increases, a larger water flow rate is introduced to the chamber, which increases the steady-state pressure and temperature.

The state of the ambient gas clearly leads to different erosion outcomes, according to the workpiece shown in Figure 4.4(b). Here, the Raster 1 exhibits poor material removal, while Raster 2 shows distinct pockets of removed material along the raster lines. This increase in erosion is attributed to the lower gas pressure, which reduces aerodynamic drag and creates a waterjet configuration close to the idealized Rayleigh jet.

4.4 Influence of stand-off distance

In this section, the influence of SOD on erosion characteristics is investigated by creating trenches in a WDM workpiece at four SODs, i.e., $SOD_1 = 45$, $SOD_2 = 229$, $SOD_3 = 457$, and $SOD_4 = 686$ mm. For these tests, 1.2 mm thick stainless steel 316L is used as the workpiece material, with jet parameters set at $P = 414$ MPa, $d = 100$ μ m, which produce a steady operating pressure and temperature of 0.5 kPa and 9 °C, respectively. A new workpiece is used for each test with identical toolpath programs used to create trenches with feed rates of $f = 0.3, 0.5, 1, 2, 3, 5, 10, 20, 30, 50, 80, 100, 200$ and 300 mm/s. Figure 4.5(a-d) shows each workpiece for the range of SODs tested. For short SODs, i.e.,

SOD₁ and SOD₂, no material removal is observed, only thin polish streaks can be discerned, see Figures 4.5(a-b). For the SOD₃ test, material removal is apparent; however, there is no penetration through the backside of this workpiece. The SOD₄ test shows comparatively more removed material, with penetration and a through-cut produced for the 0.3 mm/s case. These results clearly identify enhanced material removal for increasing SOD.

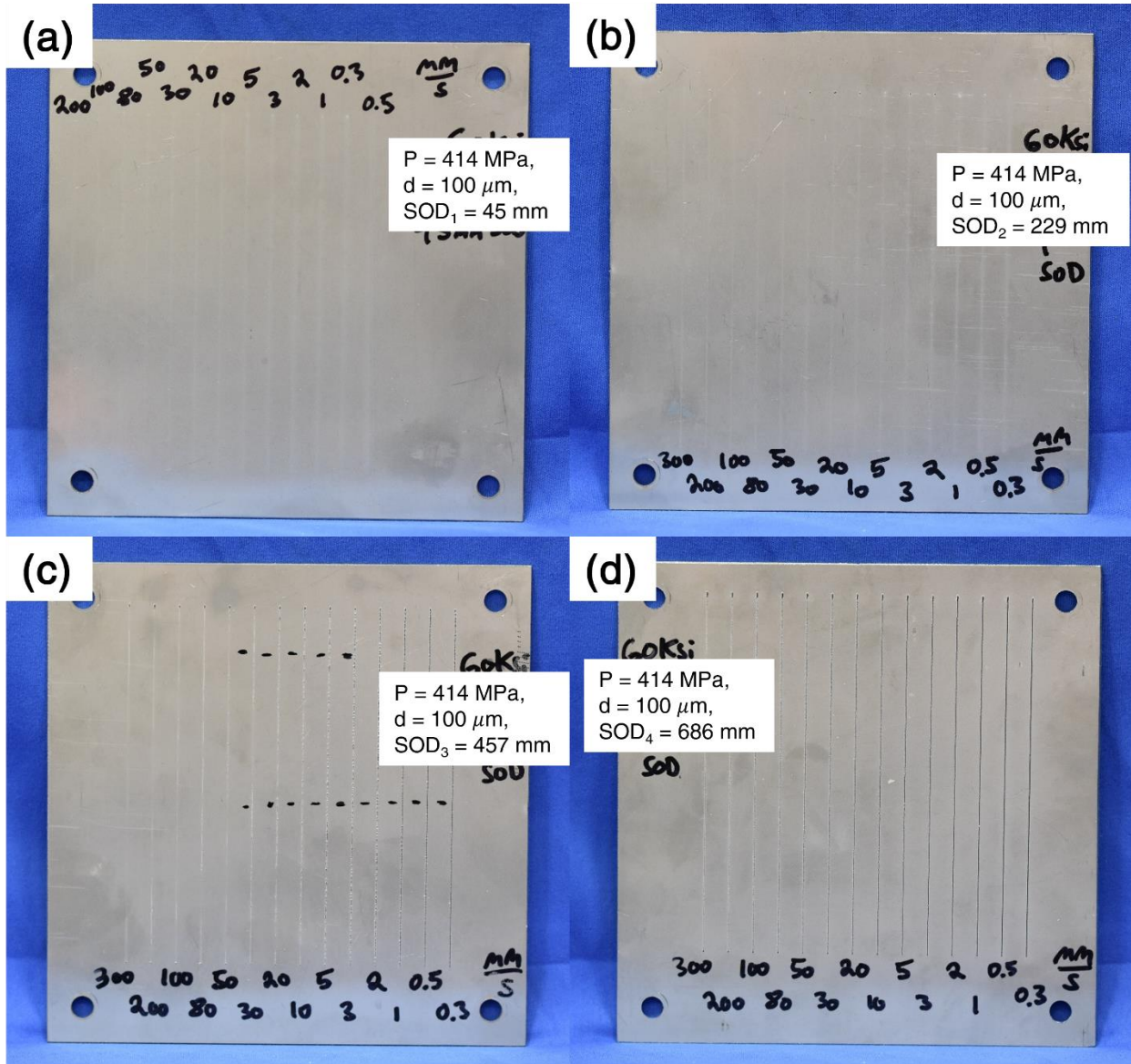


Figure 4.5: Influence of SOD on material removal of stainless steel 316L. WDM test specimens for SODs of (a) $SOD_1 = 45$, (b) $SOD_2 = 229$, (c) $SOD_3 = 457$, and (d) $SOD_4 = 686$ mm. Short SOD, i.e., (a) and (b), do not result in material removal, while material removal is apparent in (c), and to a larger extent in (d). These results clearly identify the advantage of using large SODs in the WDM process.

Trench profile measurements are shown in Figure 4.6. The test conditions of SOD_1 and SOD_2 did not experience any material removal, and therefore, they were not measured with the laser microscope. The middle trench profiles for the SOD_3 (blue) and SOD_4 (orange) test conditions are compared in Figure 4.6, with respect to feed rates of (a) 1,

(b) 3, and (c) 5 mm/s. It is apparent, that for each trench produced, the SOD₄ experiment created deeper trenches than the tests conducted with SOD₃, for each feed rate.

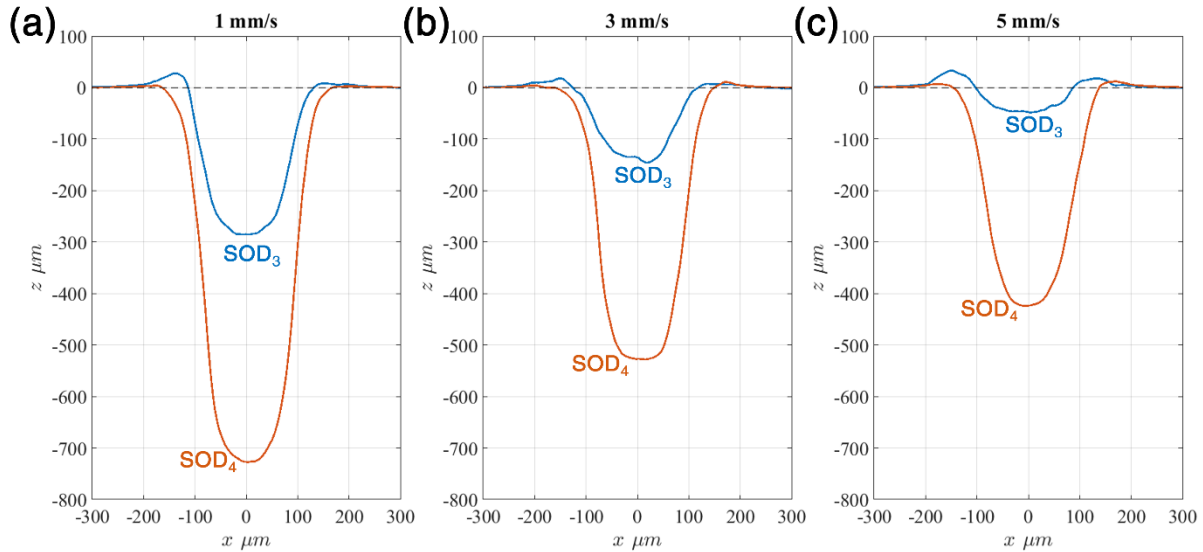


Figure 4.6: Middle trench profiles for the SOD₃ = 457 mm (blue) and SOD₄ = 686 mm (orange) test conditions at feed rates of (a) 1, (b) 3, (c) 5 mm/s. It is apparent that the trenches created with SOD₄ are the largest, revealing that material removal is enhanced for increasing SOD. The trench widths are approximately 200 μm , which is twice the orifice diameter (which is approximately equal the droplet diameter, according to Rayleigh jet theory).

The trench widths are also larger for the SOD₄ experiments, which are approximately 300 μm at the top of the trench and taper downward to $\sim 60 \mu\text{m}$ at the bottom. These narrow widths imply that the jet/droplet stream are weakly affected by aerodynamic distortion and provide evidence that the liquid does not deviate significantly from the jet axis. This is quite remarkable considering the ratio of SOD to jet diameter, i.e., $686/0.1 = 6860$. The trench widths are also comparable to the droplet diameters predicted through Rayleigh jet theory (see section 2.2), where droplet diameters are approximately twice the jet diameter. These results provide strong evidence that the liquid arriving at the workpiece is in either the droplet or wavy jet configuration. It is possible that increased erosion rates occur for $\text{SOD} > 686 \text{ mm}$; however, these distances are not easily testable given the

current machine setup. (Future work will reverse the traverse stage in order to investigate one additional higher SOD.)

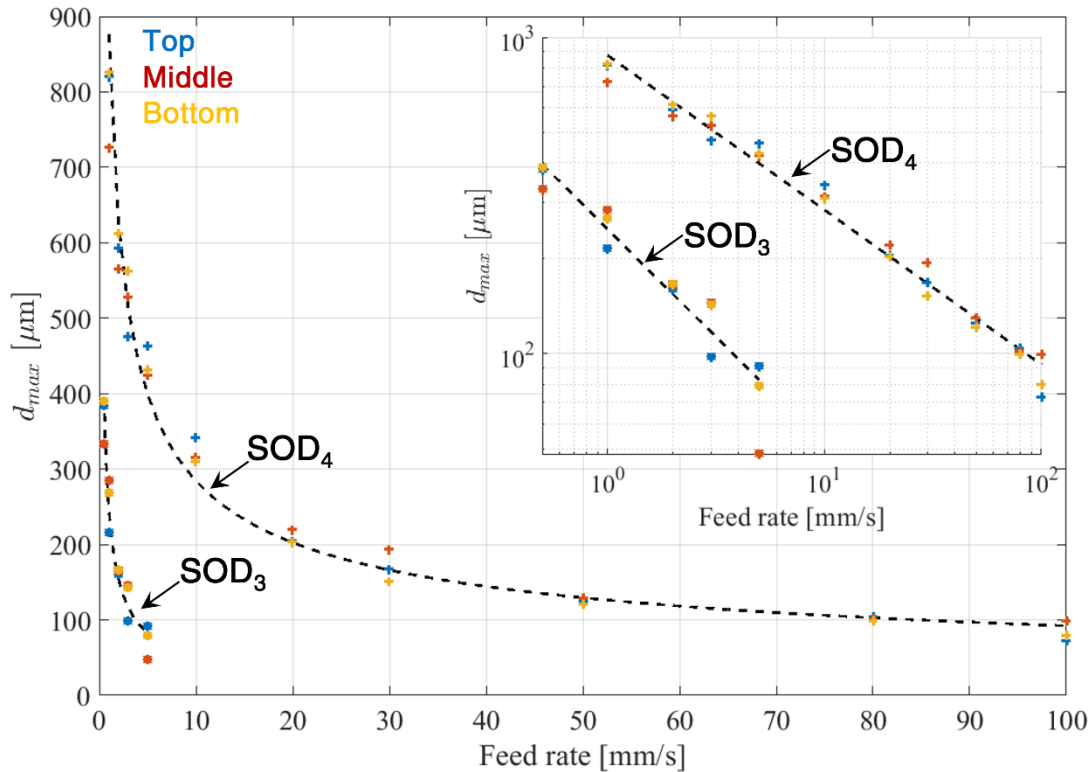


Figure 4.7: Maximum trench depth of the SOD₃ = 457 mm and SOD₄ = 686 mm test conditions plotted with respect to feed rate (inset shows the data plotted on a loglog scale). Colors indicate the location of trench measurements; top (blue), middle (red), and bottom (yellow), while the black dashed lines show a power law approximation. Longer SODs evidently produce deeper trenches.

The maximum depth d_{max} , of each trench is measured and plotted in Figure 4.7. It is clear that tests conducted at SOD₄ produced deeper trenches than tests conducted at SOD₃. The results also identify that higher feed rates correspond to smaller trench depths, and vice versa. This is not surprising, since for slow feed rates, the jet is dwelling in one location for a longer duration, and therefore eroding more material, than that of faster feed rates. When the data is plotted on a logarithmic scale (inset), it becomes apparent that the maximum depth adheres to a power law of the form,

$$d_{max} = aF^n, \quad (4.3)$$

where constants a and n can be determined by least squares. For the SOD₃ and SOD₄ results, these are $a = 247$ s, $n = -0.68$, and $a = 877$ s, $n = -0.49$, respectively, and are plotted in Figure 4.7 as a dashed black line. This power law approximation shows merit as it follows the data trends.

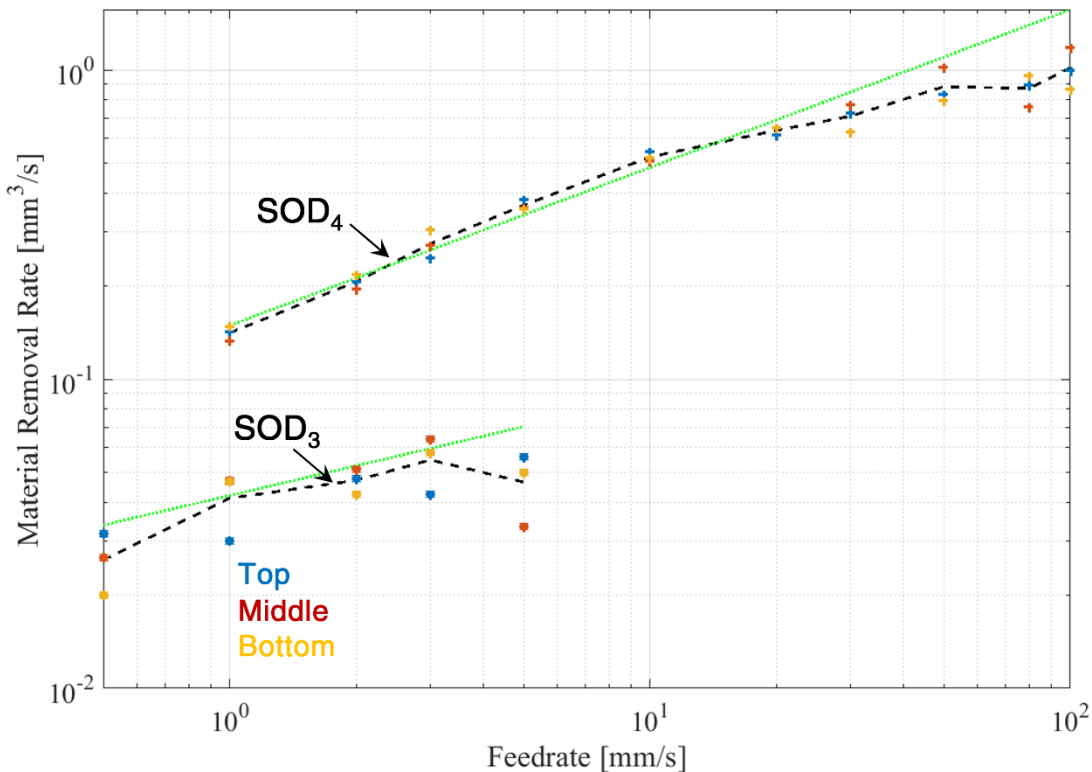


Figure 4.8: Stainless steel 316L material removal rate for tests conducted at SOD₃ = 457 mm and SOD₄ = 686 mm using $d = 100 \mu\text{m}$ orifice and $P = 414 \text{ MPa}$ water pressure. Colors indicate the location of trench measurements; top (blue), middle (red), and bottom (yellow), while the black dashed, and green dotted lines show the average MRR, and MRR model Eq. (4.4), respectively. Longer SODs clearly

Aside from comparing trench depths, another metric of quantifying the removed material is through the MRR. Figure 4.8 shows the MRR for the SOD₃ and SOD₄ test conditions with respect to feed rate. The black dashed lines show each trench's average MRR,

where the general trend is that MRR increases with feed rate. One explanation for this is that, with slow feed rates, a deeper trench is produced, and it is likely that a pool of water forms in the trench, leading to an impediment of the jet/droplet trains' erosive capability. Therefore, for fast feed rates, a smaller trench is produced, and less water is likely to pool, facilitating improved erosion.

Here, it is recognized that a rudimentary erosion model can be made for the test conditions shown in this section. Assuming that the trench width w , remains constant, then the power law depth model, Eq. (4.3), can be multiplied by width to approximate the area of material removed, and thus, when multiplied by feed rate, approximate the material removal rate. The MRR model is given by,

$$MRR = wd_{max}f . \quad (4.4)$$

Using a trench width of $w = 170 \mu\text{m}$, along with the depth models shown in Figure 4.7, the MRR models are calculated and shown in Figure 4.8 as a dotted green line. The models show reasonable agreement up until the highest feed rate, where the model overestimates the data. It is likely that the actual MRR drops off at these higher feed rates, although these trenches are difficult to accurately measure since their depths become close to the surface roughness of the sheet. Nevertheless, the MRR model works well for the mid-to-low-range feed rates. The results shown in this section clearly identify an advantage in using long SODs and suggest that a droplet train (or semi-continuous/wavy jet) produces higher erosion rates than continuous jets.

4.5 Influence of jet diameter

In light of the previous findings, the experiments conducted in this section investigate the influence of jet diameter using the largest SOD of the machine, i.e., $SOD_4 = 686$ mm, as this process parameter produced the highest erosion results. Three orifice diameters are tested, i.e., $d = 100, 180,$ and $250 \mu\text{m}$, on 1.2 mm thick stainless steel 316L and 1.4 mm thick aluminum 6022-T4. The $d = 100 \mu\text{m}$ test on stainless is essentially a repeat of the experiment shown in Figure 4.5(d), where good experimental repeatability is observed. The tests using the $d = 180 \mu\text{m}$, and $250 \mu\text{m}$ orifices conducted on the stainless steel are shown in Figure 4.9(a) and (b), respectively, while similar tests conducted on the aluminum are shown in Figure 4.9(c) and (d), respectively. It is apparent that the $d = 180 \mu\text{m}$, and $250 \mu\text{m}$ diameter orifices produced wider trenches than the $d = 100 \mu\text{m}$, see Figure 4.5. It is also clear that through-cuts were produced for some of the low feed rate cases, especially the 5 mm/s test in Figure 4.9(d), where a 4 mm width kerf was produced. The edges of this kerf are heavily eroded, feature a significant taper, and are of high surface roughness. It is evident that tests conducted with these large orifice diameters, i.e., $d > 100 \mu\text{m}$, do not result in precise and narrow kerfs.

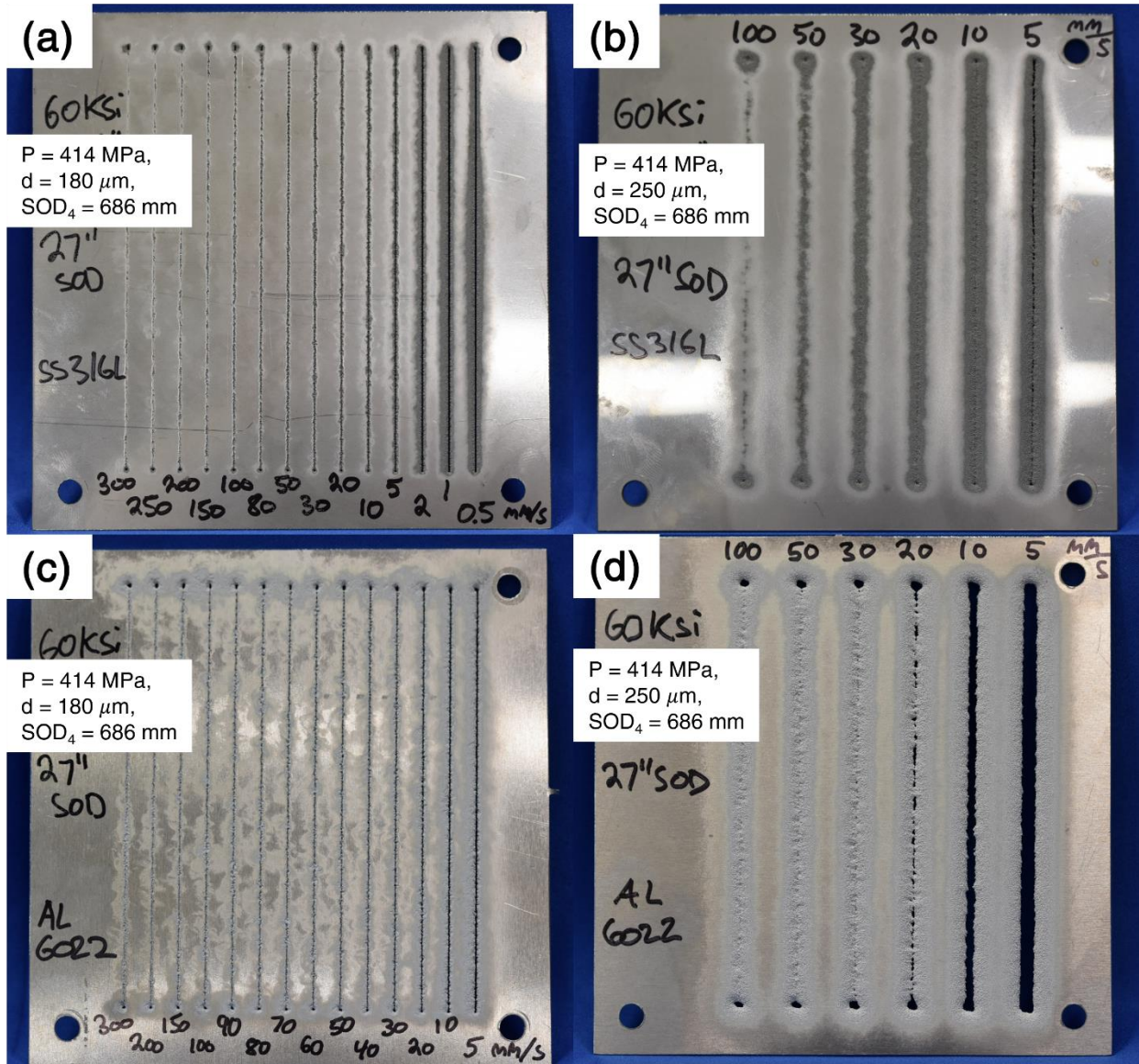


Figure 4.9: Influence of orifice diameter. Stainless steel 316L tests conducted with an (a) $d = 180 \mu\text{m}$, and (b) $d = 250 \mu\text{m}$ diameter orifice. Aluminum 6022-T4 tests conducted with a (c) $d = 180 \mu\text{m}$, and (d) $d = 250 \mu\text{m}$ diameter orifice. These tests resulted in wide trenches with high surface roughness.

Trench profiles, using the various orifice diameters, for the 10 mm/s feed rate on the stainless steel, and the 50 mm/s feed rate on the aluminum are shown in Figures 4.10(a) and (b), respectively. For increasing orifice diameter, trench widths become larger, which indicate that the configuration of the jet is approaching the atomized regime. Here, a spray of droplets are most likely impinging the surface rather than a Rayleigh-type jet. Trenches

also become larger in cross-sectional area with increasing d , which can be attributed to the greater amount of momentum transmitted to the workpiece (since as orifice diameter increases so does the water flow rate).

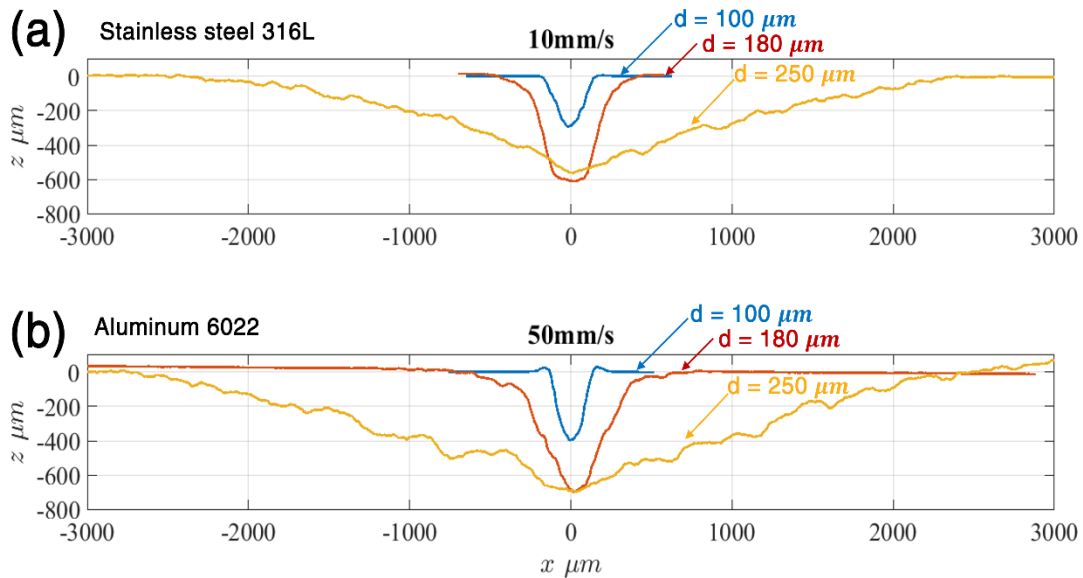


Figure 4.10: Middle trench profiles for the (a) 10 mm/s trench on stainless steel 316L and (b) 50 mm/s trench on aluminum 6022, using $d = 100 \mu\text{m}$ (blue), $d = 180 \mu\text{m}$ (red), and $d = 250 \mu\text{m}$ (orange) diameter orifices. Trench width increases nonlinearly with d , indicating that the jet configuration approaches the atomized regime.

The material removal rates for these tests is plotted in Figure 4.11 for (a) SS 316L, and for (b) AA6022-T4. Larger orifice diameters exhibit higher MRRs, for most of the feed rate ranges tested. The MRR for the aluminum is higher than for the stainless steel, which is expected when considering that the yield and fracture strength of stainless steel is higher than for aluminum. Hence, the stainless steel can tolerate droplet strikes and resist erosion better than the aluminum. For feed rates greater than 100 mm/s, the stainless steel MRRs have considerable variation, which is due to trench inconsistency. The high feed rate trenches shown in Figure 4.9, visibly show regions of high material removal and

regions of comparatively low material removal along the trench direction. These variations are reflected in the widely varying MRRs of Figure 4.11(a), above $f \geq 100$ mm/s.

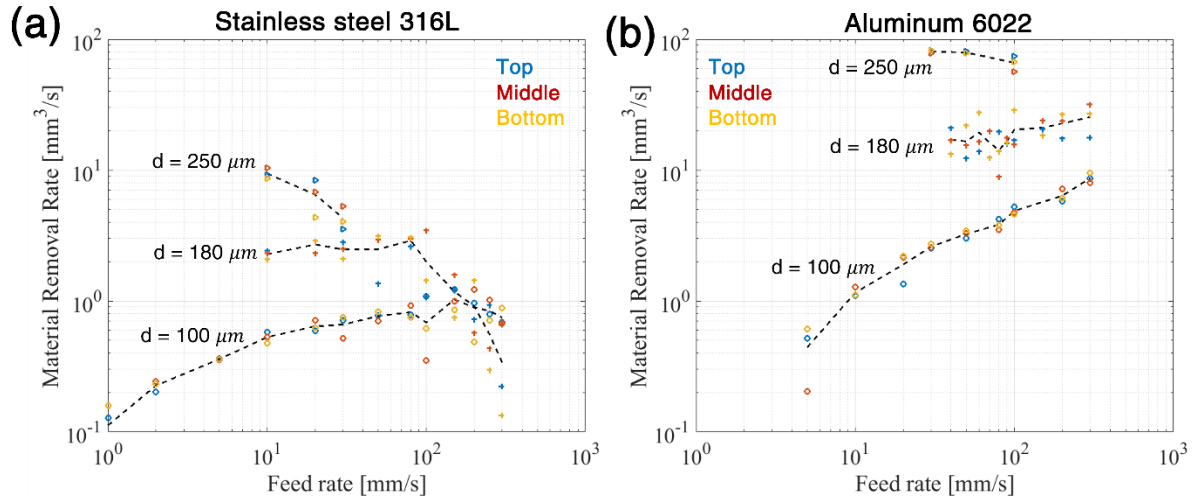


Figure 4.11: Influence of feed rate and orifice diameter on material removal rate for (a) stainless steel 316L, and (b) aluminum 6022. Colors indicate the location of trench measurements; top (blue), middle (red), and bottom (yellow), while the symbols indicate orifice diameter; $d = 100 \mu\text{m}$ (circle), $d = 180 \mu\text{m}$ (plus), and $d = 250 \mu\text{m}$ (triangle). MRRs for aluminum are greater since the material is more susceptible to erosion than stainless steel.

The orifice diameters of $d = 180 \mu\text{m}$ and $250 \mu\text{m}$, were able to cut through the stainless steel and aluminum sheets, but due to the wide kerf widths, poor edge quality, and taper, these large orifice diameters (and associated process parameters) are likely unsuitable for precise through-cutting. It is therefore recommended that orifice diameters for precision through-cutting be approximately $d = 100 \mu\text{m}$. The observed erosion patterns and trench widths, in this section, demonstrate that the jet-type can be controlled for a desired erosion outcome according to orifice diameter.

One may wonder if the Weber number, i.e., $We_{gas} = \rho_{gas} d v^2 / \sigma$, can be used to predict the WDM jet configuration, i.e., Rayleigh versus atomized jet. It is tempting to use the ideal gas law to determine gas density, especially since the ideal gas law becomes a

better approximation for decreasing density; however, the substance surrounding the WDM jet is a mixture of low-density gas and diminutive “mist” droplets. The density of this multiphase flow is difficult to know for certain. Furthermore, the jet velocity is also hard to determine with confidence. The Bernoulli equation is tempting to use; however, with the smallest orifice, i.e., $d = 100 \mu\text{m}$, viscous effects may be large at this scale, and the flow could be fully developed upon orifice exit. Note that the orifice geometry was inquired from the manufacturer; however, details were not given as they are proprietary. Nevertheless, the erosion footprints can be used to gauge jet configuration.

4.6 Comparison with conventional pure waterjet cutting

A stainless steel 316L workpiece (same material used in the tests of sections 4.4 and 4.5), was tested using a PWJ with a pressure $P = 414 \text{ MPa}$ (measured approximately halfway between the high pressure pump and experimental setup), and orifice diameter of $d = 100 \mu\text{m}$. This experiment was conducted in the WDM experimental setup at the $\text{SOD}_1 = 45 \text{ mm}$ location, but without the vacuum pump running and the chamber ports open to atmospheric pressure, and at a feed rate of 0.3 mm/s . This is essentially the test of Figure 4.5(a) but conducted in atmospheric conditions. Figure 4.12(a) shows the PWJ results, with WDM results in (b), which is the 0.3 mm/s through cut of the test shown in Figure 4.5(d). The PWJ created a trench width of approximately 0.5 mm , while the WDM created a through-cut of width 0.3 mm . Here, the advantage of WDM over PWJ is clear. For equivalent conditions, WDM outperformed PWJ by creating a through-cut. It is interesting to note that the PWJ produced a trench at this location, while at the same SOD location, WDM did not produce any discernible material removal, see Figure 4.5(a). It is

possible that the PWJ segmented into an atomized jet, resulting in a swath of droplet impacts capable of material erosion, while the WDM test, at this SOD location, was probably a continuous stream impact and unable to induce erosion.

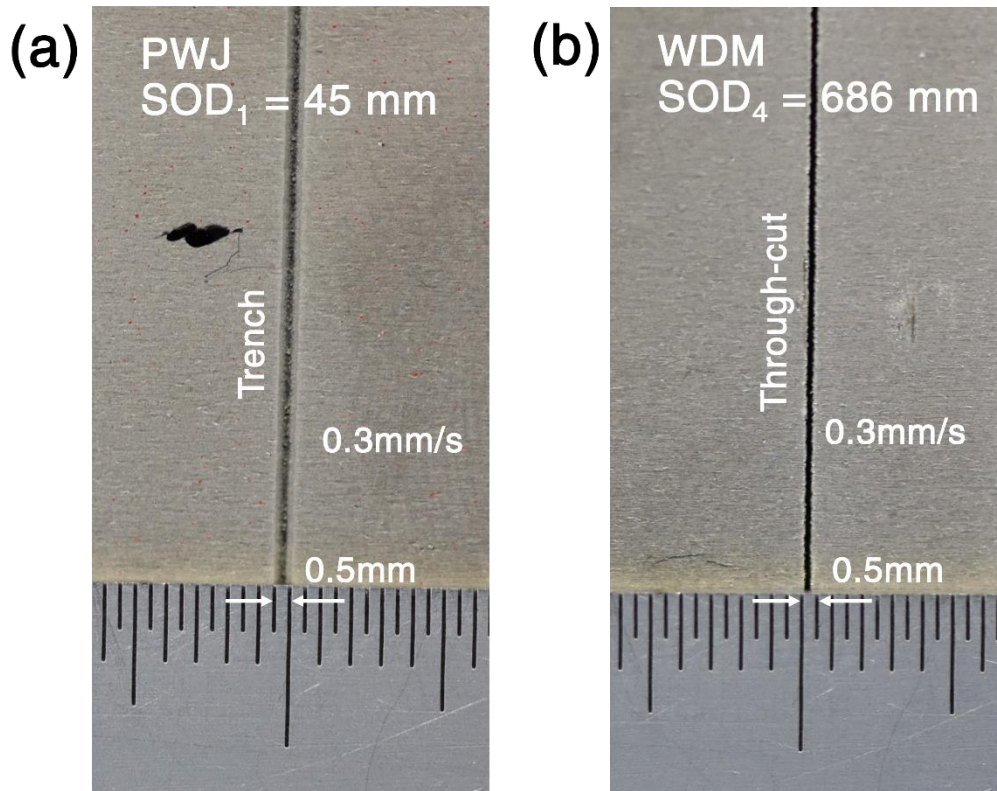


Figure 4.12: Comparison of (a) PWJ and (b) WDM on stainless steel 316L, for identical flow conditions; $P = 414 \text{ MPa}$, $d = 100 \mu\text{m}$, and $F = 0.3 \text{ mm/s}$. The PWJ only created a trench, while WDM produced a through cut, identifying a distinct advantage of using WDM over PWJ.

5. CUTTING CARBON FIBER WITH AWJ VS. WDM

(Text for this chapter is taken from an accepted but yet to be published article in *Manufacturing Letters* (2022) titled “Advantages of water droplet machining over abrasive waterjet cutting of carbon fiber reinforced polymer.” My contributions to this work were all experiments and analysis, except for the CMM measurements in section 5.2.4.)

Carbon fiber reinforced polymer (CFRP) composites are heterogeneous and anisotropic materials, which exhibit high stiffness, excellent corrosion-resistance, and high strength-to-weight ratios, and thus offer superior functional performance over conventional materials, such as steel [173]. These advantageous properties have led to widespread manufacturing and adoption of CFRP in a variety of industries including aerospace, automotive, marine, medical, sporting equipment, and wind energy [174]. During CFRP manufacturing, the composite is typically molded into the desired part geometry; however, subsequent machining operations, such as trimming, tapering, and hole drilling, are often required to bring the part into tolerance and to create features that would not be possible with the layup process alone. Creating these features with conventional tooling, such as a drill or end-mill, often result in excessive tool-wear, high-heat generation, composite delamination, and dust emission [174, 175]. Delamination and heat-induced resin degradation compromise CFRP part quality, which is particularly concerning for aircraft manufacturers as a single, large aircraft contains over a million mounting holes [174, 175, 176]. Delamination-related failures of aircraft components have led to rejection rates as high as 60% [175]. Despite these manufacturing challenges, studies have been conducted in an attempt to identify machining parameters, which mitigate delamination, increase the machinability of CFRP, and extend tool life by the use of slow feed rates and

spindle speeds, specialized tool geometries and coatings, and minimized lubricant levels [177-185]. Even with these methodologies, the risk of delamination and part degradation persists, requiring consistent quality monitoring, which adds to the already high tooling and machining costs of CFRP production. Therefore, alternative manufacturing techniques are sought, which produce high-quality edge features at low production costs.

Laser beam cutting has been used for CFRP hole drilling and edge routing, however, a heat affected zone is generated which has limited its widespread use in cutting CFRPs [174, 175, 186-188]. Abrasive waterjet cutting has been used as another alternative CFRP cutting process, but this technique often leads to delamination of the composite material, especially around pierce locations. To mitigate delamination, through-holes can be pre-drilled in the composite to create a starting position for the AWJ; however, the drilling process is subject to pull-up and push-out delamination [189]. When piercing CFRPs with an AWJ, the mechanism responsible for delamination is the hydrodynamic stagnation pressure created by a water-wedge action [189, 190]. The water, following the path of least resistance, will separate the layers if the pressure exceeds the tensile strength of the bonding layer. Furthermore, abrasive particles can become embedded into interlaminar cracks, requiring additional operations to remove the residual particles [191]. Despite these adverse effects of piercing and cutting CFRP with AWJ, there has been success in suppressing delamination by starting the pierce with a close to zero water pressure and then slowly increasing water pressure until the pierce is complete [192]. Varying the water pressure (and therefore, water flow rate) consequently requires fine tuning and timing of the abrasive delivery system. Various AWJ piercing techniques have been developed and are still active areas of investigation [189-195]. According to the

literature and industrial correspondents, a method, which cuts CFRP with satisfactory results and with low cost of production, is still lacking. It is therefore worthwhile to explore water droplet machining as an alternative CFRP cutting technique.

Owing to the absence of abrasives and the lack of heat-affect-zone in WDM, it is worth investigating whether this manufacturing process can cut CFRPs with reasonable cut-edge characteristics and without the tendency for delamination. Therefore, the aim of this chapter is to explore the CFRP cutting performance of WDM on industry relevant CFRP sheets and compare the results to similar tests conducted with an AWJ. Section 5.1 outlines the experimental methods used in cutting the CFRP specimens with WDM and AWJ. Section 5.2 discusses the results of both cutting methods and evaluates the cut characteristics based on surface roughness, the presence of delamination, and the geometric accuracy of the intended part. Section 5.3 highlights the main discoveries while proposing future work in WDM cutting of CFRPs. It is also worth mentioning that an environmental and economic comparison between AWJ and WDM has been performed, where AWJ was found to be more economical and sustainable [196].

5.1 Experimental methods

To compare the effectiveness of cutting a CFRP laminate with WDM and with an AWJ, a variety of basic shapes were cut out of a CFRP workpiece. The CFRP laminate used in these tests was produced by autoclave-molding of 22 woven graphite/epoxy plies with a layup configuration of $[90, (0^\circ/90^\circ)_5]_s$. The autoclave pressure was 516.75 kPa and the cure time was 60 min at 127 °C. The final cured laminate thickness was 5.5 ± 0.02 mm. The cut-out shapes were a series of circles ranging from 1 mm to 32 mm, an equilateral

triangle of side length 30 mm, and a raster path of side length 50 mm. The AWJ used was a Wardjet E-1515 with a Hypertherm Hyprecision 60s intensifier pump. This is also the same water pump used in WDM experiments, which produces a water pressure of $P = 414$ MPa. The abrasive cutting head uses a $406 \mu\text{m}$ diameter orifice, a 1.016 mm diameter nozzle, an abrasive flow rate of 476 gram/minute, an 80-mesh abrasive, and a stand-off distance of 3 mm. According to the Hypertherm cutting calculator, 5.5 mm thick CFRP should be cut at a feed rate of 26.7 mm/s for excellent edge quality [197]. Faster feed rates can also be used to cut the CFRP but at reduced edge quality.

For these experiments a 26.7 mm/s feed rate was chosen so that the highest quality edge would be produced. For stationary piercing, which is the piercing method used in these experiments, the Hypertherm cutting calculator suggests using low pressure, 103 MPa, for 1 second, then increasing the pressure to 414 MPa to perform the remainder of the cut. The piercing procedure turns the jet on at low pressure and then 0.2 seconds later the abrasive flow starts, which was found to be the most successful timing for mitigating delamination [192]. One second later the pump switches to high pressure, which takes 3.5 seconds to achieve, and then proceeds to move along the tool path. This method was used in all AWJ pierces. To mitigate delamination around the shape edges, all pierces start in the middle of each circle and triangle. Then the jet traverses up to the shape edge and finally moves around the outline. This positions the pierces as far away from the feature edges as possible.

For the WDM experiments a water pressure of $P = 414$ MPa was used for all piercing and cutting procedures. An orifice diameter of $P = 100 \mu\text{m}$ was used with a stand-off distance of $\text{SOD}_4 = 686$ mm. The pressure and temperature inside the chamber during cutting

were 0.7 kPa and 3 °C, respectively. Note that WDM operates close to the triple point of water, which is the temperature and pressure at which water exists in equilibrium in its liquid, solid, and gaseous states. All pierces are dwelled for 1 second and then the jet moves relative to the workpiece. The feed rate used was 1 mm/s, although 2 mm/s was also explored as detailed in Section 5.2.2.

5.2 Results and discussion

5.2.1 Abrasive waterjet cutting of CFRP

Figure 5.1(a) shows the CFRP sample cut using AWJ. It is apparent that the process created the desired shapes but with moderate delamination in some regions. Around each circle the upper surface of the sample is raised while cracks are visible on the inside edges. The smallest hole, which is roughly 2 mm in diameter, is a pierce only, i.e., the jet does not traverse the circumference. The top-edge of the sample closest to this hole shows edge delamination and cracking as shown in Figure 5.1(b), with the location of the side view indicated in Figure 5.1(a). This edge is about 30 mm away from the hole location, which indicates that the delamination phenomena can spread far away from pierce locations. A similar feature exists on the bottom edge of the sample closest to the triangle, see Figure 5.1(c), with the location of the side view again indicated in Figure 5.1(a). The inside of the shapes, which contain the pierce, all show severe delamination. Figure 5.1(d) shows a side of the cut out triangle with significant multi-layer delamination. It is not surprising that considerable delamination occurs near pierce locations as this is where the water wedge action occurs [189]. For the raster path, the pierce starts in the upper left corner and has a 5 mm on-center spacing between the lines. The raised surface

in this region indicates that delamination occurred here; however, the remainder of the raster path appears to have excellent cut characteristics. This is the only region where delamination did not occur (based on visual observation). If an AWJ starts in a through-hole or off the part, then delamination can be avoided [192]. However, even with the low-pressure pierce option used in these experiments, delamination occurred at all pierce locations.

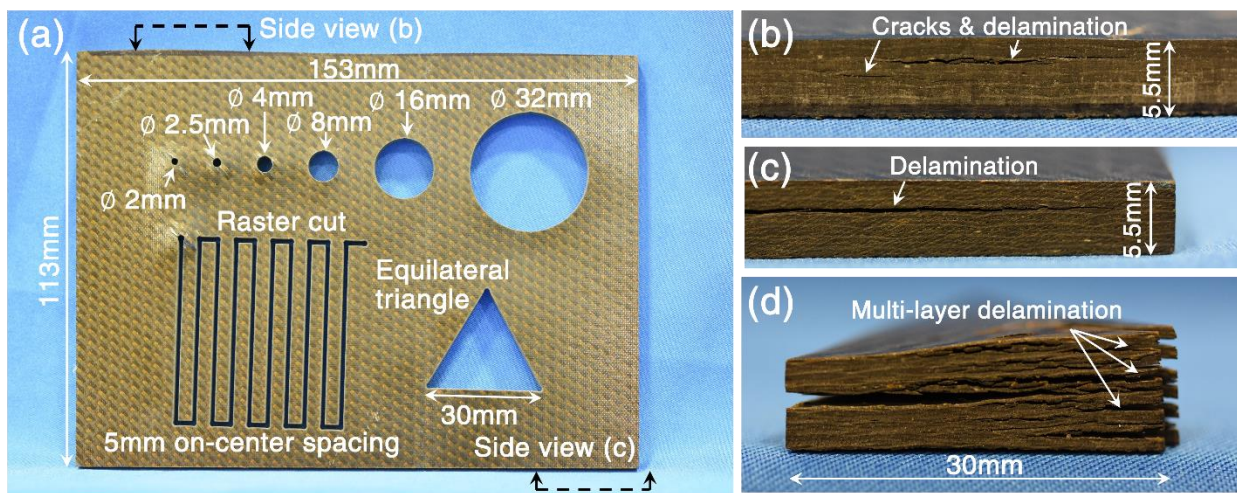


Figure 5.1: (a) Top view of various shapes cut in a CFRP sheet with AWJ, (b) side view of top-edge, (c) side view of bottom-edge, and (d) side view of cut out triangle showing delamination features.

5.2.2 Water droplet machining of CFRP

For the WDM experiments, a similar tool path was made to create the same shapes as in the AWJ experiments, i.e., a series of circles, a triangle, and a raster path. Figure 5.2(a) shows the CFRP sample cut by WDM. Visual observation of WDM cut edges show an absence of delamination for all shapes. Note that the four holes in the corners of the sample were hand drilled for fixturing the sample onto the WDM system. The other holes, ranging from 1 mm to 32 mm in diameter, show good cut quality. All of the pierce locations

feature a small crater-like region of hollowed-out material, roughly 1 mm in size. In Figure 5.2(a), this is apparent on the 1 mm diameter hole, which is slightly elliptical, and also on the start of the raster (top left). The cut-out circles and triangle also feature this crater effect at the pierce location (not shown in Figure 5.2). Figure 5.2(b) shows a zoomed-in image of the raster cut. These cuts are separated by 2 mm on-center spacing between the lines, which would not have been possible with the AWJ since this jet's kerf width is slightly greater than 1 mm. Figure 5.2(b) also elucidates the small kerf widths, i.e., 300 μm , achievable with WDM. The consistency of this diminutive kerf is remarkable considering how far away the orifice is from the sample, i.e., stand-off distance to kerf ratio of 2287. This is achievable because of the low ambient pressure and its negligible effects on the waterjet and droplet train, i.e., so that deviation from the jet axis does not occur.

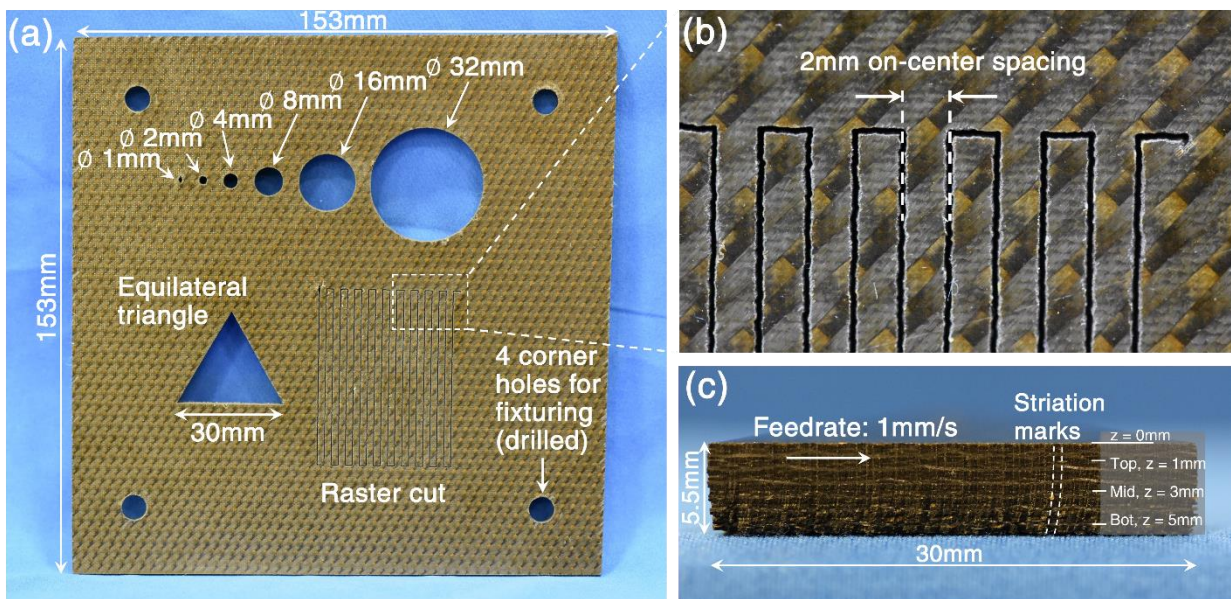


Figure 5.2: (a) Top view of various shapes cut in a CFRP sheet with WDM, (b) zoom-in view of raster kerf, and (c) side view of bottom-edge of triangle.

The circles and triangle cuts were performed with a feed rate of 1 mm/s, while the raster

was cut with a feed rate of 2 mm/s. This feed rate was slightly too fast as the CFRP is still attached in some areas on the bottom-side of the cut. This is apparent if the sample is held up to a light and visually inspected by looking through the cuts. Figure 5.2(c) shows the bottom edge of the triangle cut-out. Note that delamination and cracks are not visually present. This is in contrast to the AWJ cut triangle edge in Figure 5.1(d), which showed significant delamination. On the left and right bottom corners of the triangle in Figure 5.2(c) the laminate appears to be chipped, where individual layers can be identified; however, these chips did not seem to propagate into the material as a delamination. Figure 5.2(c) also shows striation marks on the cut edge, which is a similar feature to an AWJ cut edge on metal [198].

Another unique feature of WDM is its ability to create tight corners of approximately 150 μm radii. The AWJ cut triangle corners, in Figure 5.1(a), are notably different compared to the triangle corners cut by WDM in Figure 5.2(a). This feature of WDM allows for fabrication of small feature sizes in CFRP and with less risk of delamination than with AWJ. Although WDM can produce tiny kerfs and does not feature delamination, it is considerably slower at cutting CFRP than the AWJ, which is approximately 27 times faster. However, note that the AWJ technology has been heavily studied and optimized, while WDM is in its infant stages of development and so has the potential for growth and enhancement. One question that remains is the tendency of WDM to suppress delamination. Due to the discrete nature of WDM, it is possible that the lateral stagnation pressure that the material experiences is periodic and at a high enough frequency so that delamination is suppressed, although more research is required to validate this notion.

5.2.3 Surface roughness of WDM cut edges on CFRP

Surface roughness measurements were conducted on the WDM cut-out triangle of Figure 5.2(c), using an Olympus OLS5000 3D laser microscope. Figure 5.3(a) shows a detailed microscope image of the WDM cut surface, where individual fiber layers can be identified. From this image, delamination and cracks are absent suggesting that the WDM process does not induce delamination of CFRP. Owing to the cold operating temperatures of WDM it is surmised that WDM does not cause heat-induced resin degradation either. Figure 5.3(b) shows a 5.5 x 9.5 mm² topographic height map of the cut surface, revealing ridges of raised composite material, as shown by the red-colored features. Note that in Figure 5.3(b), green is taken as the mean surface height of 0 μm . The raised surface features, which are analogous to the striation marks observed in AWJ cutting of metals, have heights of approximately 300 to 400 μm . The ridges increase in height from the top-side of the CFRP specimen towards the bottom-side where they are at a maximum. These ridges increase the roughness of the cut edge, and for the surface shown in Figure 5.3(b), the mean surface area roughness is $S_a = 56.1 \mu\text{m}$. While individual fiber layers are easily identified in Figure 5.3(a), the same cannot be said for Figure 5.3(b), as the morphology of the WDM cut surface does not expose layers and is nearly homogeneous in the through-thickness direction. Due to the presence of cracks and delamination in the AWJ-cut specimen, edge roughness measurements were not performed.

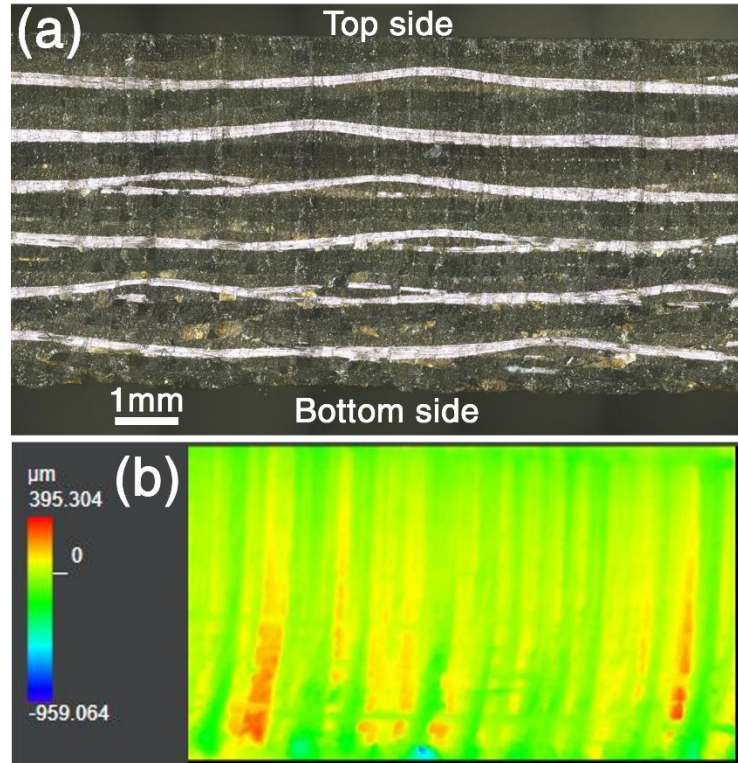


Figure 5.3: (a) Microscope image of WDM triangle cut edge in CFRP, and (b) topographic height-map of surface shown in (a).

5.2.4 Dimensional accuracy of AWJ and WDM cuts

The dimensional accuracy of the hole and triangle features cut by AWJ and WDM were performed on a Mitutoyo MACH-806 coordinate measurement machine (CMM) by Ahmad Sadek of the Aerospace Manufacturing Technologies Center, National Research Council, Montreal, QC, Canada. The hole diameter and circularity errors of the \varnothing 32 mm, \varnothing 16 mm, \varnothing 8 mm and \varnothing 4 mm holes were measured using a 2 mm diameter probe. For each hole, measurements were performed at the top (Top), middle (Mid) and bottom (Bot) planes located at 'z' depths of 1 mm, 3 mm, and 5 mm, respectively, from the uppermost plane ($z = 0$ mm) of the CFRP plate, as shown in Figure 5.2(c). Ten measurement points were probed to measure the diameter and circularity of each circular hole feature at each

plane. Measurements of the $\text{\O}2.5$ mm, $\text{\O}2$ mm, and $\text{\O}1$ mm holes were not possible due to the limitation of the probe size. Figure 5.4(a) compares the measured mean hole diameter deviation from the nominal hole diameter at the top, middle and bottom planes using the WDM and AWJ processes. The figure shows that both processes produced oversized hole diameters that ranged between (+0.07 mm to +0.12 mm) for the WDM and (+0.02 mm to +0.23 mm) for the AWJ. In a case where a static maximum tolerance limit of +0.10 mm was considered, the acceptance rate (within tolerance) for the WDM holes (75%) was significantly higher than that for the AWJ (25%). This could be attributed to the excessive material removal in AWJ caused by the abrasive particles in the cutting zone. The figure also shows, for all the AWJ holes, a gradual reduction of the hole size from the top to the bottom planes indicating a tapered hole surface of an average 0.86° angle. The WDM holes did not experience such effect and were found to be more cylindrical. Reducing the taper angle in AWJ may require a higher jet pressure and a reduced standoff distance to increase the cutting efficiency near the bottom [199]. Taper reduction may also be possible by changing the feed rate.

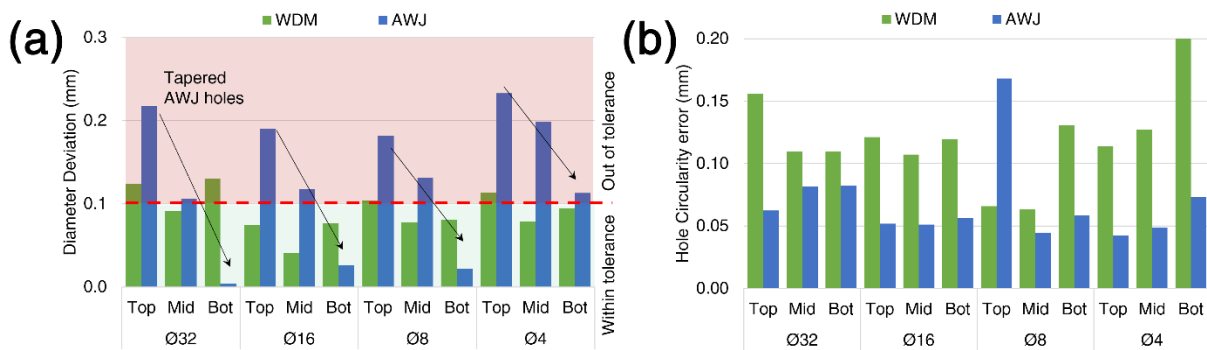


Figure 5.4: (a) Hole diameter deviation measured at top, middle, and bottom level planes for the WDM and AWJ process. (b) Hole circularity errors measured at top, middle, and bottom level planes for the WDM and AWJ process.

On the other hand, Figure 5.4(b) shows around two-fold higher circularity errors for the WDM compared to the AWJ machined holes at the top, middle and bottom planes. Circularity error is the radial distance between the minimum circumscribing circle and the maximum inscribing circle of the measured surface points. The lower circularity error in the AWJ-cut holes could be due to the ability of the jet and abrasive particles to facilitate sharper and smoother edges compared to the WDM jet. Alternatively, since the x-y stages for the WDM and AWJ processes are different, this could affect circularity of the features created.

The average straightness and perpendicularity errors of the equilateral triangle wall surfaces (along the depth of the plate) were computed based on three measurements per surface. The perpendicularity of the triangle wall surfaces was measured with respect to the CMM probed uppermost plane of the CFRP plate ($z = 0$ in Figure 5.2(c)). The average straightness error of the three triangle surfaces along the depth of the plate were found to be 0.052 mm and 0.021 mm for the WDM and the AWJ processes, respectively. This agrees with the higher circularity errors observed in the case of circular holes cut via WDM compared to AWJ. In terms of the average perpendicularity errors of the triangle wall surfaces with respect to the uppermost CFRP plate surface reference, the WDM showed a relatively lower error (0.078 mm) compared to that of the AWJ (0.110 mm), which agrees with the tapered hole findings. Table 4 summarizes the test conditions and dimensional measurement results of cutting various diameter holes in CFRP with both waterjet machines. WDM showed a smaller average diameter deviation (Avg. dia. dev.) and smaller taper angle than AWJ; however, WDM had a higher average circularity error (Avg. circ. error) than AWJ.

Table 4: Test conditions and results of hole cutting

Tool	Orifice (μm)	Feed rate (mm/s)	Avg. dia. dev. (mm)	Avg. taper ($^{\circ}$)	Avg. circ. error (mm)
AWJ	406	26.7	0.13	0.86	0.07
WDM	100	1	0.09	0.07	0.12

5.3 Summary

Experiments were used to evaluate the cutting characteristics of CFRP using two disparate waterjet cutting processes, AWJ and WDM. The AWJ created cracks and delamination regions in the CFRP despite using the low-pressure pierce capabilities of the process. The WDM successfully cut the CFRP without delamination and with fairly acceptable geometric and dimensional accuracy, although at a much slower feed rate than the AWJ. In addition, the WDM process was able to cut very narrow kerfs, indicating that small CFRP part sizes can be fabricated with WDM. The features cut from WDM showed less taper although higher circularity and straightness error than those from AWJ. Therefore, WDM demonstrated some geometrical advantages but also some disadvantages compared to AWJ. Nevertheless, this unique cutting process can be a practical solution to cutting CFRP without the tendency of delamination, heat-generation, and dust emission. Although due to the slow feed rate required in WDM, one must consider total cutting time and cost, among other aspects, to justify its use over conventional cutting techniques such as end-mill and AWJ cutting. Future studies should investigate the CFRP cutting thickness limitation of WDM.

The favorable cutting performance of the WDM process can be seen as an achievement for pure waterjet cutting technology; however, the material removal mechanisms and the

ability for WDM to cut CFRP without delamination requires further investigation. It can be reasoned that the differences in jet morphology, e.g., continuous as in AWJ, versus discrete as in WDM, lead to disparate erosion processes, which result in the presence (or absence) of delamination. Finite element analyses and micro-mechanical modeling of the droplet-composite interaction are potential avenues through which the WDM erosion mechanisms can be identified.

6. CONCLUSIONS AND FUTURE WORK

Water droplet machining (WDM) is a manufacturing process whereby high-velocity water droplets are used to impact and erode a workpiece for through-cutting, pocket milling, and/or surface profiling. In this dissertation, the mechanics involved in droplet impact were investigated by first identifying the force imparted by droplets and droplet trains impacting normal to a surface. A novel force model was developed, applicable for a wide range of impact parameters, i.e., $280 < Re \leq 29,800$ and $37 < We \leq 6360$. This model is believed to be a significant contribution to the literature, due to ubiquitous occurrence of droplet impacts in nature and in industrial applications. This was extended to model the force of droplet train impacts, where relative to experimentation, good agreement was observed. The model and experiments also indicate that the peak force of a droplet train is approximately four times greater than the force exerted by a continuous jet of equal momentum. This finding suggests that droplet trains feature a higher erosive potential, owing to the higher forces involved.

The stress state of a material subject to quasi-static, axisymmetric Hertzian contact, which is similar to droplet loadings, was presented next, using integrated photoelasticity, where a relationship between applied force and equivalent stress was identified. Although this provides insight into the material's response, the erosion mechanisms of WDM are still unclear, and future work should investigate the deformation and fracture characteristics induced during WDM.

The WDM process parameters and their associated erosion characteristics were explored with a custom-build WDM device. The WDM technique is conducted within a sub-

atmospheric environment to inhibit aerodynamic drag and atomization of the waterjet/droplet train. This preserves droplet momentum and enables high-velocity droplets to strike and erode the workpiece. For small waterjet orifice diameters, e.g., $d = 100 \mu\text{m}$, it was found that a significant distance between the orifice and workpiece, e.g., $\text{SOD} > 0.5$ meter, is required for effective material removal. This is because natural droplet formation, from a continuous jet to a droplet train, requires ample amount of time (and therefore length). Workpieces placed too close to the orifice will experience a continuous/semi-continuous jet impact, which my research showed is less effective at material removal. The influence of orifice diameter was also investigated, where the erosion footprints suggest that (comparatively) large orifice diameters, $d > 180 \mu\text{m}$, result in atomized jets capable of eroding wide trenches in the workpiece, i.e., trench width $\gg d$. These orifice diameters would be particularly useful for milling or surface profiling, where large volumes of material are sought to be removed. However, they are not capable of creating precise and narrow through-cuts. An example of using WDM for pocket milling is shown in Figure 6.1(a). Here, WDM created a $48 \times 48 \text{ mm}^2$ pocket approximately 5 mm deep in a 12.5 mm thick 1018 steel plate. The WDM process parameters used during this procedure were $P = 414 \text{ MPa}$, $d = 410 \mu\text{m}$, $\text{SOD}_4 = 686 \text{ mm}$, and $f = 0.5 \text{ mm/s}$. The tool path, shown in Figure 6.1(b), starts in the center and spirals outward in a clockwise direction with a 4 mm step over length. The erosion footprint of this toolpath is recognizable in Figure 6.1(a), especially along the exterior edges, which are more pronounced due to transient conditions. Unlike typical WDM operating conditions in through-cutting mode, which are close to the triple point of water, the chamber pressure and temperature during this pocket milling process rose to 10 kPa and 45 °C, respectively.

This is because of the significant amount of heat added to the water when the largest flow rate (and orifice diameter) of the high-pressure pump are used. Future work should aim to mitigate transient effects in milling-mode and identify step-over lengths which produce uniform pockets. Additionally, the efficacy of WDM in surface profiling mode, i.e., to strip paint/rust, or texture a surface, should be investigated.

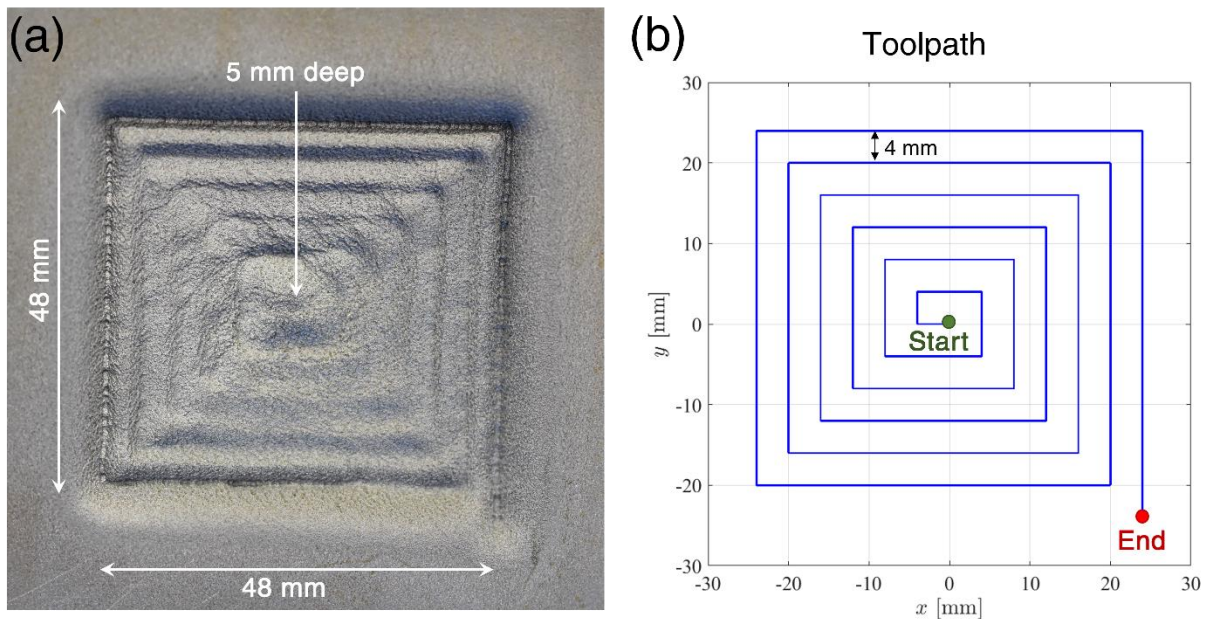


Figure 6.1: (a) Approximately $48 \times 48 \times 5 \text{ mm}^3$ pocket created in 1018 steel by WDM in milling-mode. (b) Toolpath used to create pocket with a step over length of 4 mm and feed rate of 0.5 mm/s.

A comparison between conventional PWJ cutting and WDM cutting was made for equivalent conditions, where WDM outperformed PWJ by creating a through-cut, while PWJ only created a trench in the workpiece. This result identifies WDM as an advancement in pure waterjet cutting technology. This novel through-cutting ability was tested further by cutting a variety of basic shapes in a 5.5 mm thick carbon fiber sheet. These tests were compared with conventional AWJ cutting of the same sheet, where AWJ resulted in cracks and delamination of the composite. WDM successfully cut the

carbon fiber without delamination and with fairly acceptable geometric and dimensional accuracy, although at a much slower feed rate than the AWJ.

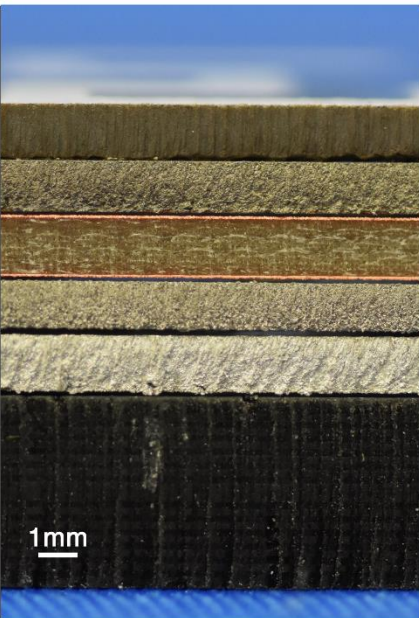






Material		Thickness (mm)	Feed rate (mm/s)	Orifice (μm)
Ceramic		1.4	0.8	100
Titanium (commercially pure)		1.3	0.5	125
Double sided FR4 circuit board		1.6	2.0	100
Stainless steel 316L		1.2	0.3	125
Aluminum 6022-T4		1.4	2.0	100
Carbon fiber reinforced polymer		5.5	1.0	100

Figure 6.2: Cut edge of materials cut by WDM (individually) at $P = 414 \text{ MPa}$, $\text{SOD}_4 = 686 \text{ mm}$. Relative to the workpiece, the WDM cuts from left to right.

Intrigued by WDM's unique cutting characteristics, the capability of WDM to cut a range of materials was explored. Figure 6.2 shows the cut edge of a variety of materials processed by WDM, which include aluminum, stainless steel, titanium, carbon fiber, FR4 circuit board, and ceramic. The figure also identifies the material, thickness and feed rate used to cut the materials with WDM cutting mode, i.e., $P = 414 \text{ MPa}$, $d = 100 \mu\text{m}$, $\text{SOD} = 686\text{mm}$. Owing to the excellent cuts produced by WDM, sample parts were produced to highlight the efficacy of this new manufacturing tool, see Figure 6.3. Future WDM research should aim to characterize erosions rates above a SOD of 686 mm, and further explore the range of materials.

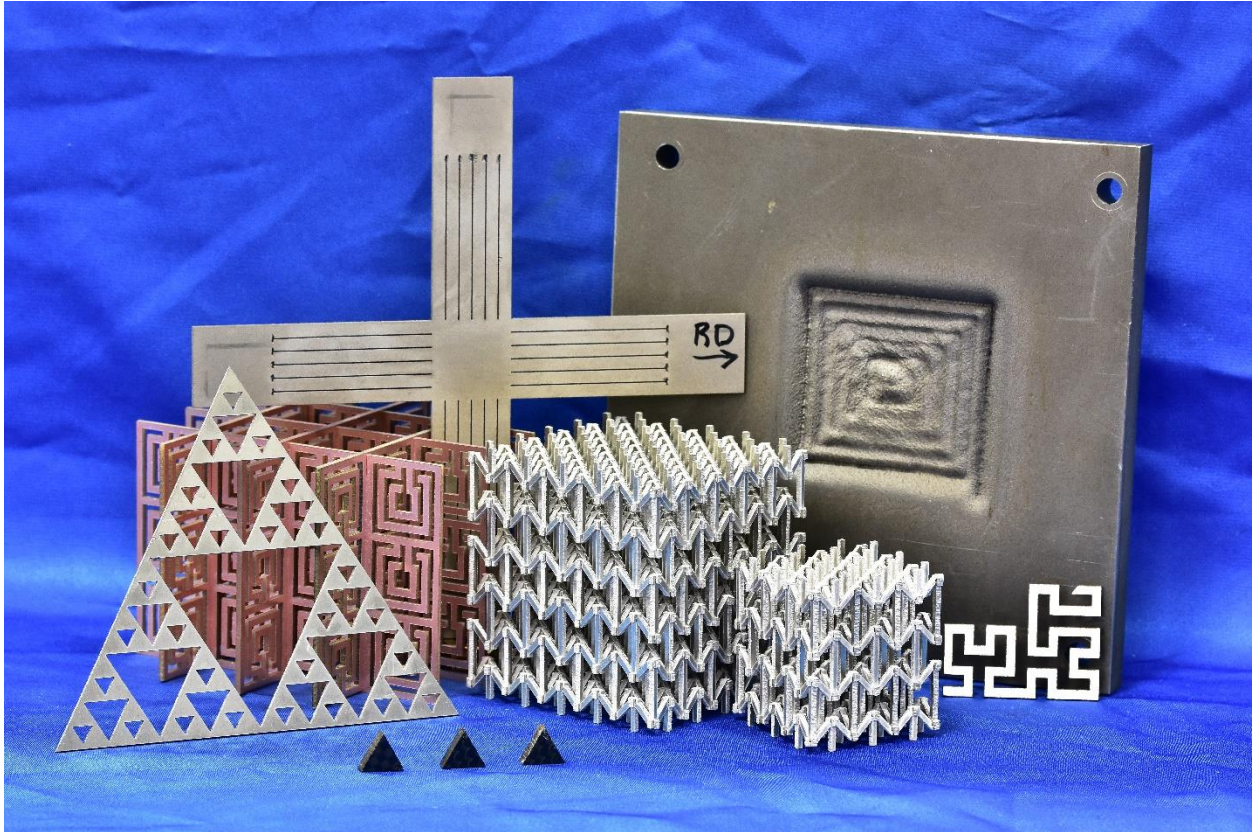


Figure 6.3: Variety of components made with WDM.

LIST OF REFERENCES

- [1] Axinte, D. A., Karpuschewski, B., Kong, M. C., Beaucamp, A. T., Anwar, S., Miller, D., & Petzel, M. (2014). High energy fluid jet machining (HEFJet-Mach): from scientific and technological advances to niche industrial applications. *CIRP Annals*, 63(2), 751-771.
- [2] Axinte, D. A., Srinivasu, D. S., Kong, M. C., & Butler-Smith, P. W. (2009). Abrasive waterjet cutting of polycrystalline diamond: A preliminary investigation. *International Journal of Machine Tools and Manufacture*, 49(10), 797-803.
- [3] Momber, A. W., & Kovacevic, R. (2012). *Principles of abrasive water jet machining*. Springer Science & Business Media.
- [4] Dean Jr, R., Nelson, D. F., Brown, M. L., Couch, R. W., & Blanchard, M. W. (2008). *U.S. Patent No. 7,380,918*. Washington, DC: U.S. Patent and Trademark Office.
- [5] Rayleigh, L. (1879). On the capillary phenomena of jets. *Proc. R. Soc. London*, 29(196-199), 71-97.

- [6] Kamkar, N., Bridier, F., Bocher, P., & Jedrzejowski, P. (2013). Water droplet erosion mechanisms in rolled Ti–6Al–4V. *Wear*, 301(1-2), 442-448.
- [7] Oka, Y. I., Mihara, S., & Miyata, H. (2007). Effective parameters for erosion caused by water droplet impingement and applications to surface treatment technology. *Wear*, 263(1-6), 386-394.
- [8] Mahdipoor, M. S., Kirols, H. S., Kevorkov, D., Jedrzejowski, P., & Medraj, M. (2015). Influence of impact speed on water droplet erosion of TiAl compared with Ti6Al4V. *Scientific reports*, 5, 14182.
- [9] Huang, L., Folkes, J., Kinnell, P., & Shipway, P. H. (2012). Mechanisms of damage initiation in a titanium alloy subjected to water droplet impact during ultra-high pressure plain waterjet erosion. *Journal of materials processing technology*, 212(9), 1906-1915.
- [10] Aldo Antonio Rueda, M., Fernando Rueda, M., Miguel Toledo, V., Florencio Sánchez, S., Ignacio Carvajal, M., & Juan Abugaber, F. (2012). The density and momentum distributions of 2-dimensional transonic flow in an LP-steam turbine. *Energy and Power Engineering*, 2012.
- [11] Elhadi Ibrahim, M., & Medraj, M. (2020). Water Droplet Erosion of Wind Turbine Blades: Mechanics, Testing, Modeling and Future Perspectives. *Materials*, 13(1), 157.
- [12] Fyall, A. A., King, R. B., & Strain, R. N. C. (1962). Rain erosion aspects of aircraft and guided missiles. *The Aeronautical Journal*, 66(619), 447-453.
- [13] Lesser, M. B. (1981). Analytic solution of liquid-drop impact problems. *Proceedings of the Royal Society of London. A. Mathematical and Physical Sciences*, 377(1770), 289-308.
- [14] Bowden, F. P., & Field, J. E. (1964). The brittle fracture of solids by liquid impact, by solid impact, and by shock. *Proceedings of the Royal Society of London. Series A. Mathematical and Physical Sciences*, 282(1390), 331-352.
- [15] Mitchell, B. R., Klewicki, J. C., Korkolis, Y. P., & Kinsey, B. L. (2019). The transient force profile of low-speed droplet impact: measurements and model. *Journal of Fluid Mechanics*, 867, 300-322.
- [16] Mitchell, B. R., Klewicki, J. C., Korkolis, Y. P., & Kinsey, B. L. (2019). Normal impact force of Rayleigh jets. *Physical Review Fluids*, 4(11), 113603.
- [17] Haferl, S., & Poulidakos, D. (2003). Experimental investigation of the transient impact fluid dynamics and solidification of a molten microdroplet pile-up. *International journal of heat and mass transfer*, 46(3), 535-550.

- [18] Šikalo, Š., Tropea, C., & Ganić, E. N. (2005). Dynamic wetting angle of a spreading droplet. *Experimental Thermal and Fluid Science*, 29(7), 795-802.
- [19] Philippi, J., Lagrée, P. Y., & Antkowiak, A. (2016). Drop impact on a solid surface: short-time self-similarity. *Journal of Fluid Mechanics*, 795, 96-135.
- [20] Wildeman, S., Visser, C. W., Sun, C., & Lohse, D. (2016). On the spreading of impacting drops. *Journal of fluid mechanics*, 805, 636-655.
- [21] Gordillo, L., Sun, T. P., & Cheng, X. (2018). Dynamics of drop impact on solid surfaces: evolution of impact force and self-similar spreading. *Journal of Fluid Mechanics*, 840, 190-214.
- [22] Thoraval, M. J., Takehara, K., Etoh, T. G., Popinet, S., Ray, P., Josserand, C., & Thoroddsen, S. T. (2012). von Kármán vortex street within an impacting drop. *Physical Review Letters*, 108(26), 264506.
- [23] Haller, K. K., Poulikakos, D., Ventikos, Y., & Monkewitz, P. (2003). Shock wave formation in droplet impact on a rigid surface: lateral liquid motion and multiple wave structure in the contact line region. *Journal of Fluid Mechanics*, 490, 1-14.
- [24] Haller, K. K., Ventikos, Y., Poulikakos, D., & Monkewitz, P. (2002). Computational study of high-speed liquid droplet impact. *Journal of Applied Physics*, 92(5), 2821-2828.
- [25] Yarin, A. L., & Weiss, D. A. (1995). Impact of drops on solid surfaces: self-similar capillary waves, and splashing as a new type of kinematic discontinuity. *Journal of Fluid Mechanics*, 283, 141-173.
- [26] Weiss, D. A., & Yarin, A. L. (1999). Single drop impact onto liquid films: neck distortion, jetting, tiny bubble entrainment, and crown formation. *Journal of Fluid Mechanics*, 385, 229-254.
- [27] Haley, P. J., & Miksis, M. J. (1991). The effect of the contact line on droplet spreading. *Journal of Fluid Mechanics*, 223, 57-81.
- [28] Pizzola, P. A., Roth, S., & De Forest, P. R. (1986). Blood droplet dynamics—I. *Journal of Forensic Science*, 31(1), 36-49.
- [29] Josserand, C., & Thoroddsen, S. T. (2016). Drop impact on a solid surface. *Annual review of fluid mechanics*, 48, 365-391.
- [30] Ahmad, M., Schatz, M., & Casey, M. V. (2013). Experimental investigation of droplet size influence on low pressure steam turbine blade erosion. *Wear*, 303(1-2), 83-86.
- [31] Amirzadeh, B., Louhghalam, A., Raessi, M., & Tootkaboni, M. (2017). A computational framework for the analysis of rain-induced erosion in wind turbine

blades, part I: Stochastic rain texture model and drop impact simulations. *Journal of Wind Engineering and Industrial Aerodynamics*, 163, 33-43.

- [32] Fyall, A. A. (1966). Practical aspects of rain erosion of aircraft and missiles. *Philosophical Transactions for the Royal Society of London. Series A, Mathematical and Physical Sciences*, 161-167.
- [33] Huang, L., Folkes, J., Kinnell, P., & Shipway, P. H. (2012). Mechanisms of damage initiation in a titanium alloy subjected to water droplet impact during ultra-high pressure plain waterjet erosion. *Journal of Materials Processing Technology*, 212(9), 1906-1915.
- [34] Römken, M. J., Helming, K., & Prasad, S. N. (2002). Soil erosion under different rainfall intensities, surface roughness, and soil water regimes. *Catena*, 46(2-3), 103-123.
- [35] Marshall, H. P., Conway, H., & Rasmussen, L. A. (1999). Snow densification during rain. *Cold Regions Science and Technology*, 30(1-3), 35-41.
- [36] Dickerson, A. K., Shankles, P. G., Madhavan, N. M., & Hu, D. L. (2012). Mosquitoes survive raindrop collisions by virtue of their low mass. *Proceedings of the National Academy of Sciences*, 109(25), 9822-9827.
- [37] Ortega-Jimenez, V. M., Badger, M., Wang, H., & Dudley, R. (2016). Into rude air: hummingbird flight performance in variable aerial environments. *Philosophical Transactions of the Royal Society B: Biological Sciences*, 371(1704), 20150387.
- [38] Baker, E. A., & Hunt, G. M. (1986). Erosion of waxes from leaf surfaces by simulated rain. *New Phytologist*, 102(1), 161-173.
- [39] Nearing, M. A., Bradford, J. M., & Holtz, R. D. (1986). Measurement of force vs. time relations for waterdrop impact. *Soil Science Society of America Journal*, 50(6), 1532-1536.
- [40] Grinspan, A. S., & Gnanamoorthy, R. (2010). Impact force of low velocity liquid droplets measured using piezoelectric PVDF film. *Colloids and Surfaces A: Physicochemical and Engineering Aspects*, 356(1-3), 162-168.
- [41] Li, J., Zhang, B., Guo, P., & Lv, Q. (2014). Impact force of a low speed water droplet colliding on a solid surface. *Journal of Applied Physics*, 116(21), 214903.
- [42] Zhang, B., Li, J., Guo, P., & Lv, Q. (2017). Experimental studies on the effect of Reynolds and Weber numbers on the impact forces of low-speed droplets colliding with a solid surface. *Experiments in Fluids*, 58(9), 1-12.
- [43] Yu, Y., & Hopkins, C. (2018). Experimental determination of forces applied by liquid water drops at high drop velocities impacting a glass plate with and without a

shallow water layer using wavelet deconvolution. *Experiments in Fluids*, 59(5), 1-23.

- [44] Mitchell, B. R., Nassiri, A., Locke, M. R., Klewicki, J. C., Korkolis, Y. P., & Kinsey, B. L. (2016, June). Experimental and numerical framework for study of low velocity water droplet impact dynamics. In *International Manufacturing Science and Engineering Conference* (Vol. 49897, p. V001T02A047). American Society of Mechanical Engineers.
- [45] Roisman, I. V. (2009). Inertia dominated drop collisions. II. An analytical solution of the Navier–Stokes equations for a spreading viscous film. *Physics of Fluids*, 21(5), 052104.
- [46] Josserand, C., & Zaleski, S. (2003). Droplet splashing on a thin liquid film. *Physics of fluids*, 15(6), 1650-1657.
- [47] Eggers, J., Fontelos, M. A., Josserand, C., & Zaleski, S. (2010). Drop dynamics after impact on a solid wall: theory and simulations. *Physics of fluids*, 22(6), 062101.
- [48] Roisman, I. V., Berberović, E., & Tropea, C. (2009). Inertia dominated drop collisions. I. On the universal flow in the lamella. *Physics of fluids*, 21(5), 052103.
- [49] Clift, R., Grace, J. R., & Weber, M. E. (2005). Bubbles, drops, and particles. *Dover Publications INC*, Mineola, New York.
- [50] Beard, K. V. (1976). Terminal velocity and shape of cloud and precipitation drops aloft. *Journal of Atmospheric Sciences*, 33(5), 851-864.
- [51] Szakall, M., Mitra, S. K., Diehl, K., & Borrmann, S. (2010). Shapes and oscillations of falling raindrops—A review. *Atmospheric research*, 97(4), 416-425.
- [52] Glycerine Producers' Association. (1963). *Physical properties of glycerine and its solutions*. Glycerine Producers' Association.
- [53] Trefethen, L. (1969). Surface tension in fluid mechanics. *Lubricating oil*, 25, 35-38.
- [54] Dorf, R. C. (2004). CRC Press LLC. *Hand Book of Engineering Table*, University of California, Davis, CRC.
- [55] Taylor, T. D., & Acrivos, A. (1964). On the deformation and drag of a falling viscous drop at low Reynolds number. *Journal of Fluid Mechanics*, 18(3), 466-476.
- [56] Thoroddsen, S. T., & Sakakibara, J. (1998). Evolution of the fingering pattern of an impacting drop. *Physics of Fluids*, 10(6), 1359-1374.
- [57] Saylor, J. R., & Jones, B. K. (2005). The existence of vortices in the wakes of simulated raindrops. *Physics of Fluids*, 17(3), 031706.

- [58] Xu, L., Zhang, W. W., & Nagel, S. R. (2005). Drop splashing on a dry smooth surface. *Physical Review Letters*, *94*(18), 184505.
- [59] Mitchell, B. R., Bate, T. E., Klewicki, J. C., Korkolis, Y. P., & Kinsey, B. L. (2017). Experimental investigation of droplet impact on metal surfaces in reduced ambient pressure. *Procedia Manufacturing*, *10*, 730-736.
- [60] Sikalo, S., Marengo, M., Tropea, C., & Ganic, E. N. (2000). Analysis of impact of droplets on horizontal surfaces. In *Thermal Sciences 2000. Proceedings of the International Thermal Science Seminar. Volume 1*. Begel House Inc.
- [61] Rioboo, R., Marengo, M., & Tropea, C. (2002). Time evolution of liquid drop impact onto solid, dry surfaces. *Experiments in fluids*, *33*(1), 112-124.
- [62] Lagubeau, G., Fontelos, M. A., Josserand, C., Maurel, A., Pagneux, V., & Petitjeans, P. (2012). Spreading dynamics of drop impacts. *Journal of Fluid Mechanics*, *713*, 50-60.
- [63] Coleman, H. W., & Steele, W. G. (2018). *Experimentation, validation, and uncertainty analysis for engineers*. John Wiley & Sons.
- [64] Tsai, P., Pacheco, S., Pirat, C., Lefferts, L., & Lohse, D. (2009). Drop impact upon micro-and nanostructured superhydrophobic surfaces. *Langmuir*, *25*(20), 12293-12298.
- [65] Mongruel, A., Daru, V., Feuillebois, F., & Tabakova, S. (2009). Early post-impact time dynamics of viscous drops onto a solid dry surface. *Physics of Fluids*, *21*(3), 032101.
- [66] Riboux, G., & Gordillo, J. M. (2014). Experiments of drops impacting a smooth solid surface: a model of the critical impact speed for drop splashing. *Physical review letters*, *113*(2), 024507.
- [67] Glover, H. W., Brass, T., Bhagat, R. K., Davidson, J. F., Pratt, L., & Wilson, D. I. (2016). Cleaning of complex soil layers on vertical walls by fixed and moving impinging liquid jets. *Journal of Food Engineering*, *178*, 95-109.
- [68] Webb, B. W., & Ma, C. F. (1995). Single-phase liquid jet impingement heat transfer. *Advances in Heat Transfer* (Vol. 26, pp. 105-217).
- [69] Fujimoto, H., Obana, W., Ashida, M., Hama, T., & Takuda, H. (2017). Hydrodynamics and heat transfer characteristics of oil-in-water emulsion droplets impinging on hot stainless steel foil. *Experimental Thermal and Fluid Science*, *85*, 201-212.
- [70] Singh, M., Haverinen, H. M., Dhagat, P., & Jabbour, G. E. (2010). Inkjet printing—process and its applications. *Advanced Materials*, *22*(6), 673-685.

- [71] Papachristou, D. N., & Barters, R. (1982). Resection of the liver with a water jet. *British Journal of Surgery*, 69(2), 93-94.
- [72] Ohki, T., Nakagawa, A., Hirano, T., Hashimoto, T., Menezes, V., Jokura, H., ... & Takayama, K. (2004). Experimental application of pulsed Ho: YAG laser-induced liquid jet as a novel rigid neuroendoscopic dissection device. *Lasers in Surgery and Medicine*, 34(3), 227-234.
- [73] Tagawa, Y., Oudalov, N., El Ghalbzouri, A., Sun, C., & Lohse, D. (2013). Needle-free injection into skin and soft matter with highly focused microjets. *Lab on a Chip*, 13(7), 1357-1363.
- [74] Reitz, R. D., & Bracco, F. V. (1982). Mechanism of atomization of a liquid jet. *The Physics of Fluids*, 25(10), 1730-1742.
- [75] Kim, H. Y., Feng, Z. C., & Chun, J. H. (2000). Instability of a liquid jet emerging from a droplet upon collision with a solid surface. *Physics of Fluids*, 12(3), 531-541.
- [76] Yarin, A. L. (2006). Drop impact dynamics: splashing, spreading, receding, bouncing.... *Annu. Rev. Fluid Mech.*, 38, 159-192.
- [77] Goedde, E. F., & Yuen, M. C. (1970). Experiments on liquid jet instability. *Journal of Fluid Mechanics*, 40(3), 495-511.
- [78] Eggers, J., & Villermaux, E. (2008). Physics of liquid jets. *Reports on Progress in Physics*, 71(3), 036601.
- [79] Rein, M. (1993). Phenomena of liquid drop impact on solid and liquid surfaces. *Fluid Dynamics Research*, 12(2), 61-93.
- [80] Vailati, A., Zinnato, L., & Cerbino, R. (2012). How archer fish achieve a powerful impact: hydrodynamic instability of a pulsed jet in *Toxotes jaculatrix*. *PLoS One*, 7(10), e47867.
- [81] Couillet, P., Mahadevan, L., & Riera, C. S. (2005). Hydrodynamical models for the chaotic dripping faucet. *Journal of Fluid Mechanics*, 526, 1-17.
- [82] Ranz, W. E. (1956). On sprays and spraying: a survey of spray technology for research and development engineers. 1956.—Department of Engineering Research, Pennsylvania State University.
- [83] Lin, S. P., & Reitz, R. D. (1998). Drop and spray formation from a liquid jet. *Annual Review of Fluid Mechanics*, 30(1), 85-105.
- [84] van Hoeve, W., Gekle, S., Snoeijer, J. H., Versluis, M., Brenner, M. P., & Lohse, D. (2010). Breakup of diminutive Rayleigh jets. *Physics of fluids*, 22(12), 122003.

- [85] Clanet, C., & Lasheras, J. C. (1999). Transition from dripping to jetting. *Journal of Fluid Mechanics*, 383, 307-326.
- [86] Lin, S. P. (2003). *Breakup of liquid sheets and jets*. Cambridge university press.
- [87] Leroux, S., Dumouchel, C., & Ledoux, M. (1996). The stability curve of Newtonian liquid jets. *Atomization and Sprays*, 6(6).
- [88] Leroux, S., Dumouchel, C., & Ledoux, M. (1997). The Break-up Length of Laminar Cylindrical Liquid Jets. Modification of Weber's Theory. *International Journal of Fluid Mechanics Research*, 24(1-3).
- [89] Kasyap, T. V., Sivakumar, D., & Raghunandan, B. N. (2009). Flow and breakup characteristics of elliptical liquid jets. *International Journal of Multiphase Flow*, 35(1), 8-19.
- [90] Umemura, A., Kawanabe, S., Suzuki, S., & Osaka, J. (2011). Two-valued breakup length of a water jet issuing from a finite-length nozzle under normal gravity. *Physical Review E*, 84(3), 036309.
- [91] García, F. J., González, H., Castrejón-Pita, J. R., & Castrejón-Pita, A. A. (2014). The breakup length of harmonically stimulated capillary jets. *Applied Physics Letters*, 105(9), 094104.
- [92] Sterling, A. M., & Sleicher, C. A. (1975). The instability of capillary jets. *Journal of Fluid Mechanics*, 68(3), 477-495.
- [93] Dumouchel, C. (2008). On the experimental investigation on primary atomization of liquid streams. *Experiments in Fluids*, 45(3), 371-422.
- [94] Fenn III, R. W., & Middleman, S. (1969). Newtonian jet stability: the role of air resistance. *AIChE Journal*, 15(3), 379-383.
- [95] Plateau, J. A. F. (1873). *Statique expérimentale et théorique des liquides soumis aux seules forces moléculaires* (Vol. 2). Gauthier-Villars.
- [96] Amini, G., & Dolatabadi, A. (2011). Capillary instability of elliptic liquid jets. *Physics of Fluids*, 23(8), 084109.
- [97] Amini, G., Lv, Y., Dolatabadi, A., & Ihme, M. (2014). Instability of elliptic liquid jets: Temporal linear stability theory and experimental analysis. *Physics of Fluids*, 26(11), 114105.
- [98] Eggers, J. (1997). Nonlinear dynamics and breakup of free-surface flows. *Reviews of Modern Physics*, 69(3), 865.
- [99] Leib, S. J., & Goldstein, M. E. (1986). Convective and absolute instability of a viscous liquid jet. *The Physics of Fluids*, 29(4), 952-954.

- [100]Keller, J. B., Rubinow, S. I., & Tu, Y. O. (1973). Spatial instability of a jet. *The Physics of Fluids*, 16(12), 2052-2055.
- [101]González, H., & García, F. J. (2009). The measurement of growth rates in capillary jets. *Journal of Fluid Mechanics*, 619, 179-212.
- [102]González, H., Vazquez, P. A., García, F. J., & Guerrero, J. (2018). Minimal formulation of the linear spatial analysis of capillary jets: Validity of the two-mode approach. *Physical Review Fluids*, 3(4), 044802.
- [103]Ardekani, A. M., Sharma, V., & McKinley, G. H. (2010). Dynamics of bead formation, filament thinning and breakup in weakly viscoelastic jets. *Journal of Fluid Mechanics*, 665, 46-56.
- [104]Shinjo, J., & Umemura, A. (2010). Simulation of liquid jet primary breakup: Dynamics of ligament and droplet formation. *International Journal of Multiphase Flow*, 36(7), 513-532.
- [105]Martin, G. D., Hoath, S. D., & Hutchings, I. M. (2008, March). Inkjet printing-the physics of manipulating liquid jets and drops. In *Journal of Physics: Conference Series* (Vol. 105, No. 1, p. 012001). IOP Publishing.
- [106]Chen, Y. J., & Steen, P. H. (1997). Dynamics of inviscid capillary breakup: collapse and pinchoff of a film bridge. *Journal of Fluid Mechanics*, 341, 245-267.
- [107]Wu, W. D., Lin, S. X., & Chen, X. D. (2011). Monodisperse droplet formation through a continuous jet break-up using glass nozzles operated with piezoelectric pulsation. *AIChE Journal*, 57(6), 1386-1392.
- [108]Rutland, D. F., & Jameson, G. J. (1971). A non-linear effect in the capillary instability of liquid jets. *Journal of Fluid Mechanics*, 46(2), 267-271.
- [109]Wu, P. K., Miranda, R. F., & Faeth, G. M. (1995). Effects of initial flow conditions on primary breakup of nonturbulent and turbulent round liquid jets. *Atomization and sprays*, 5(2).
- [110]Gavis, J., & Modan, M. (1967). Expansion and contraction of jets of Newtonian liquids in air: Effect of tube length. *The Physics of Fluids*, 10(3), 487-497.
- [111]Weber, C. (1931). Zum zerfall eines flüssigkeitsstrahles. *ZAMM-Journal of Applied Mathematics and Mechanics/Zeitschrift für Angewandte Mathematik und Mechanik*, 11(2), 136-154.
- [112]Yuen, M. C. (1968). Non-linear capillary instability of a liquid jet. *Journal of Fluid Mechanics*, 33(1), 151-163.

- [113]Frankel, I., & Weihs, D. (1985). Stability of a capillary jet with linearly increasing axial velocity (with application to shaped charges). *Journal of Fluid Mechanics*, 155, 289-307.
- [114]Richard, D., & Quéré, D. (2000). Bouncing water drops. *Europhysics Letters*, 50(6), 769.
- [115]Worthington, A. M. (1908). *A study of splashes*. Longmans, Green, and Company.
- [116]Anantharamaiah, N., Vahedi Tafreshi, H., & Pourdeyhimi, B. (2006). A study on hydroentangling waterjets and their impact forces. *Experiments in Fluids*, 41(1), 103-113.
- [117]Huber, Maksymilian Tytus. "Zur theorie der berührung fester elastischer körper." *Annalen der Physik* 319.6 (1904): 153-163.
- [118]Johnson, Kenneth L. "One hundred years of Hertz contact." *Proceedings of the Institution of Mechanical Engineers* 196.1 (1982): 363-378.
- [119]Lin, David C., et al. "Spherical indentation of soft matter beyond the Hertzian regime: numerical and experimental validation of hyperelastic models." *Biomechanics and Modeling in Mechanobiology* 8.5 (2009): 345-358.
- [120]Wang, Zhanjiang, et al. "Numerical methods for contact between two joined quarter spaces and a rigid sphere." *International Journal of Solids and Structures* 49.18 (2012): 2515-2527.
- [121]Vu-Quoc, Loc, Xiang Zhang, and Lee Lesburg. "Normal and tangential force–displacement relations for frictional elasto-plastic contact of spheres." *International Journal of Solids and Structures* 38.36-37 (2001): 6455-6489.
- [122]Johnson, Kenneth Langstreth. *Contact mechanics*. Cambridge University Press, 1987.
- [123]Ramesh, Krishnamurthi. *Developments in Photoelasticity*. IOP Publishing, 2021.
- [124]Aben, Hillar, and Claude Guillemet. *Photoelasticity of glass*. Springer Science & Business Media, 2012.
- [125]Ramesh, K., and Sachin Sasikumar. "Digital photoelasticity: Recent developments and diverse applications." *Optics and Lasers in Engineering* 135 (2020): 106186.
- [126]Marloff, R. H., et al. "Photoelastic determination of stress-intensity factors." *Experimental Mechanics* 11.12 (1971): 529-539.
- [127]Misseroni, Diego, et al. "Stress concentration near stiff inclusions: validation of rigid inclusion model and boundary layers by means of photoelasticity." *Engineering Fracture Mechanics* 121 (2014): 87-97.

- [128]Ramesh, K., M. P. Hariprasad, and S. Bhuvanewari. "Digital photoelastic analysis applied to implant dentistry." *Optics and Lasers in engineering* 87 (2016): 204-213.
- [129]Pandya, Yogesh, and Anand Parey. "Experimental investigation of spur gear tooth mesh stiffness in the presence of crack using photoelasticity technique." *Engineering Failure Analysis* 34 (2013): 488-500.
- [130]Doyle, James F., James W. Phillips, and Daniel Post. "Manual on Experimental Stress Analysis. Society for Experimental Mechanics." (1989).
- [131]Peatross, Justin, and Michael Ware. *Physics of light and optics*. Brigham: Brigham Young University, Department of Physics, 2011.
- [132]Mindlin, Raymond D., and Lawrence E. Goodman. "The Optical Equations of Three-Dimensional Photoelasticity." *Journal of Applied Physics* 20.1 (1949): 89-95.
- [133]O'Rourke, R. C. "Three-dimensional photoelasticity." *Journal of Applied Physics* 22.7 (1951): 872-878.
- [134]Aben, Hillar, and Claude Guillemet. "Integrated photoelasticity." *Photoelasticity of Glass*. Springer, Berlin, Heidelberg, 1993. 86-101.
- [135]Wijerathne, M. L. L., Kenji Oguni, and Muneo Hori. "Tensor field tomography based on 3D photoelasticity." *Mechanics of Materials* 34.9 (2002): 533-545.
- [136]Aben, H. K., J. I. Josepson, and K-JE Kell. "The case of weak birefringence in integrated photoelasticity." *Optics and Lasers in Engineering* 11.3 (1989): 145-157.
- [137]Ainola, Leo, and Hillar Aben. "On the generalized Wertheim law in integrated photoelasticity." *JOSA A* 25.8 (2008): 1843-1849.
- [138]Ainola, Leo, and Hillar Aben. "Principal formulas of integrated photoelasticity in terms of characteristic parameters." *JOSA A* 22.6 (2005): 1181-1186.
- [139]Kavanagh, J. L., Thierry Menand, and Katherine A. Daniels. "Gelatin as a crustal analogue: Determining elastic properties for modelling magmatic intrusions." *Tectonophysics* 582 (2013): 101-111.
- [140]Sun, Ting-Pi, et al. "Erosion by dripping drops: The stress distribution and surface shock wave of drop impact." arXiv preprint arXiv:2108.09398 (2021).
- [141]Popov, Valentin L. *Contact mechanics and friction*. Berlin: Springer Berlin Heidelberg, 2010.
- [142]Pansino, Stephen, and Benoit Taisne. "Shear Wave Measurements of a Gelatin's Young's Modulus." *Frontiers in Earth Science* 8 (2020): 171.

- [143]van Otterloo, Jozua, and Alexander R. Cruden. "Rheology of pig skin gelatine: Defining the elastic domain and its thermal and mechanical properties for geological analogue experiment applications." *Tectonophysics* 683 (2016): 86-97.
- [144]Kwon, Jiwoon, and Ghatu Subhash. "Compressive strain rate sensitivity of ballistic gelatin." *Journal of Biomechanics* 43.3 (2010): 420-425.
- [145]Winter, J., and D. Shifler. *The material properties of gelatin gels. MARVALAUD INC WESTMINSTER MD, 1975.*
- [146]Harris, Jack K. "A photoelastic substrate technique for dynamic measurements of forces exerted by moving organisms." *Journal of Microscopy* 114.2 (1978): 219-228.
- [147]Wijerathne, M. L. L., Kenji Oguni, and Muneo Hori. "Stress field tomography based on 3D photoelasticity." *Journal of the Mechanics and Physics of Solids* 56.3 (2008): 1065-1085.
- [148]Ainola, Leo, and Hillar Aben. "Factorization of the polarization transformation matrix in integrated photoelasticity." *JOSA A* 24.11 (2007): 3397-3402.
- [149]Ainola, Leo, and Hillar Aben. "Principal formulas of integrated photoelasticity in terms of characteristic parameters." *JOSA A* 22.6 (2005): 1181-1186.
- [150]Aben, Hillar, Andrei Errapart, and Leo Ainola. "On real and imaginary algorithms of optical tensor field tomography." *Proceedings-Estonian Academy of Sciences Physics Mathematics*. Vol. 55. No. 2. Estonian Academy Publishers; 1999, 2006.
- [151]Aben, Hillar K., et al. "Photoelastic tomography for residual stress measurement in glass." *Optical Engineering* 44.9 (2005): 093601.
- [152]Srinath, L. S., and A. V. S. S. R. Sarma. "Determination of the optically equivalent model in three-dimensional photoelasticity." *Experimental Mechanics* 14.3 (1974): 118-122.
- [153]Peatross, Justin, and Michael Ware. "Physics of light and optics: a free online textbook." *Laser Science*. Optical Society of America, 2010.
- [154]Onuma, Takashi, and Yukitoshi Otani. "A development of two-dimensional birefringence distribution measurement system with a sampling rate of 1.3 MHz." *Optics Communications* 315 (2014): 69-73.
- [155]Riera, J. D., and R. Mark. "The optical-rotation effect in photoelastic shell analysis." *Experimental Mechanics* 9.1 (1969): 9-16.
- [156]Love, Augustus Edward Hough. "IX. The stress produced in a semi-infinite solid by pressure on part of the boundary." *Philosophical Transactions of the Royal Society*

of London. Series A, Containing Papers of a Mathematical or Physical Character 228.659-669 (1929): 377-420.

- [157]Ike, Charles Chinwuba. "Love stress function method for solving axisymmetric elasticity problems of the elastic halfspace." *Electronic Journal of Geotechnical Engineering* 24.3 (2019): 663-706.
- [158]Mitchell, B. R., Demian, S. A., Korkolis, Y. P., & Kinsey, B. L. (2020). Experimental comparison of material removal rates in abrasive waterjet cutting and a novel droplet stream technique. *Procedia Manufacturing*, 48, 586-592.
- [159]Axinte, D. A., Karpuschewski, B., Kong, M. C., Beaucamp, A. T., Anwar, S., Miller, D., & Petzel, M. (2014). High energy fluid jet machining (HEFJet-Mach): from scientific and technological advances to niche industrial applications. *CIRP Annals*, 63(2), 751-771.
- [160]Mieszala, M., Torrubia, P. L., Axinte, D. A., Schwiedrzik, J. J., Guo, Y., Mischler, S., ... & Philippe, L. (2017). Erosion mechanisms during abrasive waterjet machining: model microstructures and single particle experiments. *Journal of Materials Processing Technology*, 247, 92-102.
- [161]Hashish, M. (1984). A modeling study of metal cutting with abrasive waterjets. *J. Eng. Mater. Tech.*, 106(1), 88-100.
- [162]Kovacevic, R., Hashish, M., Mohan, R., Ramulu, M., Kim, T. J., & Geskin, E. S. (1997). State of the art of research and development in abrasive waterjet machining. *Journal of Manufacturing Science and Engineering* 119(4B), 776-785.
- [163]Nebeker, E. B. (1987, August). Percussive jets-State-of-the-art. In *Proceedings of the Fourth US Water Jet Conference* (pp. 32-45).
- [164]Foldyna, J., Sitek, L., Šuka, J., Martinec, P., Valíek, J., & Páleníková, K. (2009). Effects of pulsating water jet impact on aluminium surface. *Journal of Materials Processing Technology*, 209(20), 6174-6180.
- [165]Foldyna, J., Sitek, L., Švehla, B., & Švehla, Š. (2004). Utilization of ultrasound to enhance high-speed water jet effects. *Ultrasonics Sonochemistry*, 11(3-4), 131-137.
- [166]Bowden, F. P., & Field, J. E. (1964). The brittle fracture of solids by liquid impact, by solid impact, and by shock. *Proceedings of the Royal Society of London. Series A. Mathematical and Physical Sciences*, 282(1390), 331-352.
- [167]Heymann, F. J. (1969). High-speed impact between a liquid drop and a solid surface. *Journal of Applied Physics*, 40(13), 5113-5122.
- [168]Otendal, M., Hemberg, O., Tuohimaa, T. T., & Hertz, H. M. (2005). Microscopic high-speed liquid-metal jets in vacuum. *Experiments in Fluids*, 39(5), 799-804.

- [169] Shimizu, M., Arai, M., & Hiroyasu, H. (1984). Measurements of breakup length in high speed jet. *Bulletin of JSME*, 27(230), 1709-1715.
- [170] Kong, M. C., Axinte, D., & Voice, W. (2010). Aspects of material removal mechanism in plain waterjet milling on gamma titanium aluminide. *Journal of Materials Processing Technology*, 210(3), 573-584.
- [171] Hu, W., Shin, Y. C., & King, G. (2010). Modeling of multi-burst mode pico-second laser ablation for improved material removal rate. *Applied Physics A*, 98(2), 407-415.
- [172] Jerman, M., Orbanic, H., Etxeberria, I., Suarez, A., Junkar, M., & Lebar, A. (2011, September). Measuring the water temperature changes throughout the abrasive water jet cutting system. In *2011 WJTA American waterjet conference* (pp. 12-20).
- [173] Chung, D. (2012). *Carbon fiber composites*. Elsevier.
- [174] Che, D., Saxena, I., Han, P., Guo, P., & Ehmann, K. F. (2014). Machining of carbon fiber reinforced plastics/polymers: a literature review. *Journal of Manufacturing Science and Engineering*, 136(3).
- [175] Karataş, M. A., & Gökkaya, H. (2018). A review on machinability of carbon fiber reinforced polymer (CFRP) and glass fiber reinforced polymer (GFRP) composite materials. *Defence Technology*, 14(4), 318-326.
- [176] El-Sonbaty, I., Khashaba, U. A., & Machaly, T. (2004). Factors affecting the machinability of GFR/epoxy composites. *Composite Structures*, 63(3-4), 329-338.
- [177] Durão, L. M. P., Gonçalves, D. J., Tavares, J. M. R., de Albuquerque, V. H. C., Vieira, A. A., & Marques, A. T. (2010). Drilling tool geometry evaluation for reinforced composite laminates. *Composite Structures*, 92(7), 1545-1550.
- [178] Davim, J. P., & Reis, P. (2003). Study of delamination in drilling carbon fiber reinforced plastics (CFRP) using design experiments. *Composite structures*, 59(4), 481-487.
- [179] Gaitonde, V., Karnik, S. R., Rubio, J. C., Correia, A. E., Abrao, A. M., & Davim, J. P. (2008). Analysis of parametric influence on delamination in high-speed drilling of carbon fiber reinforced plastic composites. *Journal of Materials Processing Technology*, 203(1-3), 431-438.
- [180] Shahrajabian, H., Hadi, M., & Farahnakian, M. (2012). Experimental investigation of machining parameters on machinability of carbon fiber/epoxy composites. *International Journal of Engineering and Innovative Technology*, 3(3), 30-36.

- [181]Du, J., Zhang, H., Geng, Y., Ming, W., He, W., Ma, J., & Liu, K. (2019). A review on machining of carbon fiber reinforced ceramic matrix composites. *Ceramics International*, 45(15), 18155-18166.
- [182]Krishnaraj, V., Prabukarthy, A., Ramanathan, A., Elanghovan, N., Kumar, M. S., Zitoune, R., & Davim, J. P. (2012). Optimization of machining parameters at high speed drilling of carbon fiber reinforced plastic (CFRP) laminates. *Composites Part B: Engineering*, 43(4), 1791-1799.
- [183]Slamani, M., Chatelain, J. F., & Hamedanianpour, H. (2019). Influence of machining parameters on surface quality during high speed edge trimming of carbon fiber reinforced polymers. *International Journal of Material Forming*, 12(3), 331-353.
- [184]Rawat, S., & Attia, H. (2009). Wear mechanisms and tool life management of WC-Co drills during dry high speed drilling of woven carbon fibre composites. *Wear*, 267(5-8), 1022-1030.
- [185]Senthilkumar, M., Prabukarthy, A., & Krishnaraj, V. (2018). Machining of CFRP/Ti6Al4V stacks under minimal quantity lubricating condition. *Journal of Mechanical Science and Technology*, 32(8), 3787-3796.
- [186]Pagano, N., Ascari, A., Liverani, E., Donati, L., Campana, G., & Fortunato, A. (2015). Laser interaction with carbon fibre reinforced polymers. *Procedia Cirp*, 33, 423-427.
- [187]Takahashi, K., Tsukamoto, M., Masuno, S., Sato, Y., Yoshida, H., Tsubakimoto, K., & Ogata, H. (2015). Influence of laser scanning conditions on CFRP processing with a pulsed fiber laser. *Journal of Materials Processing Technology*, 222, 110-121.
- [188]Patel, P., Sheth, S., & Patel, T. (2016). Experimental analysis and ANN modelling of HAZ in laser cutting of glass fibre reinforced plastic composites. *Procedia Technology*, 23, 406-413.
- [189]John, K. M., & Kumaran, S. T. (2020). Backup support technique towards damage-free drilling of composite materials: A review. *International Journal of Lightweight Materials and Manufacture*, 3(4), 357-364.
- [190]Shanmugam, D. K., Nguyen, T., & Wang, J. (2008). A study of delamination on graphite/epoxy composites in abrasive waterjet machining. *Composites Part A: Applied Science and Manufacturing*, 39(6), 923-929.
- [191]Schwartzentruber, J., Papini, M., & Spelt, J. K. (2018). Characterizing and modelling delamination of carbon-fiber epoxy laminates during abrasive waterjet cutting. *Composites Part A: Applied Science and Manufacturing*, 112, 299-314.

- [192]Kim, G., Denos, B. R., & Sterkenburg, R. (2020). Influence of different piercing methods of abrasive waterjet on delamination of fiber reinforced composite laminate. *Composite Structures*, 240, 112065.
- [193]Schwartzentruber, J., Spelt, J. K., & Papini, M. (2018). Modelling of delamination due to hydraulic shock when piercing anisotropic carbon-fiber laminates using an abrasive waterjet. *International Journal of Machine Tools and Manufacture*, 132, 81-95.
- [194]Nyaboro, J. N., Ahmed, M. A., El-Hofy, H., & El-Hofy, M. (2020). Fluid-structure interaction modeling of the abrasive waterjet drilling of carbon fiber reinforced polymers. *Journal of Manufacturing Processes*, 58, 551-562.
- [195]Thongkaew, K., Wang, J., & Li, W. (2019). An investigation of the hole machining processes on woven carbon-fiber reinforced polymers (CFRPs) using abrasive waterjets. *Machining Science and Technology*, 23(1), 19-38.
- [196]Guglielmi, G., Mitchell, B., Song, C., Kinsey, B. L., & Mo, W. (2021). Life Cycle Environmental and Economic Comparison of Water Droplet Machining and Traditional Abrasive Waterjet Cutting. *Sustainability*, 13(21), 12275.
- [197]<https://waterjet-calculator.hypertherm.com/>
- [198]Orbanic, H., & Junkar, M. (2008). Analysis of striation formation mechanism in abrasive water jet cutting. *Wear*, 265(5-6), 821-830.
- [199]El-Hofy, M., Helmy, M. O., Escobar-Palafox, G., Kerrigan, K., Scaife, R., & El-Hofy, H. (2018). Abrasive water jet machining of multidirectional CFRP laminates. *Procedia Cirp*, 68, 535-540.